Title	Non-perturbative analysis on thermal radiations of photons and dileptons from quark-gluon plasma
Author(s)	金, 泰広
Citation	大阪大学, 2017, 博士論文
Version Type	VoR
URL	https://doi.org/10.18910/61518
rights	
Note	

Doctoral Dissertation

Non-perturbative analysis on thermal radiations of photons and dileptons from quark-gluon plasma

Taekwang Kim
Graduate School of Osaka University

February 2, 2017

Abstract

It is expected that a colored matter fulfills the early universe although the colored state cannot be observed on the present earth. Owing to a development of an accelerator and huge efforts, physicists succeeded to produce the colored matter on the earth by ultra-relativistic heavy ion collisions. By investigations on several observables, it is found that the produced colored matter seems to be strongly coupled. The colored matter is called quark-gluon plasma. However, among several observables, photon and dilepton production rates from the colored medium are still evaluated by a perturbative method. It is desirable to estimate these rates beyond a perturbation theory and this thesis is devoted to a non-perturbative analysis of photons and dileptons.

Thermal radiations of photons and dileptons from the deconfined medium make important roles in ultra-relativistic heavy ion collisions. Photons and dileptons emitted from the quark-gluon plasma are direct signals of the deconfined matter and include the information on the medium.

In this study, I evaluate production rates of thermal photons and dileptons from quark-gluon plasma with a non-perturbative method. Electromagnetic radiations are proportional to the imaginary part of a photon self energy. I analyze the photon self energy with a quark propagator obtained by a lattice QCD numerical simulation and a gauge invariant vertex. Numerical simulation on the lattice QCD is a first-principle calculation, and thus the photon self energy constructed with the lattice quark propagator is expected to include non-perturbative effects. Moreover, the obtained self energy respects the gauge invariance which makes a significantly important role in the quantum field theory.

In this study, the lattice quark propagator is composed of two quasi-particle states. Quasi-particles are particle-like thermal excited states of quarks. On the lattice, one of the quasi-particles called plasmino has a peculiar nature that its dispersion has the minimum at finite momentum and it exists even in the space-like region. Owing to these characteristics, production rates evaluated with the lattice quark propagator also obtain peculiar structures.

I obtained suggestive results of production rates. A photon spectrum shows non-smooth variations and the almost same slope as perturbative one. The former structure is understood by kinematics of quasi-particles and I verify that the slope is determined by a thermal factor. A dilepton spectrum shows a characteristic structure called van Hove singularity. This structure is also understood by kinematics of quasi-particles. Surprisingly, obtained spectra of photons and dileptons show comparable or slightly smaller rates to perturbative results although production processes are completely different. Finally, I discuss effects of obtained results on analyses of each electromagnetic observable measured in heavy ion collisions.

Contents

1 Introduction

1.1 Electromagnetic Probes as Direct Signals of Quark-Gluon Plasma

At zero temperature and almost zero baryon chemical potential where the environment we are alive, colored particles like quarks and gluons are confined in hadrons. Single quark or gluon are not observed by themselves and only the colorless state is observed. However, as the temperature of the medium is increased, the vacuum transforms qualitatively [1, 2]. Statistical mechanics suggests that meson states which are $q\bar{q}$ pairs start increase and gradually fulfill the space. Due to the large number of mesonic states, the average distance between two mesons become smaller than sizes of mesons. Under such a condition, quarks, anti-quarks and gluons which are confined in a single meson in vacuum are no longer confined. Each meson state melts to a hot medium where colored particles can propagate without the color confinement. It means that the hot medium is colored state, and thus called the deconfined medium or the quark-gluon plasma (QGP).

Owing to a great deal of effort, physicists succeeded to produce QGP [3, 4]. In ultra-relativistic heavy ion collisions (HIC), two heavy nuclei such as gold or lead are accelerated with ring type accelerators and collided each other. Ultra-relativistic HIC are the unique method to produce the deconfined medium experimentally on the Earth [3,4]. However, the produced QGP has extremely short life time of order 10fm/c and it soon cools down to a hadronic medium. Therefore, a direct observation of QGP is impossible and multilateral analyses are demanded to investigate QGP. Detected particles in HIC are hadrons, leptons and photons. The hadronic and electromagnetic signals have qualitatively different characters. Hadrons are strongly interacting particles, and thus they are frequently scattered by the hot medium composed of hadrons whose size is the order of 10fm. In contrast, leptons and photons do not interact with the medium by the strong interaction owing to their colorless natures. Although the constituents of hot media include particles with electromagnetic charges, a mean free path of colorless particles is roughly estimated as of order 100fm which is significantly larger than the typical size of the hot medium. Therefore, once leptons and photons are produced, they penetrate the hot medium without scatterings. This is a characteristic feature of electromagnetic signals observed in HIC. Leptons and photons emitted from QGP are direct signals of QGP themselves. Therefore, electromagnetic signals are also considered as important probes to study hot media and have been studied actively over a few decades [5, 6]. Electromagnetic signals are produced via several mechanisms during the time evolution of HIC. In this study, we focus on thermal real photons and virtual photons radiated from the hot deconfined medium. The real photon is on-shell photon itself and the virtual photon is off-shell state photon. The produced virtual photons are converted to a lepton and an anti-lepton pair in final state and the invariant mass of the lepton pair is same as the one of the virtual photon. The lepton pair is called “dilepton”.

1.2 Thermal Photons and Dileptons from Hot Medium

During the time evolution of ultra-relativistic HIC, photons and dileptons are produced via several reactions in each stage. Several experimental data of photon and dilepton production yield in HIC [7–10] imply the importance of the contribution of hot media. Photon and dilepton production yields are the total amounts of photons and dileptons observed in HIC. Each production yield is compared to two protons collision (*pp* collision) data with a modification of the number of collisions among nucleons in nuclei. *pp* collisions are considered that they do not produce hot media, or even if hot media are produced, the effect on electromagnetic probes is expected to be small. When one compares HIC results with reference data obtained by *pp* collisions, one finds that dilepton production yields excess reference data in lower invariant mass regions ($\lesssim$ 1GeV) and photon production yields excess references in lower transverse momentum regions ($\lesssim$ 2GeV). These facts support the existence of a hot medium and the contribution from the medium is not negligible. To evaluate contributions from hot media theoretically is a challenging work for research of heavy ion collision physics and QGP. Other important observables are photon anisotropic flows. Anisotropic flows are anisotropies of particle productions and the dynamics of HIC is reflected on several flows. Surprisingly, observed photon flows are large as same as the ones of pions which are main components of the hot hadronic medium. This result is controversial because photon flows seems to be smaller than the ones of pions due to its colorless nature. Details of experiments are reviewed in Section 2.4.

The importance of the deconfined medium on photons and dileptons is confirmed. Moreover, analyses with hydrodynamics reveal that the deconfined medium produced in HIC is strongly coupled [12, 13]. Therefore, a perturbative analysis on QGP is not justified because the perturbation theory is reliable only when a strength of interaction is weak. However, previous theoretical analyses are based on the perturbation theory. A non-perturbative analysis is desirable to evaluate contributions of the deconfined medium. One comes up first with a lattice numerical simulation. Indeed, several works on dilepton radiation are reported for the case of zero three dimensional momentum [14, 15]. However, due to the ill-posed problem and a numerical cost, it is still difficult to estimate each production rate on the lattice for finite momentum.

In this thesis, I evaluate photon and dilepton production rates from QGP by a non-perturbative method. Two thermal radiation rates are related to the photon self energy in the medium [16–18]. To evaluate production rates non-perturbatively, we face to a problem to analyze a full photon self energy. The analysis of the full photon self energy is extremely difficult. From the Schwinger-Dyson equation, the full photon self energy is constructed with a full quark propagator and a full photon-quark vertex. To deal with the difficulty, we analyze the photon self energy with a finite temperature quark propagator obtained by a lattice numerical simulation [19–21]. I substitute the lattice quark propagator for the Schwinger-Dyson equation. This calculation is a non-perturbative analysis because the lattice numerical simulation is an ab initio calculation. A photon-quark vertex is constructed with the lattice quark propagator gauge invariantly which makes a significant role in the quantum field theory. In this paper, we analyze the photon self energy non-perturbatively with this method. Obtained production rates have curious structures which reflect peculiar structures of the thermal excited states of quarks. Obtained spectra of photon and dilepton production rates can be interpreted as overlaps of contributions arisen from several production reactions among quasi-particles. Quasi-particles are particle-like thermal excited states of quarks. On the lattice, one of the quasi-particles has an odd behavior that it exists even in space-like region. This structure permits photon and dilepton productions via two quasi-particle pair annihilation which are forbidden in the perturbative analysis. In this analysis, furthermore, real photons are produced via the Landau damping which cannot be occurred in the perturbative analysis.

1.3 Contents of Thesis

In order to calculate each production "yield" theoretically, one needs a production "rate" of the hot medium which is the radiation rate per unit time per unit volume from the static medium and a dynamical model which pictures the time evolution of the medium. In the present work, only non-perturbative analyses of production rates are discussed although the future goal is to evaluate a contribution from QGP non-perturbatively. Even thermal production rates of the deconfined medium themselves include curious phenomena.

The outline of this paper is as follows. In the next section, we overview the quantum chromodynamics and give a review of photons and dileptons observed in HIC. An important characteristics of QCD is color confinement. Owing to this nature, quarks and gluons are confined in hadrons at low temperature and low chemical potential. We discuss a mechanism how deconfinement of colored particles happen when one increases the temperature of the system. Photons and dileptons are important observables in HIC. We also make a brief review of observables called "yield" and "flow". These observables support the importance of hot media in HIC.

In Section 3, we deal with basics of the finite temperature quantum field theory and introduce the relationship between electromagnetic thermal production rates and the photon self energy. We explain an imaginary time correlator which plays a significantly important role in the finite temperature quantum field theory. We also discuss a method to extract a real time correlator which is related to each observable from the imaginary time correlator via an analytic continuation. Furthermore, We treat a famous perturbation theory called a hard thermal loop (HTL) resummed perturbation theory in the same section and derive perturbative results of each radiation. A spectral function of the HTL quark propagator is composed of two quasi-particles states and a continuum part. This review of perturbation analyses will help us to discuss our results obtained by a non-perturbative way.

In Section 4, we discuss the lattice quark propagator [19–21] and a gauge invariant vertex. The lattice quark propagator is extracted from the imaginary time correlator via two pole ansatz, and thus it has only particle-like thermal excited states. We discuss structures of dispersion relations of two quasi-particles. The vertex is constructed from the Ward-Takahashi identity so as to satisfy the gauge invariance which plays an essential role in the quantum field theory. Then we construct a formalism of the photon self energy with them. We discuss relations between each production channel and kinematics among photon and quasi-particles.

Numerical results are presented in Section 5. Photon and dilepton production rates are evaluated two temperatures for $T = 1.5T_\mathrm{c}$ and $3T_\mathrm{c}$ with a pseudo critical temperature T_c. Photon production rate shows non-smooth variations and a similar slope as the perturbative one. Surprisingly, obtained spectral show the almost same strength as the perturbative one. Dilepton production rate shows an enhancement owing to the van Hove singularity. We explain these structures.

We consider physical interpretation of obtained results in Section 6. We discuss an effect of our results on each observable phenomenologically. The final section is devoted to a brief summary.

2 Review of Photons and Dileptons in Heavy Ion collisions

In this section, first, we overview elemental features of the quantum chromodynamics which is the theory to describe the dynamics of colored particles. It will help us to skim the dynamics among quarks and gluons. Then, we inspect observables concerning to photons and dileptons produced in HIC. The dynamics of HIC is reflected on electromagnetic observables, and thus photons and dileptons can be keys to know characteristics of hot media.

2.1 Quantum Chromodynamics

We make a brief review of the quantum chromodynamics (QCD). QCD corresponds to a Yang-Mills theory [22] in the case of SU(3) symmetry and describes a dynamics among quarks and gluons. Quark and gluon interact by the strong interaction. The former is a fermion and proposed to understand hadron multiplet simply [23, 24]. The quark was confirmed its presence via an electron-proton deep inelastic scattering experiment at Stanford Linear Accelerator Center [25]. At present, six quarks are discovered called up, down, strange, charm, top and bottom (or beauty). Taking initials, quarks are referred to as u, d, s, c, t and b, respectively. These six types of quarks are called flavors. The latter corresponds to a gauge boson proposed in Ref. [26] and was discovered experimentally via three jet events [27].

A plenty study on the ratio of hadronic to leptonic cross sections $\sigma(e^+e^- \to \text{hadrons})$ leads the discovery of the charm quark and the confirmation of the "color" SU(3) symmetry [28, 29]. Quarks and gluons have color charges of SU(3) symmetry and the strong interaction interacts between color charges. Quarks have three colors called red, blue and green, and thus they are belong to the fundamental representation of SU(3). On the other hand, gluons play a role to mediate color exchanges between quarks and themselves, and thus there are eight gluons exist. Gluons are belong to the adjoint representation of SU(3).

At the beginning, we refereed QCD as the theory which describe the dynamics of the strong interaction. One finds that the strong interaction affects between color charges, and thus QCD is the theory to describe the dynamics of colored fields. Now let us skim the QCD Lagrangian which produces equations of motions of quark and gluon fields. The QCD Lagrangian $\mathscr{L}_{\text{QCD}}$ is given by

$$\mathscr{L}_{\text{QCD}} = \bar{\psi}(i\not{D} - m)\psi - \frac{1}{4}\sum_a F^a_{\mu\nu}F^{\mu\nu,a}, \tag{1}$$

where ψ is the quark field, $\bar{\psi} = \psi^\dagger\gamma_0$, m is a quark mass, D_μ is a covariant derivative and $F^a_{\mu\nu}$ is a field strength tensor, respectively. The covariant derivative is defined as $D_\mu = \partial_\mu - ig\sum_a A^a_\mu t^a$ with a coupling constant of the strong interaction g, a SU(3) gauge field A^a_μ and a generator of SU(3) t^a, where the color index a takes one to eight. In Eq. (1), we suppressed the Dirac index and the color index of quark fields for simplicity. We define $\not{D} = D_\mu\gamma^\mu$ with a γ-matrix which satisfies an anticommutation relation $\{\gamma_\mu, \gamma_\mu\} = 2g_{\mu\nu}$. We define the metric $g_{\mu\nu} = (+,-,-,-)$. The field strength tensor $F^a_{\mu\nu}$ is given by

$$F^a_{\mu\nu} = \partial_\mu A^a_\nu - \partial_\nu A^a_\mu + g \sum_{b,c} f^{abc} A^b_\mu A^c_\nu, \tag{2}$$

where the f^{abc} is a structure constant of SU(3) group. Eq. (1) treats a single flavor QCD. When one considers several quarks, extra kinetic terms of quarks $\bar{\psi}(i \not{D} - m)\psi$ are added to Eq. (1) with appropriate mass terms.

Owing to the non-abelian nature of the symmetry, the QCD field strength tensor Eq. (2) gets the non-linear term proportional to f^{abc} which is never seen in the case of quantum chromodynamics. The non-linear term leads the QCD Lagrangian with interaction terms of three and four gauge bosons. In the aspect of the Feynman rule, these interaction terms are converted to a three gauge boson vertex and a four gauge boson vertex. Three point and four point interactions among gluons introduce rich and complex QCD dynamics.

2.1.1 Asymptotic Freedom and Confinement

In the previous section, we saw that QCD includes interactions among gluons because the gauge symmetry is non-abelian. Indeed, QCD has curious and notable characteristics arisen from three and four point gluon interactions. One significant phenomenon concerning to HIC is the color confinement which is understood qualitatively with QCD.

Quarks and gluons are not observed by themselves. This behavior is reflecting the asymptotic freedom of QCD. Asymptotic freedom is discovered in the early 1970s [30, 31] and it is confirmed experimentally via an electron-proton deep inelastic scattering [32]. It is the nature that the coupling constant of the interaction become weaker when a momentum transfer between interacting particles increases. It means that the interaction becomes weaker as two particles come near to each other.

One can find the asymptotic freedom of QCD with the Callan-Symanzik equation [33]. The renormalization group equation of QCD is given by

$$\frac{d}{d\log(Q/M)} g = \beta(g), \tag{3}$$

where Q is the transformed momentum, the β-function is $\beta(g) = -(11 - 2n_f/3)g^3/(4\pi)^2$ with the number of flavor n_f and M is an arbitrary renormalization point. The β-function is analyzed with an one-loop gluon self-energy. Unlike in the case of quantum electrdynamics, the gluon self energy includes contributions from gluon loops which are permitted by gluon three and four point vertices [34]. Contributions of gluon loops are $-11g^3/(4\pi)^2$ and they makes the QCD β-function is negative because n_f takes six at most. Therefore, the QCD running coupling constant $\alpha_s(Q) = g^2(Q)/4\pi$ becomes small as Q increases. We confirm that QCD has the asymptotic freedom.

Now let us consider the phenomenon that colored particles do not appear by themselves. At low temperature and low chemical potential, quarks and gluons compose hadrons and color charges cannot be observed. Suppose a virtual experiment to leave one quark included in a hadron from the hadron. The more the distance becomes longer, the interaction on the quark becomes more stronger. It demands an infinite energy to leave the quark from the hadron for infinite distance, and thus it is impossible to take out the quark. If one continues to leave the quark, the quark and hadron are converted to two hadrons to release the stocked energy when the distance becomes some extent. As a result, one cannot make a single colored particle state. QCD has the asymptotic freedom, and thus it has the characteristics mentioned above. One finds that QCD respects the non-observability of a single quark or a single gluon.

2.1.2 QCD Scale Parameter Λ_{QCD}

QCD has an important parameter Λ_{QCD} called the scale parameter of QCD. We introduce Λ_{QCD} in this subsection.

One obtains a solution of the renormalization group equation Eq. (3) as

$$\alpha_s(Q) = \frac{\alpha_s(M)}{1+(11-2n_f/3)(\alpha_s(M)/2\pi)\log(Q/M)}. \tag{4}$$

It is convenient to remove the dependence of the renormalization point by introducing a scale parameter Λ_{QCD}. Λ_{QCD} is defined to satisfy

$$1 = \frac{g^2}{8\pi}\left(11-\frac{2}{3}n_f\right)\log\frac{M}{\Lambda_{QCD}}. \tag{5}$$

With the QCD scale parameter, $\alpha_s(Q)$ is rewritten as

$$\alpha_s(Q) = \frac{2\pi}{(11-2n_f/3)\log(Q/\Lambda_{QCD})}. \tag{6}$$

In Eq. (6), one can easily confirm that the QCD coupling constant becomes small as Q increases. From the experimental measurements of $\alpha_s(Q)$, Λ_{QCD} is estimated about 200MeV. One can guess a energy region where a perturbative QCD is justified with the value of Λ_{QCD}. When Λ_{QCD}=200MeV and n_f=2, $\alpha_s(Q)$ is roughly estimated as 0.4 for $Q = 1$GeV and 0.3 for $Q = 2$GeV. It implies that the perturbative analysis seems to be justified when a considered energy scale is bigger than one GeV [84].

2.2 Deconfined Medium

In this section, we make a short review of the deconfined medium, QGP. Deconfinement is closely related to a phase transition of the QCD vacuum. We explain several features of the phase transition and evidences of quark-gluon plasma produced in HIC.

We find that the colored particle is not observed by itself in Section 2.1.1. At low temperature T and low chemical potential μ, partons are confined in hadrons which are colorless states. However, if the temperature or the baryon chemical potential become larger than the QCD scale parameter $\Lambda_{\rm QCD} \approx 200\text{MeV}$, a longer range strong interaction seems to be permitted. In addition, the longer range strong interaction is expected to receive the Debye screening by colored plasma once the deconfined medium produced. The Debye screening makes the interaction be short ranged. This is the reason why colored states are expected to arise when the temperature or the chemical potential become large, although a single parton cannot be observed [35].

Deconfinement is related to a phase transition of the QCD vacuum which is a ground state of QCD. To investigate the QCD phase structure, effective theories of QCD and numerical simulations of a field theory which is defined on a discretized finite volume Euclidean space make significant roles. In the case of the continuous field theory, the first-order phase transition on the (T,μ) plane in the Nambu-Jona-Lasinio (NJL) model which is an effective model of QCD was observed in 1989 [36]. The phase transition is a restoration of the chiral symmetry The chiral symmetry is broken in zero or low temperature region and restored in high temperature region. It implies that the chiral phase transition seems to be related to the deconfinement phase transition.

The field theory defined on the discretized Euclidean space is called a lattice QCD. Lattice QCD numerical simulations under various conditions reveal that the phase transition along the temperature axis is a cross-over phase transition [85]. The cross-over phase transition has a feature that its order parameter which determines the phase changes without discontinuity. The cross-over phase transition does not have a clear phase boundary, and thus the deconfinement phase transition temperature is called the pseudo critical temperature $T_{\rm c}$. $T_{\rm c}$ is estimated around 170MeV in a lattice QCD numerical simulation [85]. In ultra-relativistic HIC, a chemical potential of the produced hot state is almost zero, and thus we mainly consider the dynamics on the temperature axis above in the rest of this paper.

The hot medium under the deconfined state is predicted by knowledge of thermal field theories. Experimentally, an azimuthal anisotropy of hadrons and a yield suppression of J/ψ are observed in HIC [3]. An azimuthal anisotropy observed in HIC is called flow. Flows of several hadrons are observed and ratios of flows over the number of constituent quarks (three for baryons and two for mesons) are consistent with each other. This result is known as "quark number scaling" and considered as the evidence of the production of QGP in ultra-relativistic HIC [37, 38]. The suppression of J/ψ which is a $c\bar{c}$ state is observed and also considered as a support of the formation of QGP. The suppression is caused by the Debye screening of a long range interaction between charm and anti-charm [39]. A numerical simulation based on a perfect fluid model of QGP well reproduces the observed hadron flows [12, 13] and this result suggests that the produced QGP is strongly coupled. These results support the production of the strongly coupled deconfined hot medium in ultra-relativistic heavy ion collisions.

2.3 Electromagnetic Probes in HIC

We make a short review on electromagnetic probes observed in HIC. A strong point of electromagnetic probes is that electromagnetic signals emitted from the deconfined medium can be direct signals of the deconfined medium. Numerical simulations of hydrodynamics show that a typical size of produced QGP is 10fm at most. A size of the hot hadron medium which appears at the latter stage of HIC is the order of 10fm. Therefore, electromagnetic probes can be direct signals when their mean free path is larger than $\mathscr{O}(10)$fm. The mean free path of photon l_γ which propagates in the hot charged medium can be estimated as following procedure. The mean free path is an average length between two successive scatterings. It becomes smaller as a density of charged particles ρ increases or a typical cross section σ becomes larger. The mean free path is defined as $l_\gamma = 1/\rho\sigma$. In gold-gold collisions at a $\sqrt{s} = 200$GeV, ρ is roughly estimated high as $1[\text{fm}^{-3}]$ from experimental data [3] where $\sqrt{s}$ is a collision energy of two nucleons in a center of mass system. σ is also roughly estimated as 100μb experimentally. Therefore, the mean free path of photons is evaluated 100fm at least, and this mean free path is larger than the typical size of the hot medium. It means that once a real or virtual photon emitted, the photon does not receive the scattering by the strong interaction and penetrates the medium without disturbing.

Real and virtual photons from QGP are direct signals of the deconfined matter. Virtual photons are not physical states, and thus they are converted to dileptons which are lepton and anti-lepton pairs with the same invariant mass as virtual photons. By the way, these electromagnetic signals are produced via other mechanisms during the time evolution of HIC and other contributions are also important. Observed photons and dileptons are summation over various sources with time evolution effects. Therefore, it is difficult to extract an information of the deconfined medium from observed photons and one should consider several processes carefully. Now, let us consider main production dynamics, parton-parton scatterings, thermal radiations from QGP and photo productions from hadrons.

2.3.1 Parton-Parton Scattering

First, we consider the parton scattering. Parton is a generic name of particles which interact by the color changing interaction. Partons compose of nucleons. In ultra-relativistic heavy ion collisions, nuclei are accelerated as almost the speed of light and constituent quarks have high momenta. At the moment of the collision of two nuclei, most components of nuclei pass through and some partons collide. When a quark and an anti-quark interact, they are converted to a virtual photon γ^*. Emitted γ^*s are converted to lepton pairs, and this mechanism to produce dileptons at the initial stage of collision is called the Drell-Yan process [40]. Not only dileptons, photons are also produced via parton scatterings such as $qg \to q\gamma$. These photons produced via parton scatterings are called prompt photons. Partons with high momenta behave as free particle owing to the asymptotic freedom, and thus their contribution for total yields are estimated with the perturbative QCD. The photon momentum dependence of the yield arisen from parton scatterings has the negative power of momentum. In contrast, the dependence of the thermal radiation is the negative exponential, and thus parton scatterings dominate the total yield in higher momentum region.

2.3.2 Radiation from Hot Media

Next, we consider thermal radiations of photons and dileptons. After the collision, most components of nuclei pass away but a high energy density is produced between two nuclei. After a extremely short time estimated about 1fm/c, the high energy density is converted to the quark-gluon plasma at a local thermal equilibrium state. The local thermal equilibrium means that the whole QGP is not the static matter at the constant temperature but each micro part of the QGP is static and has the temperature. One can evaluate photon and dilepton productions as summation over contributions of thermal radiation of each micro part of the QGP.

As the QGP expands, it cools down and turns to be the hadronic matter. Even the hadrons are coupled strongly, and one can evaluate contributions of coupled hadrons as thermal radiations.

Thermal radiation rates of hot media of photons $d\mathrm{N}^{\gamma}/d^3qd^4x$ and dileptons $d\mathrm{N}^{l^+l^-}/d\omega d^3qd^4x$ are evaluated as

$$\omega\frac{d\mathrm{N}^{\gamma}}{d^3qd^4x} = -\frac{1}{(2\pi)^3}\frac{1}{\mathrm{e}^{\beta\omega}-1}\mathrm{Im}\Pi^{R,\mu}_{\mu}(\omega,\boldsymbol{q}), \tag{7}$$

$$\frac{d\mathrm{N}^{l^+l^-}}{d\omega d^3qd^4x} = -\frac{\alpha}{12\pi^4}\frac{1}{Q^2}\frac{1}{\mathrm{e}^{\beta\omega}-1}\mathrm{Im}\Pi^{R,\mu}_{\mu}(\omega,\boldsymbol{q}), \tag{8}$$

where $Q_\mu = (\omega,\boldsymbol{q})$ is a four momentum of the photon, α is a fine structure constant and $\Pi_{\mu\nu}$ is the photon self energy, respectively [16–18]. Eqs. (7) and (8) are correct to all order of the strong coupling and the leading order of α.

One can evaluate thermal radiation rates of QGP and even the hadronic hot medium by Eqs. (7) and (8). Analyses of thermal rates are converted to a problem how to evaluate the photon self energy. We discuss details in Section 3.4.1.

Again, the photon momentum dependence of the yield from the thermal radiation has the negative exponential, and thus it is expected that the total yield is dominated by radiations in lower momentum region if the hot medium exists.

The hadronic matter continues to expand and finally interactions among composed hadrons disappear. These hadrons are called final state hadrons. Some of them decay with photon or dilepton and these electromagnetic particles also contribute to total spectra.

2.4 Experimental Data of Electromagnetic Probes

In this subsection, we make a short review of experimental data concerning to photons and dileptons in HIC. We discuss quantities called “yield” and “flow”. These quantities in ultra-relativistic HIC are measured by two colliders with different energies, one is Relativistic Heavy Ion Collider (RHIC) at Brookhaven National Laboratory and another one is Large Hadron Collider (LHC) at the European Organization for Nuclear Research.

The yield is the amount of observed photons or dileptons. The photon production yield is plotted versus the photon transverse momentum. In HIC, the longitudinal direction is defined along a beam axis and transverse directions are defined as orthogonal to the transverse direction. The dilepton production yield is plotted versus the dilepton invariant mass. These yields are compared to proton-proton collision data which is considered medium effects are negligible, or small.

The flow is the other important observable. In HIC, a following situation is often occurred. When one observes particles emitted for two directions in some plane, the typical momentum of particles along one direction is larger than the one of another direction. The flow is the parameter to evaluate this anisotropy. To consider the anisotropy, we define azimuthal angles of reaction planes in the laboratory frame Φ^n where the positive integer n expresses n-th azimuthal angle of the reaction plane. This angle is evaluated with experimental data as

$$\Phi^n = \frac{1}{n}\tan^{-1}\frac{\sum_i \omega_i \sin n\phi}{\sum_i \omega_i \cos n\phi}, \tag{9}$$

where the sum goes over the ith particles and ω_i is the weight of the ith particle. The azimuthal distribution of particle production is analyzed with Φ^n in terms of the Fourier expansion as

$$\frac{d\mathrm{N}}{d\phi} \propto 1 + 2\sum_{n=1}^{\infty} v_n \cos[n(\phi - \Phi^n)], \tag{10}$$

with the azimuthal angle ϕ. v_1 and v_2 are called direct flow and elliptic flow, respectively.

Anisotropies are important observables to investigate the dynamics of HIC. The non-zero pion elliptic flow in Au+Au collisions at $\sqrt{s} = 200\mathrm{GeV}$ was observed in RHIC [3] and analyses with the hydrodynamics well reproduced data [12]. It is considered as an evidence that the QGP produced in RHIC is strongly coupled. Let us discuss the mechanism how the anisotropy is produced in HIC. Consider the moment of two nuclei collide. It is a rare event that two nuclei collide in the situation where centers of nuclei are along the same axis. We call this collision as the central collision. In most cases, two nuclei collide out of alignment. Not in the case of central collisions, the produced QGP has asymmetric shape, like a shape of almond as shown in Fig. 1(a). Fig. 1 is taken from the reference [52]. In Fig. 1(a), solid circles express nuclei and and the dashed ellipsoid expresses the QGP. We suppose the produced QGP behaves like the fluid. Then edges of the almond-shaped QGP have zero pressure and the center of the almond-shaped medium has the highest pressure. Therefore, the pressure gradient along the minor axis direction is larger than one along the major axis direction. Parts of the medium expand along the minor axis direction get larger momenta compared to the major axis direction. Therefore, emitted particles for the minor axis direction have the tendency to obtain higher momenta than ones of particles emitted for the major axis direction. This makes the anisotropy called the elliptic flow.

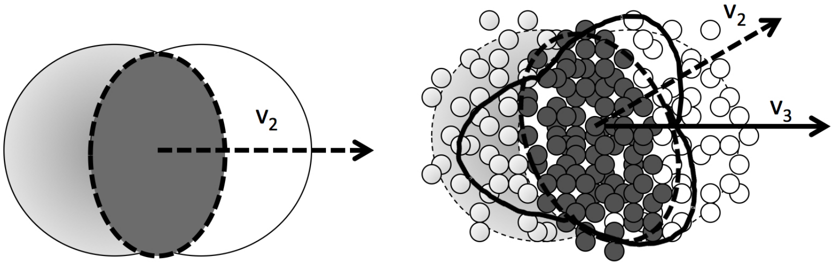

(a) Elliptic flow from a smooth almond-shaped initial state.

(b) Elliptic and triangular flows from fluctuated initial state.

Figure 1: Schematic diagram of origins of azimuthal anisotropies (a) v_2 and (b) v_3 [52].

We also explain a mechanism how the triangular anisotropy arises. The nuclear density is saturated in heavy nuclei but positions of nucleons are fluctuated in each collision event. If the distribution of nucleons as the triangular shape as illustrated in Fig. 1(b), there are three directions whose pressure gradients become larger than other directions. The triangular anisotropy is produced via the initial fluctuation of the nucleon distribution.

Anisotropic flow of hadrons are well studied in HIC. The triangular anisotropy and other higher anisotropies are already observed in HIC. Owing to the difficulty of analysis, however, only the photon flow is observed at present.

2.4.1 Real Photon

Let us discuss experimental data of photons in HIC. In Fig. 2, we show photon production yields in Au+Au collisions at $\sqrt{s} = 200$GeV (RHIC,left panel) and Pb+Pb collisions at $\sqrt{s} = 2.76$TeV (LHC, right panel). Figures are taken from Refs. [7, 8].

In Fig. 2, data are compared to proton-proton collisions data with corrections. In lower transverse momentum regions, observed data beyond proton collision fits. In general, thermal photons emitted from hot media have the tendency to occupy the total yield in smaller momentum region than ones of photons produced by hard initial scatterings. Therefore, these enhancements observed by PHENIX and ALICE seem to be the large contribution of hot media. Furthermore, the phenomenological numerical analysis based on the hydrodynamics and the perturbative QCD underestimates the photon yield by the factor two [41]. It implies the importance of the non-perturbative analysis of radiation from the strong coupled QGP.

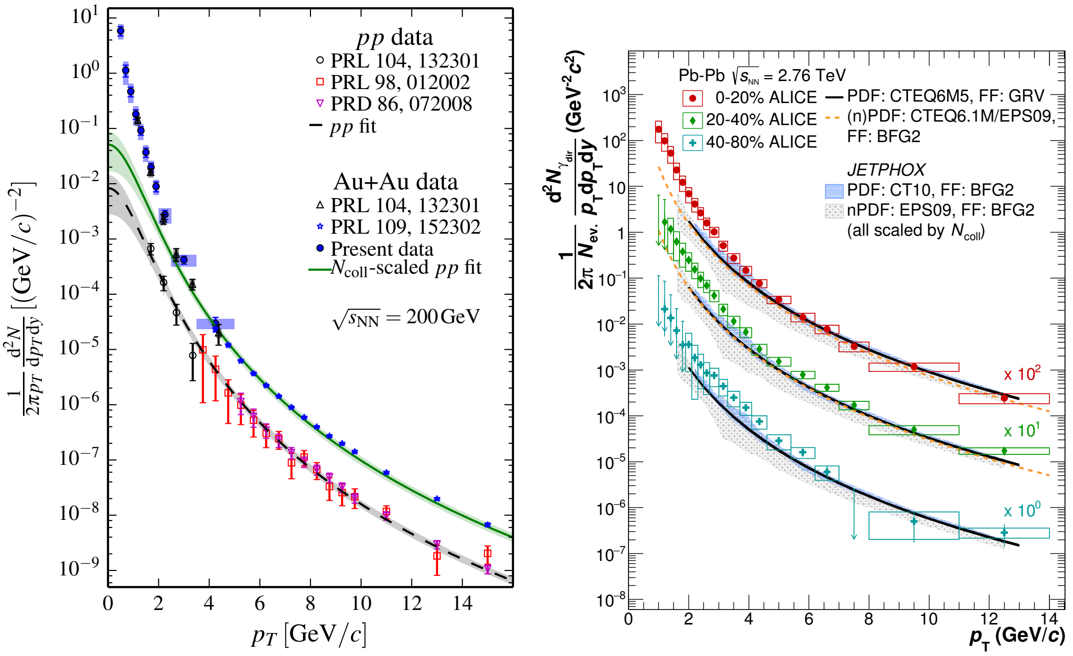

(a) Photon production yields measured by PHENIX in Au+Au collisions at $\sqrt{s} = 200$GeV [7].

(b) Photon production yields measured by ALICE in Pb+Pb collisions at $\sqrt{s} = 2.76$TeV [8].

Figure 2: Photon production yields measured in HIC.

One can estimate a useful parameter called the inverse slope parameter [43, 44]. We define a transverse mass M_{T} as $M_{\mathrm{T}} = \sqrt{m^2 + p_{\mathrm{T}}^2}$ with the mass of considered particle m and its transverse momentum p_{T}. Obtained production yields of various particles are well described by an exponential in M_{T} or $M_{\mathrm{T}} - m$,

$$\frac{1}{2\pi p_{\mathrm{T}}}\frac{d^2N}{dp_{\mathrm{T}}dy} \propto \exp(-M_{\mathrm{T}}/T_{\mathrm{slope}}), \tag{11}$$

with the inverse slope parameter T_{slope}. y is a rapidity which is corresponding to the length along the beam direction,

$$y = \frac{1}{2}\ln\frac{\omega + p_{\mathrm{beam}}}{\omega + p_{\mathrm{beam}}}. \tag{12}$$

Inverse slope parameters of photons are estimated as 221MeV for RHIC and 297MeV for LHC.

The anisotropies of photons are also measured by PHENIX collaboration [11]. The data of photon v_2 and v_3 are shown in Fig. 3. Figures are taken from Ref. [11]. Observed photon elliptic flow is not zero and it is comparable to the pion v_2. It is the confusing result because once photons are emitted from the hot medium, they do not interact with the medium any more. Therefore, photons do not receive the kick from the expanding medium. Nevertheless, the observed anisotropy is quite large. It

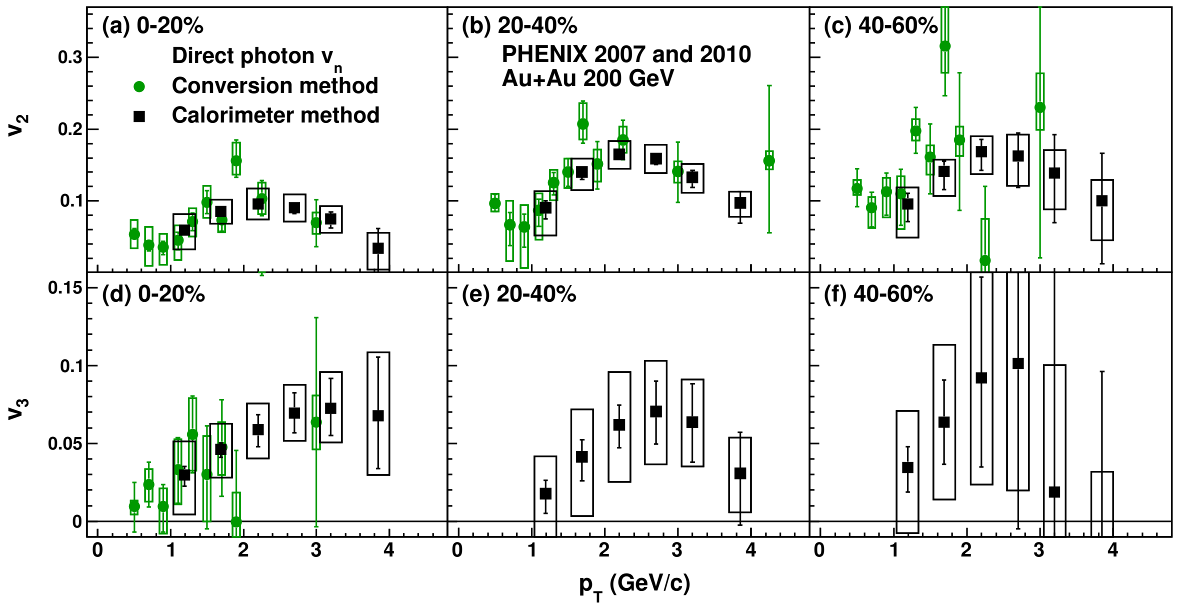

Figure 3: Direct photon v_2 and v_3 for different centralities obtained by PHENIX collaboration [11].

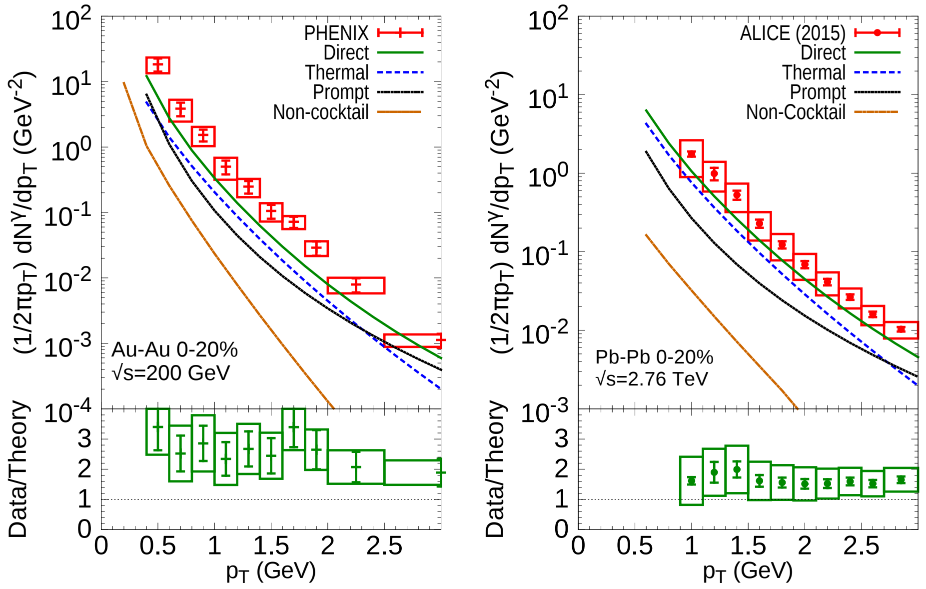

(a) Numerical simulation of photon production yield in Au+Au collisions at $\sqrt{s} =$ 200GeV [41].

(b) Numerical simulation of photon production yield in Pb+Pb collisions at $\sqrt{s} =$ 2.76TeV [41].

Figure 4: Photon production yields evaluated with the hydrodynamics and the perturbative photon rate [41]

seems that the photon production from the later stage of the time evolution of HIC has the relatively large contribution.

From experimental data Fig. 4, one can estimate that the hot medium around the pseudo critical temperature emits the large amount of photons. On the other hand, the numerical analysis based on the hydrodynamics reveals that the anisotropy of the media almost saturates till 10fm. In fact, the numerical analysis of the photon elliptic flow of thermal media and final state hadrons are comparable to data. However, the numerical simulation does not reproduce experimental results when one adds the contribution of the prompt photon which is the contribution of initial parton scatterings. It is surprising that the contribution of prompt photons which is smaller by the order two in lower transverse momentum region suppresses the elliptic flow [41]. These problem concerning to the yield and the anisotropies are called the photon v_2 puzzle.

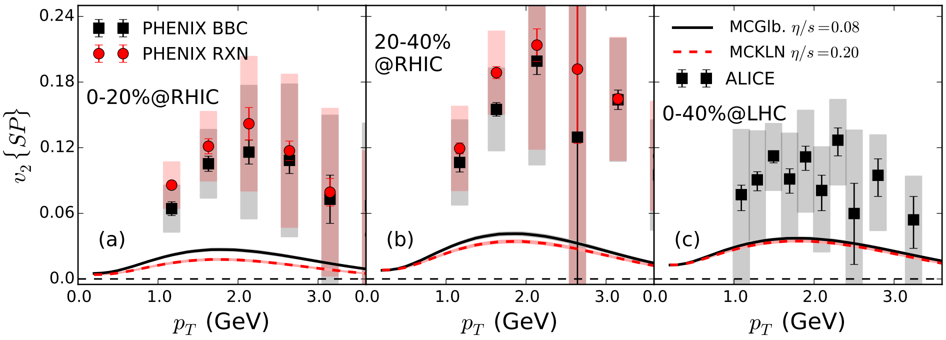

(a) Photon elliptic flow v_2.

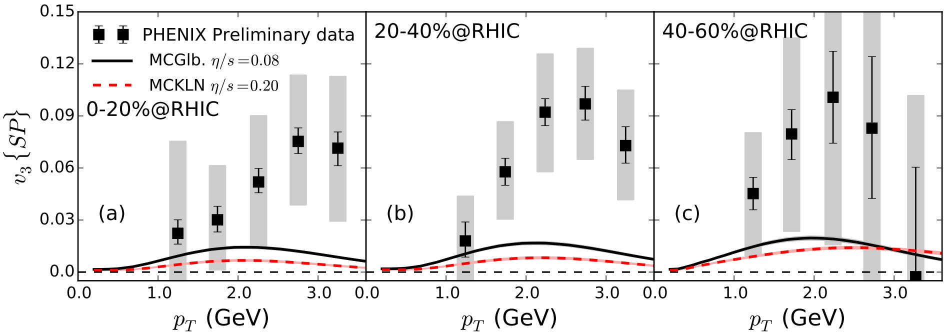

(b) Photon triangular flow v_3.

Figure 5: Numerical results of photon v_2 and v_3 evaluated with a hydrodynamics and a perturbation theory [42].

To solve the puzzle, a phenomenological mechanism is proposed which considers the effect of the strong magnetic field in HIC. In not-central ultra-relativistic heavy ion collisions, these situations can be considered as two large electromagnetic currents propagate out of alignment. Currents generate the magnetic field, and thus there is a possibility that the strong magnetic field arises at the moment of impact [45]. The direction of the strong magnetic field has the correlation of the direction of the photon elliptic flow because they share the production dynamics. Furthermore, when the photon propagate in the strong magnetic field, its strength gets direction dependencies on parallel to or horizontal to the magnetic field [46–48]. This mechanism surely enhances the elliptic anisotropy. However, the observed large v_3 cannot be understood by the mechanism because v_3 directions are determined by the initial fluctuation and it does not have the correlation to the direction of the magnetic field. The observation of the large photon v_3 is meaningful and demands a new mechanism.

Finally, we show numerical results of photon production yield in Fig. 4 and flows in Fig. 5. Fig. 4 are taken from Ref. [41] and Fig. 5 are taken from Ref. [42]. They are evaluated based on the hydrodynamics and the perturbative analysis. One finds that the numerical results of yield and flows are still smaller than the observed ones. These results indicate an incompleteness of the previous model calculations.

2.4.2 Dilepton

At the end of this section, we discuss dilepton productions in HIC. In Fig. 6, dielectron production yields in Au+Au collisions at $\sqrt{s} = 200$GeV are shown [9, 10]. Dielectron yields are observed by two collaborations PHENIX and STAR. Spectra are taken form Refs. [9, 10].

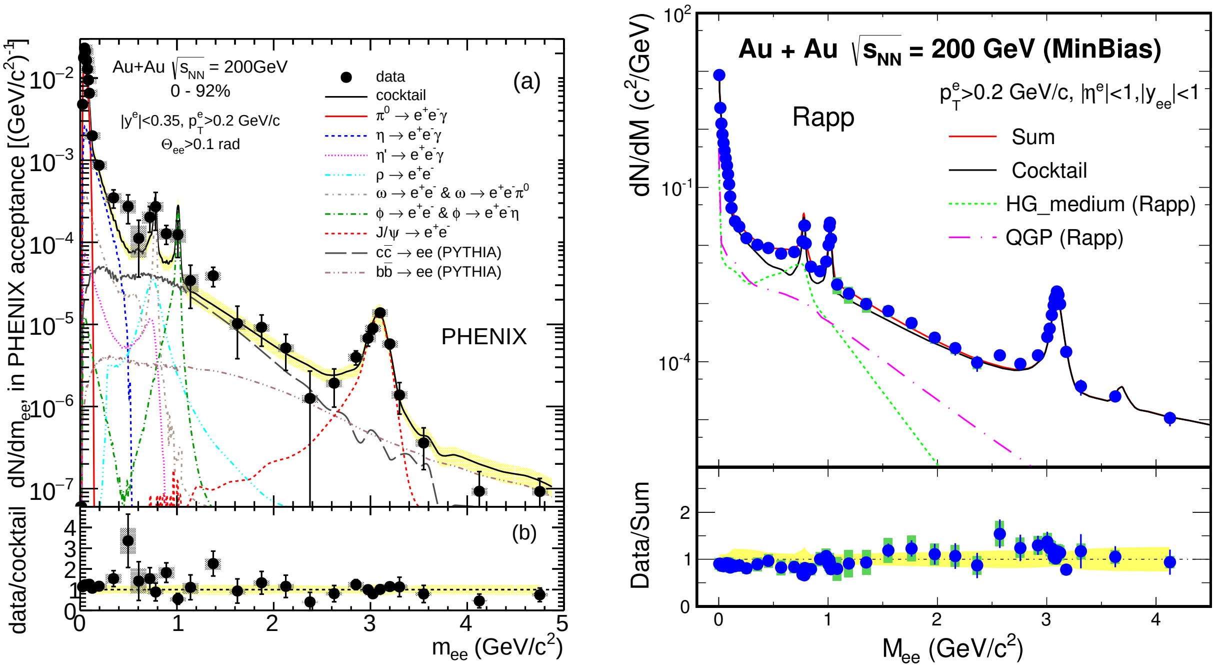

(a) Dielectron production yield measured by PHENIX collaboration [9] in Au+Au collisions at $\sqrt{s} = 200$GeV.

(b) Dielectron production yield measured by STAR collaboration [8] in Au+Au collisions at $\sqrt{s} = 200$GeV.

Figure 6: Dilepton yields measured in RHIC.

Data are compared with “cocktail” which is estimated from final state hadrons. Two data show enhancements in lower invariant mass regions <1GeV. These enhancements are considered as contributions from hot media.

A phenomenological model based on a vector dominance model is succeed to reproduce observed enhancements [49]. In Ref. [49], the contribution from the deconfined medium is evaluated perturbatively. The vector dominance model is the effective theory of the hadronic interaction. It insists that the ρ meson spectrum is altered via thermal effects and the spectral function reaches to the one of a_1 which is the chiral partner of ρ. The dilepton production “rate” per unit time per unit volume is evaluated by the effective model and the rate is integrated with a simple dynamical model of the medium. Because dilepton yields are reproduced by the effective model, it is claimed that the dilepton production yield can be a signal of the chiral phase transition. However, the complex dynamics of HIC is reflected on the dilepton yield, and thus it is still difficult to extract the spectral function of ρ from the obtained data. In addition, the numerical result is obtained with the too simple model which treats the expanding fireball as the uniform cylinder [50, 51]. Analyses with a more realistic dynamical model is desirable, and the improvement of dynamical model has to change the yield. It is also expected that the numerical result of the yield is changed by substituting the non-perturbative dilepton production rate of the QGP for the dynamical model. It seems that it is valuable to analyze the dilepton production yield with the more realistic model and the non-perturbative analysis of dilepton production from QGP.

3 Theoretical Analysis of Thermal Photon and Dilepton Production Rates

Theoretical formalism concerning thermal photon and dilepton production rates is overviewed in this section. We start this section with the fundamental formalism of the thermal field theory. Next, the hard thermal loop resummation technique is overviewed. The resummation technique plays important roles to evaluate photon and dilepton production rates perturbatively. Then we make a brief review on thermal radiation rates of electromagnetic probes from the static medium. Perturbative production rates of photons and dileptons are also given in this part.

3.1 Thermal Field Theory

In this section, we make a brief review on the quantum thermal field theory. It help readers to understand the following discussion about thermal photon production rate from the hot medium.

In statistical mechanics, it is well known that when a system is in equilibrium, the parameter T called temperature can be defined. Even in the quantum field theory, the parameter T controls property of static medium. I will review various correlators, such as retarded and Matsubara correlators, which will play important roles in the analysis of thermal photon and dilepton. This review is based on Refs. [19, 86, 87].

3.1.1 Imaginary Time Formalism

We explain about an imaginary time formalism in this section. In thermal field theory, one can express the partition function Z as a path integral. Though there is other formalism, we obey the path integral formalism of the thermal field theory and the formalism is discussed in this section.

First we consider a boson system. Let $\hat{H}$ be the Hamiltonian of the system, μ_i and N_i be chemical potential and conserved charge of particle species i, respectively. The partition function of the boson system is given by

$$\begin{aligned} Z &= \mathrm{Tr}\, \mathrm{e}^{-\beta(\hat{H}-\sum_i \mu_i \hat{N}_i)} \\ &= \sum_a \int d\phi_a \langle \phi_a | \mathrm{e}^{-\beta(\hat{H}-\sum_i \mu_i \hat{N}_i)} | \phi_a \rangle, \end{aligned} \tag{13}$$

with $\beta = 1/T$. The state $|\phi_a\rangle$ is Heisenberg state and the trace is taken over all states. We define the density matrix $\hat{\rho} = \mathrm{e}^{-\beta(\hat{H}-\sum_i \mu_i \hat{N}_i)}$.

Let π be a conjugate momentum to the field ϕ. States $|\phi\rangle$ and $|\pi\rangle$ are eigenstates of field operators

$\hat{\phi}(0,\boldsymbol{x})$ and $\hat{\pi}(0,\boldsymbol{x})$ respectively. They construct complete systems and satisfy orthogonality,

$$\begin{aligned}
&\hat{\phi}(0,\boldsymbol{x})|\phi\rangle = \phi(\boldsymbol{x})|\phi\rangle,\ \int d\phi(\boldsymbol{x})|\phi\rangle\langle\phi| = 1,\ \langle\phi_a|\phi_b\rangle = \delta(\phi_a(\boldsymbol{x})-\phi_b(\boldsymbol{x})),\\
&\hat{\pi}(0,\boldsymbol{x})|\pi\rangle = \pi(\boldsymbol{x})|\pi\rangle,\ \int \frac{d\pi(\boldsymbol{x})}{2\pi}|\pi\rangle\langle\pi| = 1,\ \langle\pi_a|\pi_b\rangle = \delta(\pi_a(\boldsymbol{x})-\pi_b(\boldsymbol{x})).
\end{aligned} \tag{14}$$

In addition, $|\phi\rangle$ and $|\pi\rangle$ satisfy

$$\langle\phi|\pi\rangle = \exp\left(i\int d^3x\, \pi(\boldsymbol{x})\phi(\boldsymbol{x})\right). \tag{15}$$

Now let us express the partition function Eq. (13) in the path integral formalism. In the following discussion, the conserved charge is ignored for simplicity. When the Hamiltonian does not depend on time explicitly, the transition amplitude that an initial state $|\phi_a\rangle$ at $t=0$ transits to a final state $|\phi_a\rangle$ at $t=t_f$ is given by

$$\begin{aligned}
\langle\phi_a|\mathrm{e}^{-i\hat{H}t_f}|\phi_a\rangle = \lim_{N\to\infty}\int\left(\prod_{i=1}^{N} d\pi_i d\phi_i/2\pi\right)\langle\phi_a|\pi_N\rangle\langle\pi_N|\mathrm{e}^{-iH\Delta t}|\phi_N\rangle\langle\phi_N|\pi_{N-1}\rangle\\
\times\langle\pi_{N-1}|\mathrm{e}^{-iH\Delta t}|\phi_{N-1}\rangle\cdots\times\langle\phi_2|\pi_1\rangle\langle\pi_1|\mathrm{e}^{-iH\Delta t}|\phi_1\rangle\langle\phi_1|\phi_a\rangle,
\end{aligned} \tag{16}$$

with $\phi_{N+1}=\phi_a$ and $\Delta t = t_f/N$. In the limit of $\Delta t \to 0$,

$$\begin{aligned}
\langle\pi_i|\mathrm{e}^{-i\hat{H}\Delta t}|\phi_i\rangle \simeq&\langle\pi_i|1-i\hat{H}\Delta t|\phi_i\rangle = \langle\pi_i|\phi_i\rangle(1-iH_i\Delta t)\\
=&(1-iH_i\Delta t)\exp\left(-i\int d^3x\pi_i(\boldsymbol{x})\phi_i(\boldsymbol{x})\right),
\end{aligned} \tag{17}$$

where $H_i = \int d^3x\mathscr{H}(\pi_i(x),\phi_i(x))$ is defined such that every $\hat{\pi}$ is on the left side of $\hat{\phi}$. Eq. (16) becomes

$$\begin{aligned}
\langle\phi_a|\mathrm{e}^{-i\hat{H}t_f}|\phi_a\rangle &= \lim_{N\to\infty}\int\left(\prod_{i=1}^{N}d\pi_i d\phi_i/2\pi\right)\delta(\phi_1-\phi_a)\\
&\quad\times\exp\left[-i\Delta t\sum_{j=1}^{N}\int d^3\left[\mathscr{H}(\pi_j,\phi_j)-\pi_j(\phi_{j+1}-\phi_j)/\Delta t\right]\right]\\
&\equiv \int[d\pi]\int_{\phi(0,\boldsymbol{x})=\phi_a(\boldsymbol{x})}^{\phi(t_f,\boldsymbol{x})=\phi_a(\boldsymbol{x})}[d\phi]\exp\left[i\int_0^{t_f}dt\int d^3x\left(\pi(t,\boldsymbol{x})\frac{\partial\phi(t,\boldsymbol{x})}{\partial t}-\mathscr{H}(\pi,\phi)\right)\right]
\end{aligned} \tag{18}$$

with Eqs. (14), (15) and (17). $[d\pi]$ and $[d\phi]$ are measures of functional integrals.

Now we substitute Eq. (18) for Eq. (13) and introduce the “imaginary time” $\tau = it$ in Eq. (18).

Summing over ϕ_a, one obtains the partition function in path integral formalism,

$$Z = \int [d\pi] \int_{\text{periodic}} [d\phi] \exp\left[\int_0^\beta d\tau \int d^3x \left(i\pi(t,\boldsymbol{x}) \frac{\partial \phi(\tau,\boldsymbol{x})}{\partial \tau} - \mathscr{H}(\pi,\phi) \right) \right], \tag{19}$$

where "periodic" means $\phi(0,\boldsymbol{x}) = \phi(\beta,\boldsymbol{x})$ and $\beta = it_f$.

One can calculate the partition function of a fermion system as in the similar manner for the case of boson system. The fermion field ψ becomes the Grassmann number in the path integral, and thus the boundary condition of the path integral becomes "anti-periodic", $\psi(\beta,\vec{x}) = -\psi(0,\vec{x})$.

In the quantum field theory, the two point correlation of an arbitrary field $\hat{O}$ is quite important. We define the imaginary time correlation function $G(\tau,\tau';\boldsymbol{x},\boldsymbol{x}')$ as

$$\begin{aligned} G\left(\tau,\tau';\boldsymbol{x},\boldsymbol{x}'\right) =& \langle \hat{O}(\tau,\boldsymbol{x}) \hat{O}(\tau',\boldsymbol{x}') \rangle \\ =& \frac{1}{Z} \mathrm{Tr}\left[\hat{\rho} \hat{O}(\tau,\boldsymbol{x}) \hat{O}(\tau',\boldsymbol{x}') \right], \end{aligned} \tag{20}$$

where $\hat{\rho}$ is the density matrix and $\langle\rangle$ means to take the thermal average. As in the similar manner for the case of real time operators, the imaginary time transformation of $\hat{\phi}(\tau,\boldsymbol{x})$ and $\hat{\psi}(\tau,\boldsymbol{x})$ is defined as

$$\hat{\phi}(\tau,\boldsymbol{x}) = \mathrm{e}^{\hat{H}\tau} \hat{\phi}(0,\boldsymbol{x}) \mathrm{e}^{-\hat{H}\tau}, \ \hat{\psi}(\tau,\boldsymbol{x}) = \mathrm{e}^{\hat{H}\tau} \hat{\psi}(0,\boldsymbol{x}) \mathrm{e}^{-\hat{H}\tau}. \tag{21}$$

The boson correlation function G_B is defined as

$$G_B(\tau_1,\tau_2;\boldsymbol{x},\boldsymbol{y}) = Z^{-1} \mathrm{Tr}\left[\hat{\rho} T_\tau \left[\hat{\phi}(\tau_1,\boldsymbol{x}) \hat{\phi}(\tau_2,\boldsymbol{y}) \right] \right], \tag{22}$$

where T_τ is the imaginary time ordering operator. T_τ is acting on the multiproduct of the operator as

$$\mathrm{T}_\tau \left[\hat{\phi}(\tau_1,\boldsymbol{x}) \hat{\phi}(\tau_2,\boldsymbol{y}) \right] = \hat{\phi}(\tau_1,\boldsymbol{x}) \hat{\phi}(\tau_2,\boldsymbol{y}) \theta(\tau_1 - \tau_2) + \hat{\phi}(\tau_2,\boldsymbol{y}) \hat{\phi}(\tau_1,\boldsymbol{x}) \theta(\tau_2 - \tau_1). \tag{23}$$

Now let us prove $G_B(\tau,0;\boldsymbol{x},\boldsymbol{y}) = G_B(\tau,\beta;\boldsymbol{x},\boldsymbol{y})$. G_B should be periodic because the partition function of bosonic system is periodic. Owing to the time translational symmetry, one can take $\tau' = 0$ without loss of generality, and thus

$$\begin{aligned} G_B(\tau,0;\boldsymbol{x},\boldsymbol{y}) =& Z^{-1} \mathrm{Tr}\left[\mathrm{e}^{-\beta\hat{K}} \hat{\phi}(\tau,\boldsymbol{x}) \hat{\phi}(0,\boldsymbol{y}) \right] = Z^{-1} \mathrm{Tr}\left[\hat{\phi}(0,\boldsymbol{y}) \mathrm{e}^{-\beta\hat{K}} \hat{\phi}(\tau,\boldsymbol{x}) \right] \\ =& Z^{-1} \mathrm{Tr}\left[\mathrm{e}^{-\beta\hat{K}} \mathrm{e}^{\beta\hat{K}} \hat{\phi}(0,\boldsymbol{y}) \mathrm{e}^{-\beta\hat{K}} \hat{\phi}(\tau,\boldsymbol{x}) \right] = Z^{-1} \mathrm{Tr}\left[\mathrm{e}^{-\beta\hat{K}} \hat{\phi}(\beta,\boldsymbol{y}) \hat{\phi}(\tau,\boldsymbol{x}) \right] \\ =& Z^{-1} \mathrm{Tr}\left[\hat{\rho} T_\tau \left[\hat{\phi}(\tau,\boldsymbol{x}) \hat{\phi}(\beta,\boldsymbol{y}) \right] \right] = G_B(\tau,\beta;\boldsymbol{x},\boldsymbol{y}). \end{aligned} \tag{24}$$

G_B satisfies periodicity. When one supposes $\phi(0,\boldsymbol{y}) = \phi(\beta,\boldsymbol{y})$, the periodicity Eq. (24) is satisfied automatically.

Next we consider the imaginary time region of the boson correlator. The boson correlator satisfies

$$\begin{aligned} G_B(\tau,\beta;\boldsymbol{x},\boldsymbol{y}) =& Z^{-1}\mathrm{Tr}\left[\mathrm{e}^{-\beta\hat{K}}\hat{\phi}(\tau,\boldsymbol{x})\hat{\phi}(0,\boldsymbol{y})\right] = Z^{-1}\mathrm{Tr}\left[\mathrm{e}^{-\beta\hat{K}}\hat{\phi}(\tau,\boldsymbol{x})\mathrm{e}^{\beta\hat{K}}\mathrm{e}^{-\beta\hat{K}}\hat{\phi}(0,\boldsymbol{y})\right] \\ =& Z^{-1}\mathrm{Tr}\left[\mathrm{e}^{-\beta\hat{K}}\hat{\phi}(0,\boldsymbol{y})\hat{\phi}(\tau-\beta,\boldsymbol{x})\right] = Z^{-1}\mathrm{Tr}\left[\hat{\rho}T_\tau\left[\hat{\phi}(\tau-\beta,\boldsymbol{x})\hat{\phi}(0,\boldsymbol{y})\right]\right] \\ =& G_B(\tau-\beta,0;\boldsymbol{x},\boldsymbol{y}). \end{aligned} \tag{25}$$

It turns out that $G_B(\tau,\beta;\boldsymbol{x},\boldsymbol{y}) = G_B(\tau-\beta,0;\boldsymbol{x},\boldsymbol{y})$. From Eq. (25) the imaginary time region can be restricted to $[0,\beta]$, and thus the Fourier transform on the imaginary time leads to the discretized energy.

The Fourier transform of the boson correlation function is defined as

$$G_B(i\nu_n,\boldsymbol{p}) = \int_0^\beta d\tau \int d^3(x-y) G_B(\tau,0;\boldsymbol{x},\boldsymbol{y})\mathrm{e}^{i\nu_n\tau}\mathrm{e}^{-i\boldsymbol{p}\cdot(\boldsymbol{x}-\boldsymbol{y})}. \tag{26}$$

Because $G_B(\tau,0;\boldsymbol{x},\boldsymbol{y})$ is periodic on time, the energy of boson becomes discrete,

$$\nu_n = 2\pi nT, \tag{27}$$

with the integer n. The discretized energy, Eq. (27), is referred to *Matsubara frequency* of boson.

The correlation function of fermion G_F is defined as in the similar case of boson. Time ordered operator is acting on the products of fermion fields anticommutatively,

$$T_\tau[\hat{\psi}(\tau_1,\boldsymbol{x})\hat{\psi}(\tau_2,\boldsymbol{y})] = \hat{\psi}(\tau_1,\boldsymbol{x})\hat{\psi}(\tau_2,\boldsymbol{y})\theta(\tau_1-\tau_2) - \hat{\psi}(\tau_2,\boldsymbol{y})\hat{\psi}(\tau_1,\boldsymbol{x})\theta(\tau_2-\tau_1). \tag{28}$$

Therefore, $G_F(\tau,0;\boldsymbol{x},\boldsymbol{y}) = -G_F(\tau,\beta;\boldsymbol{x},\boldsymbol{y})$, $G_F(\tau,0;\boldsymbol{x},\boldsymbol{y}) = -G_F(\tau-\beta,0;\boldsymbol{x},\boldsymbol{y})$. $G_F(\tau,0;\boldsymbol{x},\boldsymbol{y})$ is antisymmetric on the imaginary time and the Matsubara frequency of fermion becomes $\nu_n = (2n+1)\pi T$. As in the similar case of the boson field, when one supposes the anti-periodic condition of the fermion field, $\psi(0,\boldsymbol{y}) = -\psi(\beta,\boldsymbol{y})$, the anti-periodicity of G_F is satisfied automatically. It is notable that finite temperature field theory can be formulated reasonably with both Minkowski metric and Euclidean metric. We defined the four momentum as

$$p_\mu = (i\nu_n,\boldsymbol{p}). \tag{29}$$

In this case, the metric becomes Minkowski's one. On the other hand, when the four momentum is defined as

$$p_\mu = (p_4,\boldsymbol{p}) = (\nu_n,\boldsymbol{p}), \tag{30}$$

with the real number ν_n, the thermal field theory has the Euclidean metric. Through the rest of the paper, the four momentum is defined like Eq. (29).

3.1.2 Matsubara Sum

In the imaginary time formalism, one often has to take a summation over the Matsubara frequency. We make a brief review on the sum in this subsection.

In the previous section, it is shown that the frequency of boson or fermion in Matsubara formalism takes integer time or half-integer time of $2\pi Ti$, respectively. As a result, the sum over fermion energy p_0 becomes the summation over the integer n,

$$T\sum_{n=-\infty}^{\infty} f\left(p_0 = i\nu_n = 2\pi(n+1/2)Ti\right), \tag{31}$$

where $f(p_0)$ is an arbitrary function of p_0. The sum over Matsubara frequencies like Eq. (31) is named the *Matsubara sum*. The Matsubara sum of boson is also given by

$$T\sum_{n=-\infty}^{\infty} f(p_0 = i\nu_n = 2\pi nTi). \tag{32}$$

The Matsubara sum can be evaluated by the following procedure. First, Eq. (31) is corresponding to the complex integral on the p_0 complex plane along the contour C in the Fig. 7(a),

$$T\oint_C \frac{dp_0}{2\pi i} f(p_0) \frac{\beta}{2} \tanh\frac{\beta p_0}{2}. \tag{33}$$

The path C can be transformed to C' in Fig 7(b), if $f(p_0)$ does not have a pole located near the imaginary axis. It should be emphasized that the complex integral along the contour C' is determined by the singularity structure of $f(p_0)$.

Let us calculate the Matsubara sum Eq. (31) in a simple case. Suppose $f(p_0) = 1/p_0^2 - \nu^2$ with the real constant ν. In this case, $f(p_0)$ has poles at $p_0 = \pm\nu$, and thus the Matsubara sum is evaluated as

$$\begin{aligned} T\sum_{-\infty}^{\infty} f(p_0 = i\nu_n = 2\pi(n+1/2)Ti) &= T\oint_C \frac{dp_0}{2\pi i} \frac{1}{p_0^2-\nu^2} \frac{\beta}{2} \tanh\frac{\beta p_0}{2} \\ &= T\oint_C \frac{dp_0}{2\pi i} \frac{1}{2\nu} \left[\frac{1}{p_0-\nu} - \frac{1}{p_0+\nu}\right] \frac{\beta}{2} \tanh\frac{\beta p_0}{2} \\ &= -\frac{1}{2\nu}\left[1 - \frac{2}{e^{\beta\nu}+1}\right]. \end{aligned} \tag{34}$$

In the boson case, Eq. (32) is also calculated as the complex integral,

$$T\oint_{C''} \frac{dp_0}{2\pi i} f(p_0) \frac{\beta}{2} \coth\frac{\beta p_0}{2}, \tag{35}$$

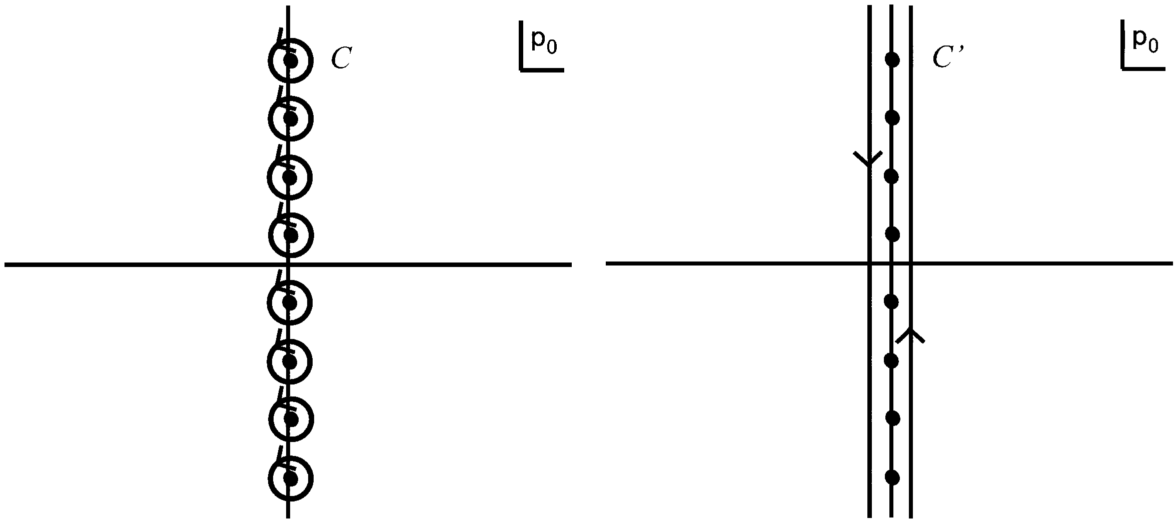

(a) Contour C (b) Contour C'

Figure 7: Contours on the p_0 plane for the Matsubara sum.

where the poles of $\coth(\beta p_0/2)$ are located on $p_0 = 2\pi n T i$.

3.1.3 Analytic Continuation of Imaginary Time Correlator

In this subsection we relate the imaginary time correlation function to the real time correlation function. The technique to obtain the real time correlator from the imaginary time correlator plays an essential role in analyses of thermal photons and dileptons. In the real time formalism, let $|n\rangle$ be a simultaneous eigenstate of a Hamiltonian H and a momentum $\boldsymbol{p}$. $|n\rangle$ has the energy eigenvalue E_n and the momentum eigenvalue $\boldsymbol{p}_n$ and forms a complete set of the system. Let D^+ be a two point correlation function of the fermion field defined as

$$iD^+(x-y) = \langle \hat{\psi}(x)\hat{\bar{\psi}}(y)\rangle = \frac{1}{Z}\sum_n \mathrm{e}^{-\beta E_n}\langle n|\hat{\psi}(x)\hat{\bar{\psi}}(y)|n\rangle. \tag{36}$$

Eq. (36) becomes

$$\langle \hat{\psi}(x)\hat{\bar{\psi}}(y)\rangle = \frac{1}{Z}\sum_{m,n} \mathrm{e}^{-\beta E_n}\langle n|\hat{\psi}(x)|m\rangle\langle m|\hat{\bar{\psi}}(y)|n\rangle. \tag{37}$$

The momentum $\hat{\boldsymbol{p}}$ plays a role of the generator of the three-dimensional coordinate transformation, the fermion field $\hat{\psi}(t,\boldsymbol{x})$ is related to $\hat{\psi}(t,\boldsymbol{0})$ with the generator,

$$\hat{\psi}(t,\boldsymbol{x}) = \mathrm{e}^{-i\hat{\boldsymbol{p}}\cdot\boldsymbol{x}}\hat{\psi}(t,\boldsymbol{0})\mathrm{e}^{i\hat{\boldsymbol{p}}\cdot\boldsymbol{x}}. \tag{38}$$

From Eq. (38), the matrix element of $\hat{\psi}$ is calculated to be

$$\langle n|\hat{\psi}(x)|m\rangle = \langle n|\mathrm{e}^{iHt}\hat{\psi}(0,\boldsymbol{x})\mathrm{e}^{-iHt}|m\rangle = \mathrm{e}^{i(E_n-E_m)t}\langle n|\hat{\psi}(0,\boldsymbol{x})|m\rangle = \mathrm{e}^{i(p_n-p_m)\cdot x}\langle n|\hat{\psi}(0)|m\rangle, \tag{39}$$

where $(p_n - p_m)\cdot x = (p_n - p_m)_\mu x^\mu$ and $x_\mu = (t, \boldsymbol{x})$ is a four coordinate. From Eqs. (37), (38) and (39), Eq. (36) is calculated as

$$iD^+(x-y) = \frac{1}{Z}\sum_{m,n} \mathrm{e}^{-\beta E_n} \mathrm{e}^{i(p_n - p_m)\cdot(x-y)} \langle n|\hat{\psi}(0)|m\rangle\langle m|\hat{\bar{\psi}}(0)|n\rangle, \tag{40}$$

and its Fourier transformed function $D^+(p)$ is given by

$$D^+(p) = \int d^4x \mathrm{e}^{ip\cdot x} D^+(x). \tag{41}$$

The spectral function $\rho^+(p)$ is defined as

$$\rho^+(p) = \frac{1}{Z}\sum_{m,n} \mathrm{e}^{-\beta E_n}(2\pi)^3\delta^4(p - p_m + p_n)\langle n|\hat{\psi}(0)|m\rangle\langle m|\hat{\bar{\psi}}(0)|n\rangle. \tag{42}$$

ρ^+ and D^+ are related to $iD^+(p) = 2\pi\rho^+(p)$.

Similarly, from the other fermion correlation function $D^-(x-y) = -\langle\hat{\bar{\psi}}(y)\hat{\psi}(x)\rangle$, the corresponding spectral function $\rho^-(p)$ is defined as

$$\rho^-(p) = -\frac{1}{Z}\sum_{m,n} \mathrm{e}^{-\beta E_m}(2\pi)^3\delta^4(p - p_m + p_n)\langle n|\hat{\bar{\psi}}(0)|m\rangle\langle m|\hat{\psi}(0)|n\rangle. \tag{43}$$

ρ^- and D^- are related to $iD^-(p) = 2\pi\rho^-(p)$. From Eqs. (42) and (43), one obtains

$$\rho^-(p) = -\mathrm{e}^{-\beta p^0}\rho^+(p). \tag{44}$$

From the thermal average of commutator of fields, the Green function $D^n(x-y)$ (n means *normal*) and the corresponding spectral function are defined as

$$D^n(x-y) = -i\langle[\hat{\psi}(x), \hat{\bar{\psi}}(y)]\rangle = D^+(x-y) + D^-(x-y), \tag{45}$$

$$\begin{aligned}\rho^n(p) =& iD^n(p)/2\pi = \rho^+(p) + \rho^-(p)\\ =&(1 - \mathrm{e}^{-\beta p_0})\rho^+(p) = -(\mathrm{e}^{\beta p_0} - 1)\rho^-(p).\end{aligned} \tag{46}$$

Next, we consider the retarded Green function $D^R(p)$ defined as

$$D^R(z) = \theta(z^0)D^n(z). \tag{47}$$

The retarded Green function is zero when $z^0 < 0$, it corresponds that no pole exists in the upper-half plane of p^0. Moreover, Fourier transform of the Heaviside step function is given by

$$\int_{-\infty}^{\infty} dz^0 \theta(z^0)\mathrm{e}^{ip^0 z^0} = \frac{i}{p^0 + i\varepsilon}, \tag{48}$$

where ε is the positive infinitesimal number. Therefore, the Fourier transform of the retarded Green function is evaluated as below,

$$\begin{aligned}
iD^R(p) &= \int d^4z \mathrm{e}^{ipz} iD^R(z) \\
&= \int d^4z \mathrm{e}^{ipz} \theta(z^0) iD^n(z) \\
&= \int d^4z \mathrm{e}^{ipz} \left(\int_{-\infty}^{\infty} \frac{dk^0}{2\pi} \frac{i}{k^0 + i\varepsilon} \mathrm{e}^{-ik^0 z^0} \right) \left(\int \frac{d\nu d^3k}{(2\pi)^4} 2\pi \rho^n(\nu, \boldsymbol{k}) \mathrm{e}^{-i(\nu z^0 - \boldsymbol{k}\cdot\boldsymbol{z})} \right) \\
&= \int d^4z \int_{-\infty}^{\infty} dk^0 \int \frac{d\nu d^3k}{(2\pi)^4} \frac{i}{k^0 + i\varepsilon} \rho^n(\nu, \boldsymbol{k}) \mathrm{e}^{-i[(\nu + k^0 - p^0) z^0 - (\boldsymbol{k} - \boldsymbol{p})\cdot\boldsymbol{z}]} \\
&= \int_{-\infty}^{\infty} dk^0 \int d\nu d^3k \frac{i}{k^0 + i\varepsilon} \rho^n(\nu, \boldsymbol{k}) \delta(\nu + k^0 - p^0) \delta^3(\boldsymbol{k} - \boldsymbol{p}) \\
&= -i \int d\nu \frac{1}{\nu - p^0 - i\varepsilon} \rho^n(\nu, \boldsymbol{p}).
\end{aligned} \tag{49}$$

The dispersion relation between $D^R(p)$ and $\rho^n(p)$ is obtained from Eq. (49) as

$$D^R(p) = -\int d\nu \frac{\rho^n(\nu, \boldsymbol{p})}{\nu - p^0 - i\varepsilon}. \tag{50}$$

Now we consider the imaginary time correlator $\mathscr{D}(\tau, \boldsymbol{x})$,

$$\mathscr{D}(\tau, \boldsymbol{x}) \equiv \langle \hat{\psi}(\tau, \boldsymbol{x}) \hat{\bar{\psi}}(0) \rangle. \tag{51}$$

The imaginary time field at arbitrary time τ and position $\boldsymbol{x}$ is measured with the time evolution operator and the translation operator,

$$\psi(\tau, \boldsymbol{x}) = \mathrm{e}^{\hat{H}\tau} \mathrm{e}^{-i\hat{\boldsymbol{p}}\cdot\boldsymbol{x}} \psi(0, \boldsymbol{x}) \mathrm{e}^{i\hat{\boldsymbol{p}}\cdot\boldsymbol{x}} \mathrm{e}^{-\hat{H}\tau}. \tag{52}$$

From Eq. (52), the imaginary time correlator can be expressed with the matrix elements of $\psi(0)$ and $\bar{\psi}(0)$ as

$$\begin{aligned}
\mathscr{D}(\tau, \boldsymbol{x}) =& \langle \hat{\psi}(\tau, \boldsymbol{x}) \hat{\bar{\psi}}(0) \rangle \\
=& \frac{1}{Z} \sum_n \mathrm{e}^{-\beta E_n} \langle n | \hat{\psi}(\tau, \boldsymbol{x}) \hat{\bar{\psi}}(0) | n \rangle \\
=& \frac{1}{Z} \sum_{m,n} \mathrm{e}^{-\beta E_n} \langle n | \hat{\psi}(\tau, \boldsymbol{x}) | m \rangle \langle m | \hat{\bar{\psi}}(0) | n \rangle \\
=& \frac{1}{Z} \sum_{m,n} \mathrm{e}^{-\beta E_n} \mathrm{e}^{\tau(E_n - E_m)} \mathrm{e}^{i(\boldsymbol{p}_m - \boldsymbol{p}_n)\cdot\boldsymbol{x}} \langle n | \hat{\psi}(0) | m \rangle \langle m | \hat{\bar{\psi}}(0) | n \rangle.
\end{aligned} \tag{53}$$

Because $i\nu_n$ is the Matsubara frequency of fermion, $\mathrm{e}^{-i\beta\nu_n} = -1$ and the Fourier transform of $\mathscr{D}(\tau, \boldsymbol{x})$

is

$$\begin{aligned}\mathscr{D}(i\nu_n,\boldsymbol{p}) =& \int_0^\beta d\tau \int d^3x \mathrm{e}^{-i(\boldsymbol{p}\cdot\boldsymbol{x}+\nu_n\tau)}\mathscr{D}(\tau,\boldsymbol{x}) \\ =& -\frac{1}{Z}\sum_{m,n}(2\pi)^3\delta^3(\boldsymbol{p}-\boldsymbol{p}_m+\boldsymbol{p}_n)\langle n|\hat{\psi}(0)|m\rangle\langle m|\hat{\bar{\psi}}(0)|n\rangle\frac{\mathrm{e}^{-\beta E_m}+\mathrm{e}^{-\beta E_n}}{E_n-E_m-i\nu_n} \\ =& -\frac{1}{Z}\sum_{m,n}(2\pi)^3\int_{-\infty}^{\infty}d\nu\,\delta(\nu-E_m+E_n)\delta^3(\boldsymbol{p}-\boldsymbol{p}_m+\boldsymbol{p}_n) \\ & \times\langle n|\hat{\psi}(0)|m\rangle\langle m|\hat{\bar{\psi}}(0)|n\rangle\frac{\mathrm{e}^{-\beta E_m}+\mathrm{e}^{-\beta E_n}}{E_m-E_n-i\nu_n}. \end{aligned} \tag{54}$$

Because the spectral density is defined as Eq. (46), the dispersion relation is obtained as

$$\mathscr{D}(i\nu_n,\boldsymbol{p}) = -\int_{-\infty}^{\infty}d\nu\frac{\rho^n(\nu,\boldsymbol{p})}{\nu-i\nu_n}. \tag{55}$$

Comparing Eqs. (50) and (55), one thus finds that

$$D^R(p) = \mathscr{D}(i\nu_n \to p^0+i\varepsilon,\boldsymbol{p}). \tag{56}$$

This result shows that the retarded Green function is connected with the Matsubara correlation function via analytic continuation of $i\nu_n \to p^0+i\varepsilon$. When one analyzes the imaginary time correlator, the corresponding real time correlator can be obtained by the analytic continuation. In the following section, we find that thermal production rates of real and virtual photons are obtained from the retarded photon self energy. Therefore, Eq. (56) is quite important to evaluate thermal emission rates.

Eq. (56) which connects the spectral function to the Green function is known as Lehmann representation.

3.2 Quark Spectral Function

In the previous subsection, we make the review on several correlators and introduce spectral functions. A quark spectral function is nothing other than the imaginary part of the quark self energy in the deconfined medium. In addition, the full photon self energy is constructed with the full quark propagator. Therefore, its structure determines the thermal photon production rate. It is useful to discuss about the nature of the spectral function. This subsection is devoted to a review of the property of the spectral function.

The quark spectral function is defined as

$$S^{ab}_{\mu\nu}(\tau,\boldsymbol{x};0,\boldsymbol{y}) = \langle \mathrm{T}_\tau\hat{\psi}^a_\mu(\tau,\boldsymbol{x})\hat{\bar{\psi}}^b_\nu(0,\boldsymbol{y})\rangle, \tag{57}$$

where the imaginary time ordering operator T_τ affects $\hat{\psi}^a_\mu(\tau_1,\boldsymbol{x})\hat{\bar{\psi}}^b_\nu(\tau_2,\boldsymbol{y})$ as

$$\mathrm{T}_\tau[\hat{\psi}(\tau_1,\boldsymbol{x})\hat{\bar{\psi}}(\tau_2,\boldsymbol{y})] = \hat{\psi}(\tau_1,\boldsymbol{x})\hat{\bar{\psi}}(\tau_2,\boldsymbol{y})\theta(\tau_1-\tau_2) - \hat{\bar{\psi}}(\tau_2,\boldsymbol{y})\hat{\psi}(\tau_1,\boldsymbol{x})\theta(\tau_2-\tau_1), \tag{58}$$

and $\psi^a_\mu(\tau,\boldsymbol{x})$ is the quark field with the Dirac index μ and the color index a. The Fourier transform of the coordinate space is defined as

$$S_{\mu\nu}(\tau,\boldsymbol{p}) = \frac{1}{VN_\mathrm{C}}\sum_a\int d^3xd^3y\mathrm{e}^{-i\boldsymbol{p}\cdot(\boldsymbol{x}-\boldsymbol{y})}S^{aa}_{\mu\nu}(\tau,\boldsymbol{x};0,\boldsymbol{y}), \tag{59}$$

where N_C is the number of color.

It is known that the quark propagator is the gauge depending correlator. In various gauge fixings, freedoms of global gauge transformation still exist. However, the trace over color indices of the quark propagator is gauge independent. In addition, photon and dilepton production rates from the deconfined medium are observables and gauge independent quantities. Therefore, it is expected that the photon self energy composed of gauge depending quark propagator and vertex is gauge independent, or the effect of gauge fixing is small at least. Based on the hypothesis, it is expected that valuating the trace over color indices of the quark propagator is enough to calculate the thermal photon production rate. In Section 4.1.1, we discuss the finite temperature quark propagator obtained on the lattice [19–21] which we use as an input. They analyze with the Landau gauge and confirm that the trace over color indices is gauge invariant and off-diagonal elements disappear.

The Fourier transform of the imaginary time space and its inverse Fourier transform are

$$S_{\mu\nu}(i\nu_n,\boldsymbol{p}) = \int_0^\beta d\tau\mathrm{e}^{i\nu_n\tau}S_{\mu\nu}(\tau,\boldsymbol{p}), \tag{60}$$

$$S_{\mu\nu}(\tau,\boldsymbol{p}) = T\sum_n\mathrm{e}^{-i\nu_n\tau}S_{\mu\nu}(i\nu_n,\boldsymbol{p}). \tag{61}$$

From the dispersion relation Eq. (55), the quark propagator (60) is expressed with the spectral function as

$$S_{\mu\nu}(i\nu_n,\boldsymbol{p}) = -\int_{-\infty}^{\infty}d\nu'\frac{\rho_{\mu\nu}(\nu',\boldsymbol{p})}{\nu'-i\nu_n}. \tag{62}$$

From Eqs. (61) and (62), one obtains the relation between $S_{\mu\nu}(\tau,\boldsymbol{p})$ and $\rho_{\mu\nu}(\nu,\boldsymbol{p})$;

$$S_{\mu\nu}(\tau,\boldsymbol{p}) = \int_{-\infty}^{\infty}d\nu\frac{\mathrm{e}^{(1/2-\tau/\beta)\beta\nu}}{\mathrm{e}^{\beta\nu/2}+\mathrm{e}^{-\beta\nu/2}}\rho_{\mu\nu}(\nu,\boldsymbol{p}). \tag{63}$$

Now let us discuss the Dirac structures of Eq. (62) [19, 21]. In the finite temperature field theory, owing to the parity symmetry and rotational symmetry, the Dirac structure of the quark spectral function can be decomposed as

$$\rho_{\mu\nu}(\nu,\boldsymbol{p})=\rho_0(\nu,p)\,(\gamma_0)_{\mu\nu}-\rho_{\rm V}(\nu,p)\,(\hat{\boldsymbol{p}}\cdot\boldsymbol{\gamma})_{\mu\nu}+\rho_{\rm S}(\nu,p)(\mathbf{1})_{\mu\nu}, \tag{64}$$

with $p=|\boldsymbol{p}|, \hat{\boldsymbol{p}}=\boldsymbol{p}/p$. Each spectral density is given by

$$\rho_0(\nu,p)=\mathrm{Tr_D}[\rho(\nu,\boldsymbol{p})\gamma_0]/4, \tag{65}$$

$$\rho_{\rm V}(\nu,p)=\mathrm{Tr_D}[\rho(\nu,\boldsymbol{p})\hat{\boldsymbol{p}}\cdot\gamma]/4, \tag{66}$$

$$\rho_{\rm S}(\nu,p)=\mathrm{Tr_D}[\rho(\nu,\boldsymbol{p})]/4. \tag{67}$$

In the following discussion, the Dirac indices are suppressed for simplicity.

Let $\mathscr{C}$ be an unitary operator for charge conjugation,

$$\mathscr{C}\psi\mathscr{C}^{-1}=C\bar{\psi}^{\rm T}, \tag{68}$$

where C is a charge conjugate matrix. The charge conjugation matrix effects $\bar{\psi}^{\rm T}$ as [84]

$$C\bar{\psi}^{\rm T}=-i\gamma_2\psi^*, \tag{69}$$

and it satisfies

$$C=-i\gamma_2\gamma_0=-C^{-1}=-C^\dagger,\ C^{-1}\gamma_\mu C=-\gamma_\mu^{\rm T}. \tag{70}$$

From Eqs. (70) and $(\mathscr{C}\psi\mathscr{C}^{-1})^\dagger=\mathscr{C}\psi^\dagger\mathscr{C}^{-1}$,

$$\mathscr{C}\bar{\psi}\mathscr{C}^{-1}=-\psi^{\rm T}C^{-1}. \tag{71}$$

For zero quark chemical potential, thermal ensembles are symmetric for the charge conjugation symmetry. It means $\langle\mathscr{C}\mathscr{O}\mathscr{C}^{-1}\rangle=\langle\mathscr{O}\rangle$. One thus obtains

$$\begin{aligned}S^{ab}_{\mu\nu}(\tau,\boldsymbol{x};0,\boldsymbol{y})&=\langle\mathscr{C}\mathrm{T}_\tau\psi^a_\mu(\tau,\boldsymbol{x})\bar{\psi}^b_\nu(0,\boldsymbol{y})\mathscr{C}^{-1}\rangle\\&=-\langle\mathrm{T}_\tau[(C\bar{\psi}^{\mathrm{T}a}(\tau,\boldsymbol{x}))_\mu(\psi^{\mathrm{T}b}(0,\boldsymbol{y})C^{-1})_\nu]\rangle\\&=-\sum_{\mu',\nu'}\langle C_{\mu\mu'}\mathrm{T}_\tau[\bar{\psi}^{\mathrm{T}a}_{\mu'}(\tau,\boldsymbol{x})\psi^{\mathrm{T}b}_{\nu'}(0,\boldsymbol{y})]C^{-1}_{\nu'\nu}\rangle\\&=\sum_{\mu',\nu'}\langle C_{\mu\mu'}\mathrm{T}_\tau[(\psi^b(0,\boldsymbol{y})\bar{\psi}^a(\tau,\boldsymbol{x}))^{\rm T}_{\mu'\nu'}]C^{-1}_{\nu'\nu}\rangle\\&=[C(S^{ba}(0,\boldsymbol{y};\tau,\boldsymbol{x}))^{\rm T}C^{-1}]_{\mu\nu},\end{aligned} \tag{72}$$

where in the 4th line I use the anticommutative nature of ψ. From Eqs. (59) and (72),

$$S_{\mu\nu}(\tau,\boldsymbol{p}) = [CS^{\mathrm{T}}(-\tau,-\boldsymbol{p})C^{-1}]_{\mu\nu} = -[CS^{\mathrm{T}}(\beta-\tau,-\boldsymbol{p})C^{-1}]_{\mu\nu}. \tag{73}$$

This result leads to

$$\rho_{\mu\nu}(\nu,\boldsymbol{p}) = [C\rho^{\mathrm{T}}(-\nu,-\boldsymbol{p})C^{-1}]_{\mu\nu}. \tag{74}$$

When the chiral symmetry is restored, the scalar term ρ_{S} proportional to $\mathbf{1}_{\mu\nu}$ vanishes because the quark propagator commutes with γ_5. In this case, the spectral density can be decomposed with the projection operator $\Lambda_{\pm}(\boldsymbol{p}) = (1 \pm \gamma_0 \hat{\boldsymbol{p}} \cdot \boldsymbol{\gamma})/2$,

$$\rho(\nu,\boldsymbol{p}) = \rho_{+}(\nu,p)\Lambda_{+}(\boldsymbol{p})\gamma_0 + \rho_{-}(\nu,p)\Lambda_{-}(\boldsymbol{p})\gamma_0, \tag{75}$$

where

$$\rho_{\pm}(\nu,p) = \frac{1}{2}\mathrm{Tr}_{\mathrm{D}}\left[\rho(\nu,\boldsymbol{p})\gamma_0\Lambda_{\pm}(\boldsymbol{p})\right] = \rho_0(\nu,p) \pm \rho_{\mathrm{v}}(\nu,p), \tag{76}$$

and Tr_{D} means the trace over the Dirac indices.

From Eq. (74), it is shown that $\rho_0(\nu,p)$ is an even function and $\rho_{\mathrm{V,S}}(\nu,p)$ are odd functions of ν;

$$\rho_0(\nu,p) = \rho_0(-\nu,p)\ \rho_{\mathrm{V}}(\nu,p) = -\rho_{\mathrm{V}}(-\nu,p),\ \rho_{\mathrm{S}}(\nu,p) = -\rho_{\mathrm{S}}(-\nu,p). \tag{77}$$

When the chiral symmetry is restored, the scalar spectral density disappears, and thus it leads to the relation between ρ_{+} and ρ_{-};

$$\rho_{\pm}(-\nu,p) = \rho_{\mp}(\nu,p). \tag{78}$$

A simple sum rule of $\rho_{\pm}$ can be obtained from the equal time anticommutation relations of ψ and $\psi^{\dagger}$ and Eq. (78). Using real time Fourier transform,

$$\begin{aligned}
\int_{-\infty}^{\infty} d\nu \rho_0(\nu,p) &= \frac{1}{4}\int_{-\infty}^{\infty} d\nu \mathrm{Tr}_{\mathrm{D}}[\rho(\nu,\boldsymbol{p})\gamma_0] \\
&= \frac{1}{4}\int_{-\infty}^{\infty} d\nu \mathrm{Tr}_{\mathrm{D}}[(\rho^{+}(\nu,\boldsymbol{p}) + \rho^{-}(\nu,\boldsymbol{p}))\gamma_0] \\
&= \frac{1}{4}\int d^4x\delta(t)\mathrm{e}^{-i\boldsymbol{p}\cdot\boldsymbol{x}}\mathrm{Tr}_{\mathrm{D}}[\langle\psi(x)\psi^{\dagger}(0)\rangle - \langle\bar{\psi}(0)\psi(x)\gamma_0\rangle] \\
&= \frac{1}{4}\int d^4x\delta(t)\mathrm{e}^{-i\boldsymbol{p}\cdot\boldsymbol{x}}[\mathrm{Tr}_{\mathrm{D}}[\langle\psi(x)\psi^{\dagger}(0)\rangle] - \sum_{\mu}[\langle(\psi(0)^{\dagger}\gamma_0)_{\mu}(\psi(x)\gamma_0)_{\mu}\rangle]] \\
&= \frac{1}{4}\int d^4x\delta(t)\mathrm{e}^{-i\boldsymbol{p}\cdot\boldsymbol{x}}\mathrm{Tr}_{\mathrm{D}}[\langle\psi(x)\psi^{\dagger}(0)\rangle + \langle\psi(0)^{\dagger}\psi(x)\rangle]
\end{aligned}$$

$$= 1. \tag{79}$$

On the other hand, from Eq. (78),

$$\begin{aligned}\int_{-\infty}^{\infty} d\nu \rho_0(\nu,p) &= \frac{1}{4}\int_{-\infty}^{\infty} d\nu \mathrm{Tr}_{\mathrm{D}}[\rho(\nu,\boldsymbol{p})\gamma_0] \\ &= \frac{1}{4}\int_{-\infty}^{\infty} d\nu \mathrm{Tr}_{\mathrm{D}}[\rho_+(\nu,p)\Lambda_+(\boldsymbol{p})+\rho_-(\nu,p)\Lambda_-(\boldsymbol{p})] \\ &= \int_{-\infty}^{\infty} d\nu \frac{1}{2}(\rho_+(\nu,p)+\rho_-(\nu,p)) \\ &= \int_{-\infty}^{\infty} d\nu \rho_+(\nu,p) \\ &= 1. \end{aligned} \tag{80}$$

Therefore,

$$\int d\nu \rho_\pm(\nu,p) = 1. \tag{81}$$

It should be emphasized that the sum rule Eq. (81) is changed due to renormalization problem [82]. However, this problem is negligible in our analysis because the lattice quark propagator obtained in Refs. [19–21] has no continuum part.

3.3 Hard Thermal Loop Approximation

Hard thermal loop (HTL) resummation technique developed by Braaten and Pisarski [58–60] is essential for perturbative analyses at $T \neq 0$. A characteristics of this method is that various physical quantities such as gluon damping rate [69, 70], quark damping rate [71, 72], photon [61–65] and dilepton production rates [67, 68] can be evaluated "gauge invariantly". The gauge invariance is important because observables are gauge independing. In addition, the quark propagator obtained on the lattice [19–21] which is used as an input to evaluate real photon production rate is inspired by the HTL quark propagator. It is useful to make a short review of the technique and the HTL perturbation theory in this section.

3.3.1 HTL Resummation

First, we consider the HTL perturbation theory in QED. Suppose a fermion propagating in a weak coupled plasma of temperature T and the coupling constant $e \ll 1$. In the following section, we define two energy scales eT and T as *soft* scale and *hard* scale, respectively. Let P be the momentum of the fermion and consider the fermion self energy perturbatively at 1-loop level. When the fermion is soft, $P \sim eT$, certain diagrams have contributions of the same order as the bare propagator. When all loop momentum is hard and all fermion momentum is soft, the loop correction becomes $\mathscr{O}(1)$. HTL

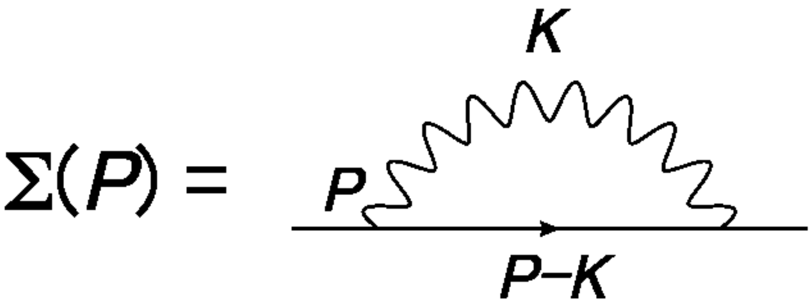

Figure 8: Diagrammatic representation of the 1-loop fermion self-energy, Eq. (83).

resummed perturbative fermion propagator is obtained from summing all such diagrams. Similarly, certain diagrams have the same order contributions as the bare soft gauge boson and HTL resummation of the boson can be also executed. The gauge boson self energy is also evaluated at 1-loop level in the HTL perturbation theory.

3.3.2 HTL fermion propagator

First, we calculate a photon self energy in QED by HTL resummation technique. The calculation is easy to extent to evaluate a quark self energy. In the hot medium, the fermion receives the thermal effect which is included in the self energy Σ. The thermal massless fermion propagator with the four momentum P is expressed as

$$S(P) = \frac{1}{\not{p} - \Sigma(P)}, \tag{82}$$

with $\not{p} = \gamma_\mu p^\mu$. From this chapter, p means the norm of three dimensional momentum $|\boldsymbol{p}|$, P and p_μ mean four momentum but $p_1 \cdot p_2$ mean the inner product of Minkowski space.

Because a photon propagator $D^{\mu\nu}(K)$ is given by $g^{\mu\nu}/K^2$ in a Feynman gauge, 1-loop fermion self energy $\Sigma(P)$ shown in Fig. (8) is obtained as

$$\Sigma(P) = -e^2 T \sum_m \int \frac{d^3k}{(2\pi)^3} \gamma_\mu S(K-P) \gamma_\nu D^{\mu\nu}(K). \tag{83}$$

When loop propagators are bare, the self energy is calculated as

$$\begin{aligned}\Sigma(P) &= -e^2 T \sum_m \int \frac{d^3k}{(2\pi)^3} \gamma_\mu \frac{1}{\not{k} - \not{p}} \gamma^\mu \frac{1}{K^2} \\ &= -e^2 T \sum_m \int \frac{d^3k}{(2\pi)^3} \gamma_\mu (\not{k} - \not{p}) \gamma^\mu \Delta(K) \widetilde{\Delta}(K-P),\end{aligned} \tag{84}$$

where $\Delta(K) = 1/K^2$ and $\widetilde{\Delta}(K-P) = 1/(K-P)^2$ with the boson Matsubara frequency k_0 and the fermion Matsubara frequency $k_0 - p_0$, respectively. When the HTL resummation is justified, it means every external fermion line is soft and loop momentum is hard, the photon momentum becomes much larger than the fermion momentum, $K \gg P$. In this case, $\not{p}$ can be negligible in Eq. (83), and thus Eq. (83) becomes

$$\begin{aligned}\Sigma(P) \simeq & -e^2 T \sum_m \int \frac{d^3k}{(2\pi)^3} \gamma_\mu \not{k} \gamma^\mu \Delta(K) \widetilde{\Delta}(P-K) \\ = & -2e^2 T \sum_m \int \frac{d^3k}{(2\pi)^3} \not{k} \Delta(K) \widetilde{\Delta}(P-K)\end{aligned} \tag{85}$$

In addition, the following approximations are applicable;

$$E_{\boldsymbol{k}-\boldsymbol{q}} = \sqrt{|\boldsymbol{k}-\boldsymbol{q}|^2} \simeq k - q\cos\theta, \tag{86}$$

$$f(E_{\boldsymbol{k}-\boldsymbol{q}}) \simeq f(k) - q\cos\theta \frac{df(k)}{dk}, \tag{87}$$

where $f(E)$ is the Fermi distribution function.

Now the Matsubara sum of the space component in Eq. (85) is evaluated to be

$$\begin{aligned}& T\sum_m \int \frac{d^3k}{(2\pi)^3} \Delta(K)\widetilde{\Delta}(P-K) k_i \\ = & \frac{1}{8\pi^2} \int \frac{k^2 dk d\Omega}{4\pi} \frac{1}{E_{\boldsymbol{k}} E_{\boldsymbol{p}-\boldsymbol{k}}} \times \\ & \Bigg[\left(1 + n\left(E_{\boldsymbol{k}}\right) - f\left(E_{\boldsymbol{p}-\boldsymbol{k}}\right)\right) \left(\frac{1}{p_0 - E_{\boldsymbol{k}} - E_{\boldsymbol{p}-\boldsymbol{k}}} - \frac{1}{p_0 + E_{\boldsymbol{k}} + E_{\boldsymbol{p}-\boldsymbol{k}}} \right) \\ & + \left(n\left(E_{\boldsymbol{k}}\right) + f\left(E_{\boldsymbol{p}-\boldsymbol{k}}\right)\right) \left(\frac{1}{p_0 + E_{\boldsymbol{k}} - E_{\boldsymbol{p}-\boldsymbol{k}}} - \frac{1}{p_0 - E_{\boldsymbol{k}} + E_{\boldsymbol{p}-\boldsymbol{k}}} \right) \Bigg] k_i .\end{aligned} \tag{88}$$

The time component is also evaluated to be

$$\begin{aligned}& T\sum_m \int \frac{d^3k}{(2\pi)^3} i\omega_n \Delta(K)\widetilde{\Delta}(P-K) \\ = & \frac{1}{8\pi^2} \int \frac{k^2 dk d\Omega}{4\pi} \frac{1}{E_{\boldsymbol{p}-\boldsymbol{k}}} \\ & \Bigg[\left(1 + n\left(E_{\boldsymbol{k}}\right) - f\left(E_{\boldsymbol{p}-\boldsymbol{k}}\right)\right) \left(\frac{1}{p_0 - E_{\boldsymbol{k}} - E_{\boldsymbol{p}-\boldsymbol{k}}} + \frac{1}{p_0 + E_{\boldsymbol{k}} + E_{\boldsymbol{p}-\boldsymbol{k}}} \right) \\ & - \left(n\left(E_{\boldsymbol{k}}\right) + f\left(E_{\boldsymbol{p}-\boldsymbol{k}}\right)\right) \left(\frac{1}{p_0 + E_{\boldsymbol{k}} - E_{\boldsymbol{p}-\boldsymbol{k}}} + \frac{1}{p_0 - E_{\boldsymbol{k}} + E_{\boldsymbol{p}-\boldsymbol{k}}} \right) \Bigg],\end{aligned} \tag{89}$$

where $n(k)$ is the Bose distribution function. Because $K \gg P$,

$$\begin{aligned} & T\sum_m \int \frac{d^3k}{(2\pi)^3}\Delta(K)\widetilde{\Delta}(P-K)k_i \\ \simeq & \frac{1}{8\pi^2}\int \frac{\mathrm{d}k\mathrm{d}\Omega}{4\pi}\left[(1+n(E_{\boldsymbol{k}})-f(E_{\boldsymbol{k}}))\frac{-1}{2}+(n(E_{\boldsymbol{k}})+f(E_{\boldsymbol{k}}))\left(\frac{1}{p\cdot\hat{K}}-\frac{1}{p\cdot\hat{K}'}\right)k\right]\hat{k}_i, \end{aligned} \tag{90}$$

with $\hat{K}=(1,\hat{\boldsymbol{k}})$, $\hat{K}'=(1,-\hat{\boldsymbol{k}})$. Except for the vacuum divergence term, the second term is the leading term of order T^2 in Eq. (90). In addition, the radial integral of thermal distribution functions are approximated as

$$\int_0^\infty dk k n(k) = 2\int_0^\infty dk k f(k) = \frac{\pi^2T^2}{6}. \tag{91}$$

Now Eq. (88) becomes

$$\frac{T^2}{16}\int \frac{d\Omega}{4\pi}\frac{\hat{k}_i}{p\cdot\hat{K}}. \tag{92}$$

The angular integral is performed as

$$\begin{aligned} \frac{T^2}{16}\int \frac{d\Omega}{4\pi}\frac{\hat{k}_i}{p\cdot\hat{K}} =& \int \frac{d\Omega}{4\pi}\frac{\cos\theta}{p\cdot\hat{K}} = \frac{1}{2}\int_{-1}^{1} dt \frac{t}{p_0+pt} \\ =&\frac{1}{2}\left(\frac{2}{p}-\frac{p_0}{p^2}\ln(p_0+pt)\Big|_{-1}^{1}\right) = \frac{1}{p}\left(1-\frac{p_0}{2p}\ln\left(\frac{p_0+p}{p_0-p}\right)\right) \\ =&\frac{1}{p}Q_1\left(\frac{p_0}{p}\right), \end{aligned} \tag{93}$$

where $Q_0(x)$ and $Q_1(x)$ are the second kind Legendre functions;

$$Q_0(x) = \frac{1}{2}\ln\frac{x+1}{x-1},\ Q_1(x) = xQ_0(x)-1. \tag{94}$$

The fermion self energy is calculated as

$$\Sigma(P) = \frac{m_{\mathrm{T}}^2}{p}\gamma_0 Q_0\left(\frac{p_0}{p}\right) + \frac{m_{\mathrm{T}}^2}{p}\hat{\boldsymbol{p}}\cdot\boldsymbol{\gamma}\left(1-\frac{p_0}{p}Q_0\left(\frac{p_0}{p}\right)\right), \tag{95}$$

where $m_{\mathrm{T}} = eT/\sqrt{8}$ is the fermion thermal mass.

$Q_0(x)$ has a branch cut in $-1<x<1$ on the real axis. Just above the real axis, with an infinitesimal $\eta>0$,

$$\begin{aligned} Q_0(x+i\eta) =& \frac{1}{2}\ln\frac{x+1+i\eta}{x-1+i\eta} \\ =& \frac{1}{2}\ln\left|\frac{x+1}{x-1}\right| - \frac{i\pi}{2}\theta(1-x^2), \end{aligned} \tag{96}$$

and below the cut, with $\eta > 0$,

$$Q_0(x-i\eta) = \frac{1}{2}\ln\left|\frac{x+1}{x-1}\right| + \frac{i\pi}{2}\theta(1-x^2). \tag{97}$$

The imaginary part of the HTL retarded photon self energy is arisen from Eqs. (96) and (97). It is obtained by analytic continuation $p_0 = i\nu_n \to \nu + i\eta$,

$$\mathrm{Im}\Sigma^R(P) = -\frac{\pi}{2}\frac{m_{\mathrm{T}}^2}{p}\left(\gamma_0 - \frac{\nu}{p}\hat{\boldsymbol{p}}\cdot\gamma\right). \tag{98}$$

3.3.3 HTL Fermion Spectral Function

One can extract the HTL fermion spectral function from the obtained fermion self energy Eq. (95). The HTL fermion propagator is decomposed with the projection operator as

$$S(P) == \Delta_+(p)\Lambda_+\gamma_0 + \Delta_-(p)\Lambda_-\gamma_0. \tag{99}$$

$\Delta_\pm = \mathrm{Tr_D}[S(P)\gamma_0\Lambda_\pm]/2$ is expressed as

$$\Delta_\pm(p) = \left(p_0 \mp p - \frac{m_{\mathrm{T}}^2}{2p}\left[\left(1 \mp \frac{p_0}{p}\ln\frac{p_0+p}{p_0-p} \pm 2\right)\right]\right)^{-1} \tag{100}$$

The spectral function is obtained from the imaginary part of $\Delta_\pm$;

$$\begin{aligned}\rho_\pm(p_0,\boldsymbol{p}) =& -\frac{1}{\pi}\mathrm{Im}\Delta_\pm(p_0,\boldsymbol{p})\\ =& Z_\pm(p)\delta(p_0-\omega_\pm(\boldsymbol{p})) + Z_\mp(p)\delta(p_0+\omega_\mp(\boldsymbol{p}))\\ &+\frac{1}{2p}m_{\mathrm{T}}^2(1\mp x)\,\theta(1-x^2)\times\\ &\left[\left(p(1\mp x) \pm \frac{m_{\mathrm{T}}^2}{2p}\left[(1\mp x)\ln\left|\frac{x+1}{x-1}\right| \pm 2\right]\right)^2 + \frac{\pi^2 m_T^4}{4p^2}(1\mp x)^2\right]^{-1},\end{aligned} \tag{101}$$

where $x = p_0/p$. The spectral function is composed of two poles at $p_0 = \pm\omega_\pm$ or $p_0 = \pm\omega_\mp$ and a continuum part in the space-like region, $-p < p_0 < p$. The continuum part arises from the branch cut of the second kind Legendre function. Dispersions $\omega_\pm \geq 0$ are the solution of equation $\Delta_\pm^{-1} = 0$. Two solutions of $\Delta_+ = 0$ are

$$(p_0,\boldsymbol{p}) = (\omega_+(p),\boldsymbol{p}) \text{ or } (-\omega_-(p),\boldsymbol{p}), \tag{102}$$

and two solutions of $\Delta_- = 0$ are

$$(p_0, \boldsymbol{p}) = (-\omega_+(p), \boldsymbol{p}) \text{ or } (\omega_-(p), \boldsymbol{p}). \tag{103}$$

Two residues $Z_\pm$ in Eq. (101) are evaluated as

$$\begin{aligned} Z_\pm(p) = &\left[\left. \frac{\partial \Delta_\pm^{-1}(p_0, p)}{\partial p_0} \right|_{p_0=\omega_\pm} \right]^{-1} = 1 - \left. \frac{\partial \Sigma_\pm(P)}{\partial p_0} \right|_{p_0=\omega_\pm} \\ = &\frac{\omega_\pm^2(p) - p^2}{2m_\mathrm{T}^2}. \end{aligned} \tag{104}$$

The two particle-like excited states $\omega_\pm$ are known as *quasi-particle* states. The excited state with dispersion $\omega_+(p)$ is called *normal* mode and another state with dispersion $\omega_-(p)$ is called *plasmino* mode. In Fig. 9, the quasi-particle dispersions are illustrated. Two quasi-particle states acquire thermal mass m_T although the bare fermion is massless. Plasmino dispersion has a peculiar behavior, it has a minimum at non-zero momentum. It should also be mentioned that plasmino mode disappears in high momentum limit because the plasmino dispersion approaches to the light cone as shown in Fig. 9. Similarly, the normal mode approaches to the light cone in high momentum region. The asymptote is weaker than the plasmino one, the normal dispersion approaches as $p + m_\mathrm{T}^2/p$ and the plasmino dispersion approaches as $p + 2p\exp^{-2p^2/m_\mathrm{T}^2}/e$. Summarize the quasi-particle characteristics, when the quasi-particle has the higher momentum to the temperature of the system T, the effect of thermal scattering on the quasi-particle becomes smaller. It means that the medium effect on the fermion becomes smaller, and thus the plasmino mode disappears and the normal mode behaves as the bare fermion.

At the end of this subsection, we briefly discuss on the fermion self energy obtained by the HTL resummation technique in QCD at high temperature. Going from QED to QCD is simple. The self energy is only modified by a SU(3) group factor of fundamental representation $C_F = 4/3$. The square of the thermal mass is replaced as

$$m_\mathrm{T}'^2 = g^2 T^2 C_F / 8. \tag{105}$$

3.3.4 HTL Gauge Boson Propagator

This subsection is devoted to the analysis of gauge boson self energy in HTL approximation. As in the similar manner for the case of fermion, we first discuss QED boson and then evaluate gluon self energy in QCD.

When the external photon momentum is soft and the loop fermion momentum is hard, the one

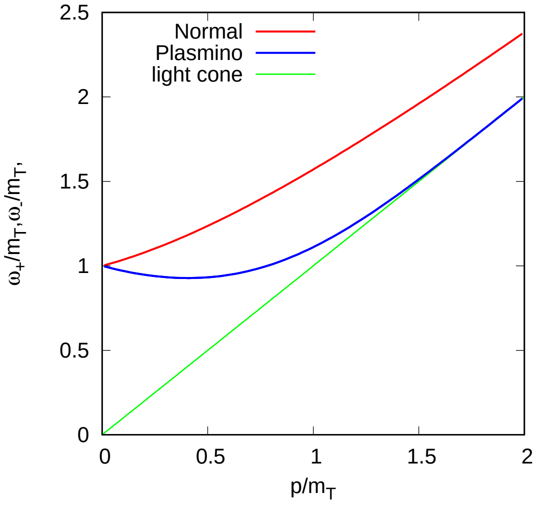

Figure 9: The dispersions of two quasi-particle states. The green line is light cone.

loop photon self energy $\Pi_{\mu\nu}(Q)$ shown in Fig. 10 is given by

$$\begin{aligned}\Pi_{\mu\nu}(Q) &= -e^2 T \sum_n \int \frac{d^3p}{(2\pi)^3} \mathrm{Tr}\left[\gamma_\mu S(P) \gamma_\nu S(P-Q)\right] \\ &= -e^2 T \sum_n \int \frac{d^3p}{(2\pi)^3} \mathrm{Tr}\left[\gamma_\mu \not{p} \gamma_\nu (\not{p} - \not{q})\right] \widetilde{\Delta}(P) \widetilde{\Delta}(P-Q). \end{aligned} \tag{106}$$

It is approximated as

$$\begin{aligned}\Pi_{\mu\nu}(Q) &\simeq -e^2 T \sum_n \int \frac{d^3p}{(2\pi)^3} (8 p_\mu p_\nu - 4P^2 g_{\mu\nu}) \widetilde{\Delta}(P) \widetilde{\Delta}(P-Q) \\ &\simeq -2 m_{T,\gamma}^2 \int \frac{d\Omega}{4\pi} \left(g_{\mu 0} g_{\nu 0} - \frac{i\omega_m \hat{P}_\mu \hat{P}_\nu}{q \cdot \hat{P}} \right), \end{aligned} \tag{107}$$

where $m_{\mathrm{T},\gamma}^2 = e^2 T^2/6$ is the photon thermal mass. In the first line we ignore $\not{q}$ and the loop integral is estimated with the HTL perturbation technique.

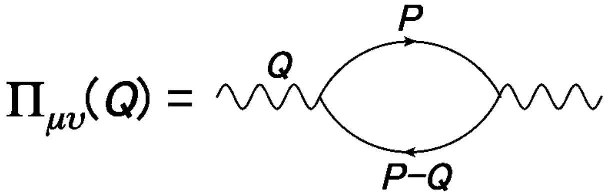

Figure 10: Diagrammatic representation of the photon self-energy, Eq. (107).

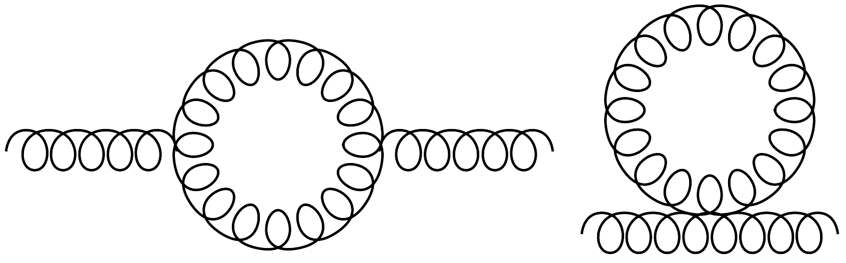

(a) Gluon loop 1 (b) Gluon loop 2

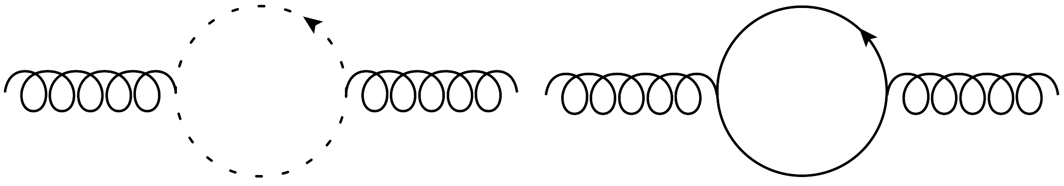

(c) ghost loop (d) quark loop

Figure 11: Four diagrammatic representation of one loop gluon self energies.

It is also possible to estimate the HTL gluon self energy with the analogy of QED. The one loop gluon self energy is calculated with four diagrams shown in Fig. 11. It is composed of two gluon loops, one ghost loop and one quark loop.

The contribution from the gluon loop shown in Fig. 11(a) is evaluated as

$$\Pi^{(a)}_{\mu\nu}(Q) = g^2 C_A T \sum_{m'} \int \frac{d^3k}{(2\pi)^3} (5k_\mu k_\nu + K^2 g_{\mu\nu}) \Delta(K) \Delta(Q-K), \tag{108}$$

where C_A is a SU(3) group factor of the adjoint representation. Another contribution from the gluon loop shown in Fig. 11(b) is given by

$$\Pi^{(b)}_{\mu\nu}(Q) = -3g^2 C_A g_{\mu\nu} T \sum_{m'} \int \frac{d^3k}{(2\pi)^3} \Delta(K). \tag{109}$$

The ghost loop contributes as

$$\Pi^{(c)}_{\mu\nu}(Q) = -3g^2 C_A T \sum_{m'} \int \frac{d^3k}{(2\pi)^3} k_\mu k_\nu \Delta(K) \Delta(Q-K). \tag{110}$$

Adding the gluon and ghost loops, one obtains

$$\Pi^{(a+b+c)}_{\mu\nu}(Q) = g^2 C_A T \sum_{m'} \int \frac{d^3k}{(2\pi)^3} (4k_\mu k_\nu - 2K^2 g_{\mu\nu}) \Delta(K) \Delta(Q-K). \tag{111}$$

The last contribution from the quark loop is obtained from multiplying the number of flavor N_f on the

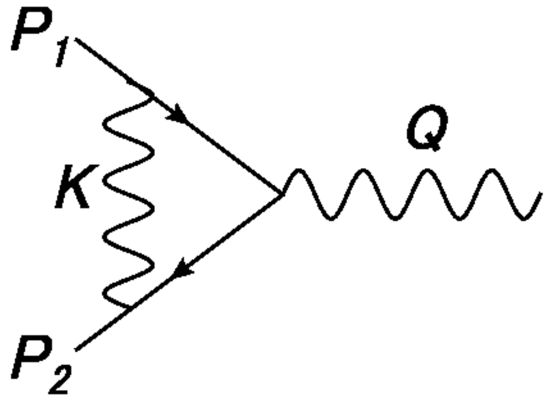

Figure 12: The gauge invariant QED vertex correction in hard thermal loop resummed perturbation theory.

QED self energy, Eq. (107);

$$\Pi^{(d)}_{\mu\nu}(Q) = -g^2 N_f T \sum_n \int \frac{d^3p}{(2\pi)^3}(8p_\mu p_\nu - 4P^2 g_{\mu\nu})\widetilde{\Delta}(P)\widetilde{\Delta}(Q-P). \tag{112}$$

Integrals of Fermi and Bose distribution functions are related with each other as

$$\int_0^\infty dp p f(p) = \frac{1}{2}\int_0^\infty dk k n(k). \tag{113}$$

Therefore, the Matsubara sum of bosonic frequency can be translated to the sum on fermionic frequency as

$$T\sum_{m'} \int \frac{d^3k}{(2\pi)^3}\Delta(K) = -2T\sum_n \int \frac{d^3p}{(2\pi)^3}\widetilde{\Delta}(P), \tag{114}$$

$$T\sum_{m'} \int \frac{d^3k}{(2\pi)^3}\Delta(K)\Delta(Q-K) = -2T\sum_n \int \frac{d^3p}{(2\pi)^3}\widetilde{\Delta}(P)\widetilde{\Delta}(Q-P). \tag{115}$$

As a result, the SU(3) gauge boson self energy can be obtained only by a simple replacement of the thermal mass;

$$m'^2_{\mathrm{T},gluon} = \frac{1}{6}g^2T^2(C_A + N_f). \tag{116}$$

3.3.5 HTL vertex correction

The HTL vertex correction is needed to estimate the leading order dilepton production rate perturbatively. This subsection is devoted to estimate the one loop QED vertex correction.

When all the external lines are soft and each internal line is hard, the one loop vertex shown in

Fig. 12 is the only contributable vertex correction. It is estimated as

$$\begin{aligned} e\delta\Gamma_\mu(P_1,P_2) \simeq & e^3 T\sum_n \int \frac{d^3k}{(2\pi)^3}[\gamma_\nu \not{k}\gamma_\mu \not{k}\gamma^\nu]\Delta(K)\widetilde{\Delta}(P_2-K)\widetilde{\Delta}(P_1-K) \\ = & e^3 T\sum_n \int \frac{d^3k}{(2\pi)^3}\gamma_\nu[2k_\mu \not{k} - \gamma_\mu K^2]\gamma^\nu \Delta(K)\widetilde{\Delta}(P_2-K)\widetilde{\Delta}(P_1-K). \end{aligned} \tag{117}$$

The first term and the second term in Eq. (117) are of order T^2 and $\ln T$, respectively. Therefore, the second term is negligible in high temperature limit and the vertex in this limit is calculated to be

$$\delta\Gamma_\mu(P_1,P_2) = m_T^2 \int \frac{d\Omega}{4\pi}\frac{\hat{K}_\mu \hat{\not{K}}}{\left(p_1\cdot\hat{K}\right)\left(p_2\cdot\hat{K}\right)}, \tag{118}$$

where m_T is the fermion thermal mass. From Eq. (95), it is easily verified that Eq. (118) satisfies the Ward-Takahashi identity;

$$(p_1-p_2)^\mu\, \delta\Gamma_\mu(P_1,P_2) = \Sigma(P_1) - \Sigma(P_2). \tag{119}$$

This is an important signature of the HTL resummed perturbation theory. Owing to Eq. (119), various quantities can be evaluated gauge invariantly with the HTL perturbation theory.

3.4 Photon and Dilepton Production Rates

In this section, we first introduce the formula of photon and dilepton production rates from the static hot medium. Then perturbative analyses of the rates of electromagnetic probes are overviewed.

3.4.1 Thermal Production Rates from Static Hot Medium

In this paper, we are interested in the thermal photon and dilepton production rates per unit time and unit volume from the static medium. We make a review on these quantities in the following section.

Consider an initial state $|i\rangle$ and a final state $|f\rangle$ and a transition between them which emits or absorbs a real photon or a virtual photon. The virtual photon is off-shell state, and thus it becomes a lepton and anti-lepton pair in the final state. We define the photon momentum $q_\mu = (\omega, \boldsymbol{q})$ and the polarization vector ε_μ. The transition rate between the two states is

$$R_{fi} = \frac{|S_{fi}|^2}{tV}, \tag{120}$$

where tV is the space-time volume where the interaction takes place and S_{fi} is the S-matrix element.

To leading order in the electromagnetic interaction, the matrix element is given by

$$S_{fi} = \langle f| \int d^4x j_\mu(X) A^\mu(X) |i\rangle, \tag{121}$$

where $j_\mu(X) = e\bar{\psi}(X)\gamma_\mu\psi(X)$ is the electromagnetic current. The free vector field is considered;

$$A^\mu(X) = \frac{\varepsilon^\mu}{\sqrt{2\omega V}}(\mathrm{e}^{iq\cdot x} + \mathrm{e}^{-iq\cdot x}), \tag{122}$$

with the polarization tensor ε_μ. Suppose $|f,i\rangle$ is the eigenstate of the momentum operator and considering the translational invariance for the matrix element,

$$\langle f|j_\mu(X)|i\rangle = \mathrm{e}^{i(p_f - p_i)\cdot x}\langle f|j_\mu(0)|i\rangle. \tag{123}$$

Substitute Eqs. (121), (122) and (123) for Eq. (120), the transition rate Eq. (120) is evaluated as

$$R_{fi} = \frac{\varepsilon^{*\mu}\varepsilon^\nu}{2\omega V}(2\pi)^4[\delta^4(P_i - P_f + Q) + \delta^4(P_i - P_f - Q)]\langle f|j_\mu(0)|i\rangle\langle i|j_\nu(0)|f\rangle. \tag{124}$$

From Eq. (124), keeping the emission part of δ-function, integrating over final states, summing over polarization indices and averaging over initial states with the Boltzmann weight $\mathrm{e}^{-\beta\hat{H}}/Z$, where Z is the partition function and $\hat{H}$ is the Hamiltonian of the system, one obtains the thermal rate dR from the medium

$$dR = \sum_\varepsilon \frac{\varepsilon^{*\mu}\varepsilon^\nu}{2\omega V}\frac{Vd^3q}{(2\pi)^3}\frac{1}{Z}\sum_i \mathrm{e}^{-\beta\hat{H}}\sum_f (2\pi)^4\delta^4(P_i - P_f - Q)\langle f|j_\mu(0)|i\rangle\langle i|j_\nu(0)|f\rangle. \tag{125}$$

From $dR = dN^\gamma/d^4x$ and the sum over polarization tensors gives the metric, one obtains the differential real photon production rate per unit time per unit volume as

$$\omega\frac{dN^\gamma}{d^3qd^4x} = -\frac{g^{\mu\nu}}{2}\frac{1}{(2\pi)^3}\frac{1}{Z}\sum_i \mathrm{e}^{-\beta\hat{H}}\sum_f (2\pi)^4\delta^4(P_i - P_f - Q)\langle f|j_\mu(0)|i\rangle\langle i|j_\nu(0)|f\rangle. \tag{126}$$

As discussed in Section 3.1.3, spectral functions are related to the absorption and emission processes. From Eqs. (46) and (126) and taking into account the fact that the spectral density is proportional to the imaginary part of the retarded photon self energy $\pi\rho^n_{\mu\nu}(Q) = -\mathrm{Im}\Pi^R_{\mu\nu}(Q)$, the thermal real photon production rate per unit time per unit volume is expressed as

$$\omega\frac{dN^\gamma}{d^3qd^4x} = -\frac{1}{(2\pi)^3}\frac{1}{\mathrm{e}^{\beta\omega} - 1}\mathrm{Im}\Pi^{R,\mu}_\mu(Q). \tag{127}$$

This formula is valid to order e^2 and to all orders in g. In addition, Eq. (127) is valid both in confined and deconfined phases.

The thermal dilepton production rate is also derived in the similar manner. In this case, the final state includes the lepton and anti-lepton pair, and thus the S-matrix element between two states is expressed as

$$S_{fi} = \frac{e}{Q^2}\bar{u}(\boldsymbol{p}_1)\gamma^{\mu}v(\boldsymbol{p}_2)\langle f|\int d^4x j_{\mu}(X)|i\rangle, \tag{128}$$

where $\boldsymbol{p}_1$ and $\boldsymbol{p}_2$ are three dimensional momenta of leptons and $\bar{u}$ and v are the Dirac spinors of leptons, respectively. Substitute Eq. (128) for Eq. (120), keep the emission part, summing over final states and lepton spins, and averaging over initial states with the Boltzmann weight, one obtains

$$dR = \frac{e^4}{Q^4}\sum_{\text{spins}}(\bar{u}(\boldsymbol{p}_1)\gamma^{\mu}v(\boldsymbol{p}_2))(\bar{u}(\boldsymbol{p}_1)\gamma^{\nu}v(\boldsymbol{p}_2))^*\frac{1}{e^{\beta\omega}-1}\mathrm{Im}\Pi^R_{\mu\nu}(Q)\frac{d^3p_1}{2p_1^0(2\pi)^3}\frac{d^3p_2}{2p_2^0(2\pi)^3}. \tag{129}$$

The sum over spins are evaluated as

$$\sum_{\text{spins}}(\bar{u}(\boldsymbol{p}_1)\gamma^{\mu}v(\boldsymbol{p}_2))(\bar{u}(\boldsymbol{p}_1)\gamma^{\nu}v(\boldsymbol{p}_2))^* = 4[p_1^{\mu}p_2^{\nu}+p_2^{\mu}p_1^{\nu}-g^{\mu\nu}(p_1\cdot p_2+m_l^2)], \tag{130}$$

with the lepton mass m_l. The thermal dilepton production rate R per unit time and unit volume is expressed as

$$R = e^2\int\frac{d^4q}{(2\pi)^4}\frac{1}{Q^4}\frac{1}{e^{\beta\omega}-1}\mathrm{Im}\Pi(Q)^R_{\mu\nu}(Q)L^{\mu\nu}(Q), \tag{131}$$

where the tensor $L^{\mu\nu}$ is arisen from the spin sum,

$$\begin{aligned}L^{\mu\nu}(Q) =& \int\frac{d^3p_1}{2p_1^0(2\pi)^3}\frac{d^3p_2}{2p_2^0(2\pi)^3}(2\pi)^4\delta^4(Q-P_1-P_2)4[p_1^{\mu}p_2^{\nu}+p_2^{\mu}p_1^{\nu}-g^{\mu\nu}(p_1\cdot p_2+m_l^2)]\\ =&\frac{1}{6\pi}(q^{\mu}q^{\nu}-Q^2g^{\mu\nu}).\end{aligned} \tag{132}$$

The differential production rate $dR = dN^{l^+l^-}/d^4x$ is evaluated as

$$\frac{dN^{l^+l^-}}{d\omega d^3q d^4x} = -\frac{\alpha}{12\pi^4}\frac{1}{Q^2}\frac{1}{e^{\beta\omega}-1}\mathrm{Im}\Pi^{R,\mu}_{\mu}(Q), \tag{133}$$

where α is the fine structure constant $e^2/4\pi$.

From Eqs. (127) and (133), one finds that thermal photon and dilepton production rates are obtained from the imaginary part of the photon self energy. The difference between coefficients arises from the difference of final states.

3.4.2 Perturbative Photon Production Rate:Log Part

In this and next sections, the perturbative analysis of thermal photon production rate is reviewed. Since the thermal photon is proposed as the direct signal of the QGP plasma [6, 53–57], a plenty of investigation is carried out in these decades. It was a difficult analysis owing to an infra red divergence, but, first, the gauge invariant leading order contribution of the strong coupling constant g was estimated by Kapusta *et al.* [61] and Baier *et al.* [62] independently. The HTL resummation technique plays a significant role in Refs. [61, 62] to remove the infrared divergence and estimate production rate gauge invariantly. After the leading order production rate is evaluated, the importance of the *Landau-Pomeranchuk-Migdal* (LPM) effect [74–77] is recognized even in the leading order analysis. Arnold, Moore and Yaffe considered the LPM effect and analyzed the complete leading order results of thermal photons [63,64]. Owing to the LPM effect, some ladder type diagrams which seems to be higher order diagrams contribute to the same order as g^2. The next-to-leading order photon production rate was evaluated by Ghiglieri *et al.* [65] in quite recently. In this study, detailed and careful analysis on higher order corrections is performed.

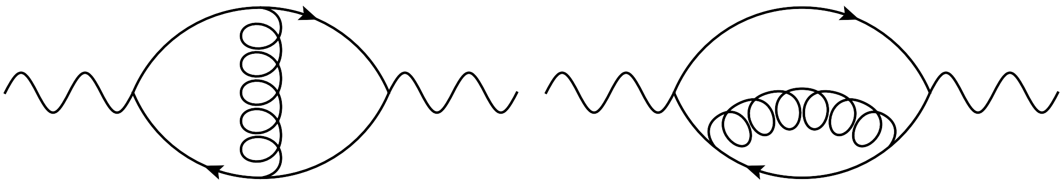
(a) Gluon exchange (b) Gluon dress

Figure 13: The lowest order 2-loop diagrams contribute to the hard photon production.

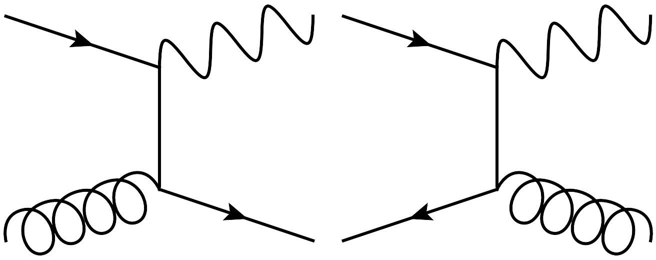
(a) Compton scattering (b) Pair annihilation

Figure 14: 2 to 2 photon emission reactions.

Now let us discuss the first analyzed leading order result. When the emitted photon has the enough high momentum so that the thermal medium effect can be ignored, one can evaluate the photon self energy constructed with bare propagators and vertices. The lowest order diagrams having nonzero contribution to the photon production rate are two-loop diagrams shown in Fig. 13 because the photon emission from one-loop diagram is forbidden kinematically. Cut of these diagrams corresponds to

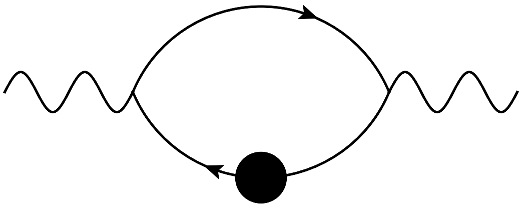

Figure 15: The lowest order diagram contributes to the soft photon emission. The black circle means that the propagator is HTL fermion and other propagator and vertices are bare.

inelastic pair annihilation process $q\bar{q} \to g\gamma$ and Compton scattering process $qg \to q\gamma$. These photon emission processes shown in Fig. 14 are known as 2 to 2 processes. In a low momentum region, two-loop diagrams have infrared divergence. To avoid this divergence, the photon self energy is estimated with the HTL resummed propagator which has the effective thermal mass in Refs. [61,62]. It is shown that the one-loop diagram constructed with one HTL quark, one bare quark and bare vertices shown in Fig. 15 has the leading order contribution.

In Refs. [61, 62], they introduce a cutoff μ_{LO} to separate soft and hard scales. The self energy is estimated as bare two-loop diagrams in the hard momentum region. On the other hand, the photon self energy is calculated with the HTL resummation technique in the soft momentum region. Surprisingly, the final result does not depend on the cutoff μ_{LO} [61, 62].

In two flavor massless QCD and taking $\mu_{\mathrm{LO}}^2 \to 0$ limit, each rate is evaluated as

$$\omega\frac{dN^{\gamma}_{\text{annihilation}}}{d^3q d^4x} = \frac{5}{9}\frac{\alpha\alpha_s}{12\pi^2}T^2 \mathrm{e}^{-\beta\omega}[\ln(4\omega T/\mu_{\mathrm{LO}}^2) + D_1], \tag{134}$$

$$\omega\frac{dN^{\gamma}_{\text{Compton}}}{d^3q d^4x} = \frac{5}{9}\frac{\alpha\alpha_s}{6\pi^2}T^2 \mathrm{e}^{-\beta\omega}[\ln(4\omega T/\mu_{\mathrm{LO}}^2) + D_2], \tag{135}$$

where $D_{1,2}$ are constants and $\alpha_s = g^2/4\pi$.

Next we consider the soft photon production rate. The HTL quark propagator obtained in Section 3.3.2 includes $\mathcal{O}(g^2)$ correction. Therefore the one-loop diagram shown in Fig. 15 gives the leading order rate of α_s. It should be mentioned that a diagram constructed by two HTL propagators gives higher order contribution in this kinematical region. The diagram constructed by the HTL propagator and HTL vertex also becomes higher order diagram. In soft region the two-loop diagram shown in Fig. 13(a) is not considered but it is adopted when the ladder type diagram is calculated in *collinear* region which we discuss in the next section.

The photon self energy in two flavor QCD with the HTL quark propagator is

$$\Pi_{\mu\nu}(Q) = -\frac{5}{3}e^2 T\sum_n \int \frac{d^3p}{(2\pi)^3}\mathrm{Tr}_{\mathrm{D}}[S^{\mathrm{HTL}}(P)\gamma_\mu S(P+Q)\gamma_\nu]. \tag{136}$$

Now only the soft quark loop is focused. Therefore, the integral region is limited by $0 \le P^2 \le \mu_{\mathrm{LO}}^2$.

The soft photon production rate is valuated as

$$\omega\frac{dN^{\gamma}_{\text{soft}}}{d^3qd^4x}=\frac{5}{9}\frac{\alpha\alpha_s}{4\pi^2}T^2\mathrm{e}^{-\beta\omega}\ln\frac{\mu^2_{\text{LO}}}{g^2T^2/3}. \tag{137}$$

Adding Eqs. (135) and (137), the leading log perturbative photon production rate is obtained;

$$\omega\frac{dN^{\gamma}_{\text{soft+hard}}}{d^3qd^4x}=\frac{5}{9}\frac{\alpha\alpha_s}{4\pi^2}T^2\mathrm{e}^{-\beta\omega}\ln\frac{2.912\beta\omega}{g^2}. \tag{138}$$

The cutoff dependence disappears.

3.4.3 Perturbative Photon Production Rate:Complete Leading Order Result

It was found that leading order analyses in Refs. [61, 62] was not enough and Arnold, Moore and Yaffe evaluated the complete leading order result [63, 64]. Next, we consider the gluon multi-scattering effect and derive the complete leading order result of thermal photon production.

It is found that other kinematical regions have the leading order contribution. When the hard quark emits the photon which is almost parallel to the quark, some gluon scattering reactions shown in Fig. 16 have the leading order contributions. This kinematical region is famous as *collinear* region. The gluon scattering processes shown in Fig. 16 seem to be higher order contributions. However, the single gluon scatterings shown in Figs. 16(a) and 16(b) have $\mathscr{O}(1)$ correction when the gluon is soft. Moreover, the multi gluon scatterings shown in Figs. 16(c) and 16(d) give $\mathscr{O}(1)$ corrections as well as the single gluon scatterings. In these cases, intermediate quarks are almost on-shell, energies differ from on-shell quarks by only $\mathscr{O}(g^2T)$. Their Fourier transform gives long lifetime of quarks of $\mathscr{O}(1/g^2T)$. The scale $\mathscr{O}(1/g^2T)$ is also known as the photon formation time because all intermediate quark has the $\mathscr{O}(1/g^2T)$ lifetime, and thus the photon emission process also acquire the same duration. Now each gluon is soft, its energy is of order gT. It means that the gluon scattering time is estimated as $\mathscr{O}(1/gT)$ and the time is shorter than the photon formation time. Therefore, the interference of each multi-scattering processes has occurred [63, 66] and it makes $\mathscr{O}(1)$ suppression on the production rate. This suppression is known as the LPM effect [74–77], the contribution from multi-scattering diagrams is calculated in Refs. [63, 64, 66].

It is known that the ladder type diagrams in Fig. 17 have the leading order contributions owing to the LPM effect. In Fig. 17, each quark is hard but photons and gluons are soft. Therefore, gluon propagators are resummed by the Braaten and Pisarski's HTL method. The contribution of ladder type diagrams is estimated by an analogy of the Bethe-Salpeter equation. The differential photon

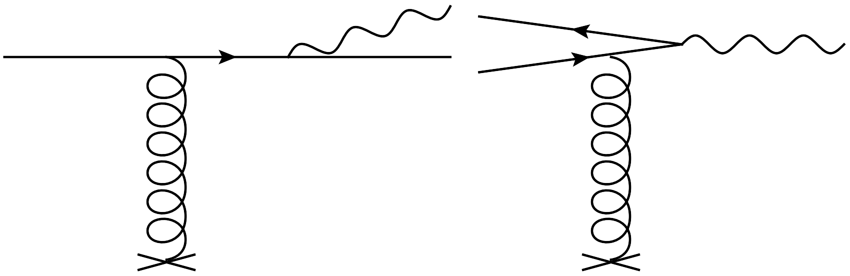

(a) Compton scattering with single gluon scattering

(b) Pair annihilation with single gluon scattering

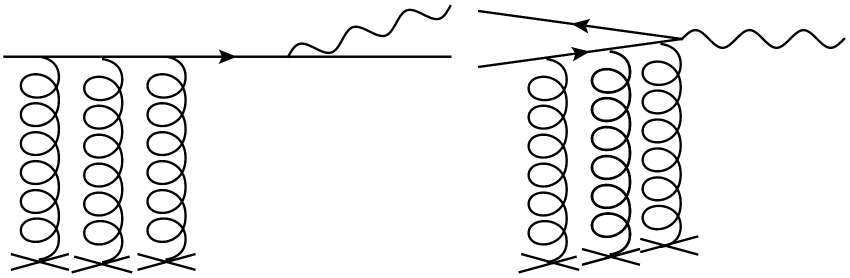

(c) Compton scattering with multi gluon scatterings

(d) Pair annihilation with multi gluon scatterings

Figure 16: *Collinear* photon emissions.

emission rate of two flavor QCD obtained from ladder diagrams is

$$\omega\frac{dN^{\gamma}_{\mathrm{AMY}}}{d^3qd^4x}=\frac{5T^2\alpha\alpha_s f(q)}{18\pi^2}\int_{-\infty}^{\infty}dp_{||}\frac{p_{||}^2+(p_{||}+q)^2}{4p_{||}^2(p_{||}+q)^2}\frac{3f(p_{||}+q)[1-f(p_{||})]}{g^2T^2f(q)}\int\frac{d^2p_{\perp}}{(2\pi)^2}\mathrm{Re}[2\boldsymbol{p}_{\perp}\cdot\boldsymbol{F}(\boldsymbol{p},q)],\tag{139}$$

where $\boldsymbol{p}_{||}$ and $\boldsymbol{p}_{\perp}$ are quark momenta parallel or perpendicular to $\boldsymbol{q}$, respectively.

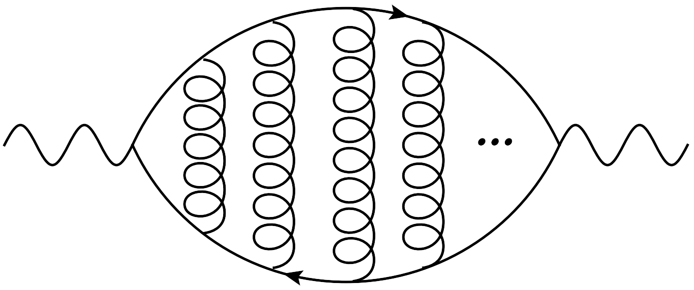

Figure 17: The ladder type diagram contributes to the leading order photon emission. Photons and vertices are bare but gluons are HTL ones. Hard quarks are almost on-shell.

The unknown function $\boldsymbol{F}$ has a relation with $\boldsymbol{p}_\perp$ of

$$2\boldsymbol{p}_\perp = i\delta E(\boldsymbol{p},q)\boldsymbol{F}(\boldsymbol{p},q)+\int\frac{d^2q_\perp}{(2\pi)^2}\mathscr{C}(\boldsymbol{q}_\perp)[\boldsymbol{F}(\boldsymbol{p},q)-\boldsymbol{F}(\boldsymbol{p}+\boldsymbol{q}_\perp,q)], \tag{140}$$

where δE is

$$\delta E(\boldsymbol{p},q) = \frac{q}{2p_{||}(p_{||}+q)}\left(p_\perp^2+\frac{g^2T^2}{3}\right), \tag{141}$$

and the collision term $\mathscr{C}$ is

$$\mathscr{C}(\boldsymbol{q}_\perp) = \frac{g^2m_\mathrm{D}^2}{3}\int d\omega dq_{||}\delta(\omega-q_{||})\frac{T}{q}\left[\frac{2}{|q^2-\Pi^\mathrm{L}_\mathrm{AMY}(Q)|^2}+\frac{[1-(\omega/q)^2]^2}{|Q^2-\Pi^\mathrm{T}_\mathrm{AMY}(Q)|^2}\right], \tag{142}$$

where $m_\mathrm{D} = 5e^2g^2T^2/9$ is the Debye mass and $\Pi^\mathrm{L}_\mathrm{AMY}$ and $\Pi^\mathrm{T}_\mathrm{AMY}$ are longitudinal and transverse components of the photon self energy, respectively.

One can obtain the complete leading log emission rate by solving Eq. (139) numerically. It is well known that a phenomenological fitting

$$\omega\frac{dN^\gamma_{pheno.}}{d^3qd^4x} = \frac{5T^2\alpha\alpha_sf(q)}{18\pi^2}\left[\ln\frac{\sqrt{3}}{g}+\frac{1}{2}\ln\left(\frac{2\omega}{T}\right)+C_\mathrm{hard}\left(\frac{\omega}{T}\right)+C_\mathrm{coll.}\left(\frac{\omega}{T}\right)\right], \tag{143}$$

$$C_\mathrm{hard}(x) \simeq 0.041x^{-1}-0.3615+1.01\mathrm{e}^{-1.35x}, \tag{144}$$

$$C_\mathrm{coll.} \simeq \frac{4}{3}\left[\frac{0.548\ln(12.28+1/x)}{x^{3/2}}+\frac{0.133x}{\sqrt{1+x/16.27}}\right] \tag{145}$$

well reproduces the complete leading log result within an absolute error of 0.02 over the region $0.2 \leq \omega/T \leq 50$ [64, 65] We are interested in photons of order GeV which are detected in recent heavy ion collisions, and thus this phenomenological fitting is well applicable.

Analyses on thermal photon production rates are expanded to the next-to-leading order level recently [65]. The next-to-leading order contributions are arisen from higher order diagrams and expansion of kinematics. The obtained result shows that the correction enhances the rate at most 20% around $\omega/T \sim 2$. The correction effect becomes weaker as ω/T increases. Therefore, we will use the leading order result Eqs. (143), (144) and (145) to compare our results in Section 5.1.

3.4.4 Perturbative Dilepton Production Rate

The HTL analysis on dilepton [67, 68] is briefly reviewed in this subsection. The virtual photon self energy analyzed with the HTL resummed perturbation theory is illustrated as Fig. 18 In Fig. 18, propagators and vertices include one-loop thermal effects. In other word, the thermal propagator has the fermion self energy Eq. 95 and the photon-quark vertex is corrected by Eq. 118. The HTL virtual

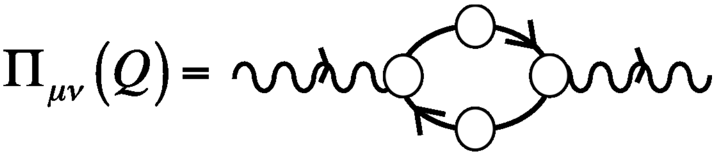

Figure 18: Photon self energy analyzed with the HTL perturbation theory. White circles mean each vertex and propagator is HTL one.

photon self energy in two flavor QCD is given by

$$\Pi^{\mathrm{HTL}}_{\mu\nu} = -\frac{5}{3}T\sum_{n}\int\frac{d^3p}{(2\pi)^3}\mathrm{Tr_D}[S^{\mathrm{HTL}}(P)\Gamma^{\mathrm{HTL}}_{\mu}(P,P+Q)S^{\mathrm{HTL}}(P+Q)\Gamma^{\mathrm{HTL}}_{\nu}(P+Q,P)]. \tag{146}$$

In the present study, we only consider the case of $\boldsymbol{q}=\boldsymbol{0}$. In this case, the HTL dilepton production rate is evaluated as

$$\left.\frac{d\mathrm{N}^{l^+l^-}_{\mathrm{HTL}}}{d\omega d^3q d^4x}\right|_{\boldsymbol{q}=\boldsymbol{0}}$$

$$= \frac{5\alpha^2}{36\pi^4\omega^2}\int_0^\infty dp p^2\int_{-\infty}^{\infty}\frac{dp_0}{2\pi}\int_{-\infty}^{\infty}\frac{dp'_0}{2\pi}f(p_0)f(p'_0)\delta(\omega-p_0-p'_0)\Bigg[4\left[1-\frac{p_0^2-p_0^{\prime 2}}{2p\omega}\right]^2\rho_+(p_0,p)\rho_-(p'_0,p)$$

$$+\left[1+\frac{p_0^2+p_0^{\prime 2}-2p^2-2m_{\mathrm{T}}^2}{2p\omega}\right]^2\rho_+(p_0,p)\rho_+(p'_0,p)+\left[1-\frac{p_0^2+p_0^{\prime 2}-2p^2-2m_{\mathrm{T}}^2}{2p\omega}\right]^2\rho_-(p_0,p)\rho_-(p'_0,p)$$

$$+\theta(p^2-p_0^2)\frac{m_{\mathrm{T}}^2}{4p\omega^2}\left(1-\frac{p_0^2}{p^2}\right)\left[\left(1+\frac{p_0}{p}\right)\rho_+(p'_0,p)+\left(1-\frac{p_0}{p}\right)\rho_-(p'_0,p)\right]\Bigg], \tag{147}$$

where spectral functions $\rho_\pm$ are given by Eq. (101). We comments on the obtained rate. From the structure of the spectral function which is composed of two poles and the continuum, one finds that the HTL dilepton production rate is constructed of pair annihilation, Landau damping and continuum parts. The dominance contributions are continuum parts and we confirm this fact in Section 5.2. When one substitutes one for Z_+, zero for Z_- and p for $\nu_\pm$, Eq. (147) becomes the one of free quark gas. This is the desirable behavior. When the virtual photon has the larger energy, $\omega \gg T$, quasi-particles concerning to the virtual photon radiation also have large energies. Thermal medium effects on such quasi-particles become relatively small. It is reflected on the dilepton production rate in higher invariant mass region as the spectrum gets to be similar to the one of free quark gas.

4 Analysis of Photon and Dilepton with Lattice Quark Propagator

It is indicated that the strongly coupled deconfined medium is produced in ultra-relativistic heavy ion collisions. When the medium is strongly coupled, the non-perturbative analysis is desirable. We attempt to evaluate thermal photon and dilepton production rates in a non-perturbative method.

Until now, no one succeeds in obtaining the exact photon self energy in QCD plasma. To avoid this problem, we use a quark propagator obtained in lattice QCD numerical simulation at finite temperature as an input. The non-perturbative effect is reflected on production rates by this method. Vertices are constructed to satisfy the Ward-Takahashi identity so as to respect the gauge invariance. In this section, first, the lattice quark propagator is overviewed. Next, we discuss our strategy to construct the vertex function. Then we analyze the photon self energy with the lattice quark propagator and the vertex. Finally, the relation between the kinematics of several production processes are discussed.

4.1 Exact Photon Self Energy

As discussed in Section 3.4, the thermal photon and dilepton production rates per unit time per unit volume from the static medium are related to the retarded photon self energy $\Pi^R_{\mu\nu}(\omega,\boldsymbol{q})$ as

$$\omega\frac{d\mathrm{N}^{\gamma}}{d^3q d^4x} = -\frac{1}{(2\pi)^3}\frac{1}{\mathrm{e}^{\beta\omega}-1}\mathrm{Im}\Pi^{R,\mu}_{\mu}(\omega,\boldsymbol{q}), \tag{148}$$

$$\frac{d\mathrm{N}^{l^+l^-}}{d\omega d^3q d^4x} = -\frac{\alpha}{12\pi^4}\frac{1}{Q^2}\frac{1}{\mathrm{e}^{\beta\omega}-1}\mathrm{Im}\Pi^{R,\mu}_{\mu}(\omega,\boldsymbol{q}), \tag{149}$$

at the leading order in the electromagnetic interaction and the all order in the strong interaction with the inverse temperature $\beta = 1/T$ [16–18]. The retarded photon self-energy is obtained from the imaginary time self energy by the analytic continuation,

$$\Pi^R_{\mu\nu}(\omega,\boldsymbol{q}) \quad = \quad \Pi_{\mu\nu}(i\omega_m,\boldsymbol{q})|_{i\omega_m\to\omega+i\eta}. \tag{150}$$

From Eqs. (148), (149) and (150) thermal production rates are obtained by evaluating the imaginary time photon self energy.

Now we focus on the full photon self energy. From the Schwinger-Dyson equation (SDE) in imaginary time formalism, the exact photon self-energy is given by the full quark propagator $S(P)$ and the full photon-quark vertex $\Gamma_\mu(P+Q,P)$ as

$$\Pi_{\mu\nu}(i\omega_m,\boldsymbol{q}) = -\sum_{\mathrm{f}} e_{\mathrm{f}}^2 T\sum_n \int\frac{d^3p}{(2\pi)^3}\mathrm{Tr_C Tr_D}[S(P)\gamma_\mu S(P+Q)\Gamma_\nu(P+Q,P)], \tag{151}$$

where $\omega_m = 2\pi Tm$ and $\nu_n = (2n+1)\pi T$ with integers m and n are the Matsubara frequencies for

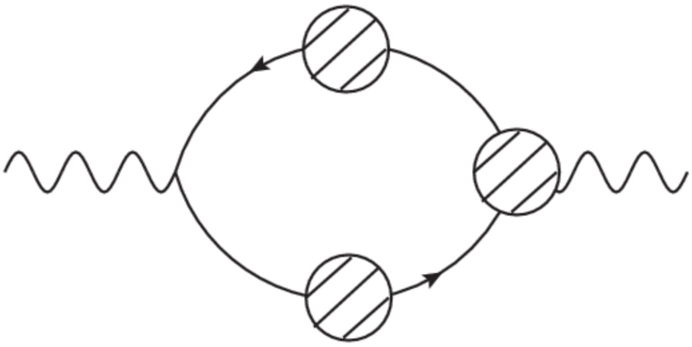

Figure 19: Diagrammatic representation of the Schwinger-Dyson equation for the full photon self-energy, Eq. (151). The shaded circles represent the full quark propagator and the full vertex function.

bosons and fermions, respectively, $P_\mu = (i\nu_n, \boldsymbol{p})$ is the four momentum of quarks, $Q_\mu = (i\omega_m, \boldsymbol{q})$ is the four momentum of the photon and $e_{\rm f}$ is the electric charge of the quark with an index "f" representing the quark flavor. The color, flavor, and Dirac indices of $S(P)$ are suppressed for notational simplicity. $\mathrm{Tr}_{\rm C}$ and $\mathrm{Tr}_{\rm D}$ denote the trace over the color and the Dirac indices, respectively. We note that we take the Landau gauge in this calculation. Off-diagonal elements in color space disappear and the trace over the color indices gives a factor 3 in Eq. (151). Equation (151) is graphically expressed in Fig. 19, in which the shaded circles represent the full propagator and the full vertex function. The left-side vertex is bare to avoid a double counting problem. In the following, we consider the two flavor system with degenerate u and d quarks, in which $\sum_{\rm f} e_{\rm f}^2 = (2e/3)^2 + (e/3)^2 = 5e^2/9$.

4.1.1 Lattice Quark Propagator and Spectral Function

Eq. (151) is exact, the non-perturbative formula of the photon self energy but one needs the full quark propagator S and the full photon-quark vertex Γ_ν to evaluate Eq. (151). In this study, we regard a quark propagator obtained on the lattice [19–21] as the full quark propagator and construct the gauge invariant vertex from the propagator to satisfy the Ward-Takahashi identity. We evaluate the photon self energy $\Pi_{\mu\nu}$ by substituting the lattice quark propagator and the vertex for S and Γ_ν in Eq. (151). This analysis is a non-perturbative calculation of the photon self energy. In this subsection, we discuss the lattice quark propagator.

As discussed in Section 3.2, the quark spectral function $\rho_{\mu\nu}(\nu, \boldsymbol{p})$ is related to the imaginary time correlator $S_{\mu\nu}(\tau, \boldsymbol{p})$ as

$$S_{\mu\nu}(\tau, \boldsymbol{p}) = \int_{-\infty}^{\infty} d\nu \frac{\mathrm{e}^{(1/2-\tau/\beta)\beta\nu}}{\mathrm{e}^{\beta\nu/2} + \mathrm{e}^{-\beta\nu/2}} \rho_{\mu\nu}(\nu, \boldsymbol{p}). \tag{152}$$

The left-hand side of Eq. (152) is analyzed numerically on the lattice for discrete imaginary times. To obtain the quark propagator, one has to deduce the spectral function from this information. In

Refs. [19–21], the quark correlator in the Landau gauge is analyzed on the lattice in the quenched approximation, and the quark spectral function is obtained with the two-pole ansatz,

$$\rho_+(\nu,p) = Z_+(p)\delta\left(\nu-\nu_+(p)\right) + Z_-(p)\delta\left(\nu+\nu_-(p)\right), \tag{153}$$

where $Z_\pm(p)$ and $\nu_\pm(p)$ are the residues and positions of the poles, respectively. The four parameters, $Z_\pm(p)$ and $\nu_\pm(p)$, are determined by fitting the correlators obtained on the lattice for each p.

Some comments on the two-pole fit in Refs. [19–21] are in order. First, the two poles in Eq. (153) at $\nu_+(p)$ and $\nu_-(p)$, respectively, correspond to the normal and plasmino modes in the HTL approximation. In fact, the study of the momentum and bare quark mass, m_0, dependences of the fitting parameters [19–21] shows that the behavior of these parameters is consistent with this interpretation [80, 82]; for example, for large m_0 or p the residue of the plasmino mode $Z_-(p)$ becomes small and the propagator approaches the one of the free quark. Second, the restoration of the chiral symmetry for massless quarks above T_c is checked explicitly on the lattice by measuring the scalar term in the massless quark propagator [20, 21]. Third, in Refs. [20, 21] the extension of the fitting ansatz to allow for the width of the poles are also performed. It, however, is found that the χ^2 of this fit always has a minimum for vanishing widths, and this extension does not improve the fit. This result indicates that the existence of sharp quasi-particle peaks in the quark spectral function even near T_c is supported from the lattice analysis.

It should be emphasized that a quark propagator depends on the gauge fixing in general. In Refs. [19–21], numerical simulations are performed in the Landau gauge. There is a possibility that obtained results are changed when one evaluates imaginary time correlators in other gauge. Therefore, it is desirable to study a gauge dependence of the quark propagator. However, it is revealed that the pole structure of the quark propagator is independent of the gauge fixing in Ref. [81]. In this case, it is expected that analyses of poles of the quark propagator do not change even in other gauges.

The quark propagator evaluated in lattice QCD numerical simulations are available only for discretized momenta. Although the lattice data are available only for discrete values of p, we must have the quark propagator as a continuous function of p to solve the SDE. For this purpose, we take the interpolation and extrapolation of the lattice data by the cubic spline method. From the charge conjugation symmetry one can show that $\mathrm{d}\nu_+(p)/\mathrm{d}p = -\mathrm{d}\nu_-(p)/\mathrm{d}p$, $\mathrm{d}^2\nu_+(p)/\mathrm{d}p^2 = \mathrm{d}^2\nu_-(p)/\mathrm{d}p^2$, and $Z_+(p) = Z_-(p)$ for $p = 0$ [19, 21], where $\nu_\pm(p)$ are the dispersion relations and $Z_\pm$ are the residues of the normal and plasmino modes, respectively. These properties are taken into account in our cubic spline interpolation. The lattice data are available only in the momentum range $p/T \lesssim 4.7$. To take extrapolations to higher momenta, we extrapolate the parameters using an exponentially damping form for $Z_-/(Z_+ + Z_-)$,

$$Z_-/(Z_+ + Z_-) = R\mathrm{e}^{-\alpha p}, \tag{154}$$

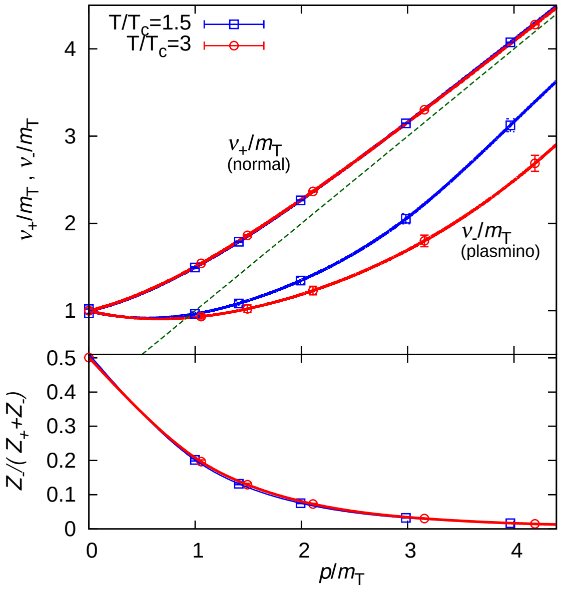

Figure 20: Open symbols show the momentum dependence of the parameters $\nu_+(p)$, $\nu_-(p)$, and $Z_-(p)/(Z_+(p)+Z_-(p))$ obtained on the lattice in Ref. [21]. The solid lines represent their interpolation obtained by the cubic spline method. The dashed line represents the light cone.

and $\nu_\pm(p)$ are extrapolated by functions,

$$\nu_\pm(p) = p + \beta_1^\pm \mathrm{e}^{-\beta_2^\pm p}, \tag{155}$$

which exponentially approach the light cone for large p. The parameters R, α, and $\beta_i^\pm$ are determined in the cubic spline analysis.

In Fig. 20, we show the fitting result of each parameter in Eq. (153) for massless quarks as the function of p for $T = 1.5T_\mathrm{c}$ and $3T_\mathrm{c}$ obtained in Ref. [21]. These analyses are performed on the lattice with the volume $128^3 \times 16$, where both the lattice spacing and finite volume effects are found to be small [21]. In the upper panel, p dependences of $\nu_\pm(p)$, i.e. the dispersion relations of the normal and plasmino modes, are shown by the open symbols. The vertical and horizontal axes are normalized by the thermal mass m_T defined by the value of $\nu_\pm(p)$ at $p = 0$: The value of m_T obtained on the lattice after the extrapolation to the infinite volume limit is $m_\mathrm{T}/T = 0.768(11)$ and $0.725(14)$ at $T = 1.5T_\mathrm{c}$ and $3T_\mathrm{c}$, respectively [21]. The lower panel shows the relative weight of the plasmino residue, $Z_-/(Z_+ + Z_-)$. This figure shows that the weight becomes smaller as p increases, which indicates that the quark propagator for large p/T is dominated by the normal mode. A result similar to that shown in Fig. 20 is obtained by the Schwinger-Dyson approach for the quark propagator [83]. We tested another extrapolation form by a polynomial, $\nu_\pm(p) = p + \beta_1'^\pm/p + \beta_2'^\pm/p^2 + \cdots$, but found that it hardly changes the dispersion relation. Finally, we fix

$$Z_{+} + Z_{-} = 1 \tag{156}$$

throughout this paper to satisfy the sum rule Eq. (81). As discussed in Section 3.2, the sum rule Eq. (81) can be altered by a renormalization. However, the structure of the spectral function does not have a continuum part in our fitting function Eq. (153), and thus Eq. (156) is expected to be fine. We note that the slope of the plasmino dispersion relation exceeds unity for $p \gtrsim 3m_{\mathrm{T}}$ and is acausal. This unphysical behavior may come from an artifact of the lattice simulation and/or the ansatz for the spectral function. However, the residue of the plasmino mode is small, $Z_{-}(p) < 0.05$, in this momentum region and the contribution of this branch in this momentum range to our final result is well suppressed. We discuss the suppression in Section 5.

The results shown in Fig. 20 are obtained in quenched approximation and the pseudo-critical temperature T_{c} is estimated as 290MeV. In full QCD, the form of the quark spectrum may be altered due to contributions of dynamical quark loops. It should also be noted that the T_{c} in the quenched approximation is estimated about 1.5 times larger than that of full QCD.

The quark which we consider is massless and its scalar term is zero. Therefore, the quark propagator can be decomposed as

$$\begin{aligned} S(i\nu_n, \boldsymbol{p}) &= S_{+}(i\nu_n, p)\Lambda_{+}(\boldsymbol{p})\gamma_0 + S_{-}(i\nu_n, p)\Lambda_{-}(\boldsymbol{p})\gamma_0, \\ &= \sum_{s=\pm 1} S_s(i\nu_n, p)\Lambda_s(\boldsymbol{p})\gamma_0, \end{aligned} \tag{157}$$

where we define $\Lambda_{\pm 1} = \Lambda_{\pm}$ and $S_{\pm 1} = S_{\pm}$. With the two-pole form of the spectral function Eq. (153), $S_{\pm}$ satisfies

$$S_s(i\nu_n, p) = \frac{Z_{+}(p)}{i\nu_n - s\nu_{+}(p)} + \frac{Z_{-}(p)}{i\nu_n + s\nu_{-}(p)}. \tag{158}$$

Correspondingly, the inverse propagator is given by

$$S^{-1}(i\nu_n, \boldsymbol{p}) = \sum_{s=\pm 1} S_s^{-1}(i\nu_n, p)\gamma_0\Lambda_s(\boldsymbol{p}), \tag{159}$$

with

$$S_s^{-1}(i\nu_n, p) = \frac{(i\nu_n - s\nu_{+}(p))(i\nu_n + s\nu_{-}(p))}{i\nu_n + sV(p)}, \tag{160}$$

and

$$V(p) = Z_{+}(p)\nu_{-}(p) - Z_{-}(p)\nu_{+}(p). \tag{161}$$

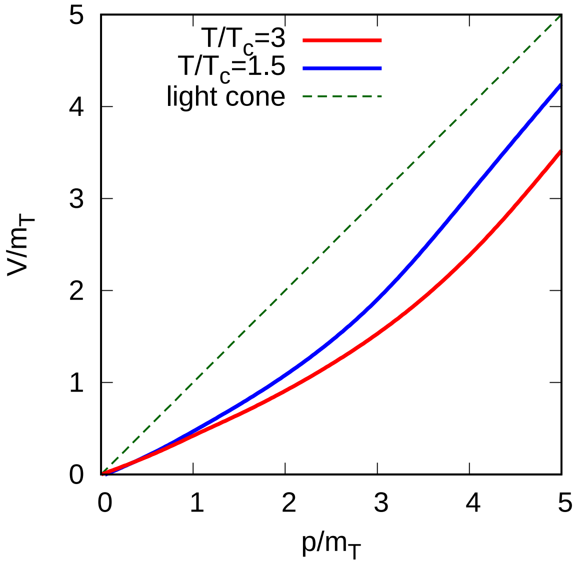

Figure 21: The p-dependence of the function $V(p)$ defined as Eq. (161). The horizontal and vertical axes are normalized with the thermal mass of the quasi-particle.

For notational convenience for the following analysis, we define $S_{\pm}^{-1} = S_{\pm 1}^{-1}$. Note that the inverse propagator has poles at $i\nu_n = \pm V(p)$. These poles inevitably appear in the multipole ansatz, because the propagator Eq. (158) has one zero point in the range of ν surrounded by two poles. The form of the inverse propagator Eq. (160) will be used in the construction of the vertex function. We will see that the poles at $i\nu_n = \pm V(p)$ give rise to additional terms in photon and dilepton production rates.

The p dependence of $V(p)$ defined as Eq. (161) is shown in Fig. 21 for two temperatures. One finds that $V(p)$ is the monotonically increasing function of p. One can evaluate $S_s^{-1}(\nu, p)$ from Eq. (160) by taking the analytic continuation of $i\nu_n \to \nu + i\varepsilon$. For a given ν, a solution p' can exist satisfying $\nu - V(p') = 0$ or $\nu + V(p') = 0$. Therefore, either S_+^{-1} or S_-^{-1} can have a divergence for the given photon energy. Owing to the divergence, the gauge invariant vertex Γ_μ has the pole which does not appear when the photon self energy is analyzed with bare vertices. We call this odd pole as the "anomalous" pole because real or virtual photon productions from this process cannot be interpreted as simple physical reactions between quasi-particles and photon. We will discuss details of this anomalous process in the following sections.

4.1.2 Gauge Invariant Vertex

In this subsection, we consider the gauge invariant vertex function. The full photon self energy, Eq. (151), requires the full photon-quark vertex $\Gamma_\mu(P+Q, P)$ besides the full quark propagator. So far, the evaluation of $\Gamma_\mu(P+Q, P)$ on the lattice at nonzero temperature has not been performed. In the present study, we construct the vertex function from the lattice quark propagator respecting the

Ward-Takahashi identity (WTI) as follows.

The gauge invariance requires that the vertex function fulfills the WTI

$$Q_\mu \Gamma^\mu(P+Q,P) = S^{-1}(P+Q) - S^{-1}(P), \tag{162}$$

with the inverse quark propagator $S^{-1}(P)$. In this study, we suppose

$$\begin{aligned}&\Gamma_0(i\omega_m + i\nu_n, \boldsymbol{p}+\boldsymbol{q}; i\nu_n, \boldsymbol{p})\\ =&\frac{1}{2i\omega_m}\left[S^{-1}(i\omega_m + i\nu_n, \boldsymbol{p}+\boldsymbol{q}) - S^{-1}(i\nu_n, \boldsymbol{p}+\boldsymbol{q}) + S^{-1}(i\omega_m + i\nu_n, \boldsymbol{p}) - S^{-1}(i\nu_n, \boldsymbol{p})\right],\end{aligned} \tag{163}$$

and

$$\begin{aligned}&\Gamma_i(i\omega_m + i\nu_n, \boldsymbol{p}+\boldsymbol{q}; i\nu_n, \boldsymbol{p})\\ =&\gamma_i - \frac{q_i}{2q^2}\left[S^{-1}(i\omega_m + i\nu_n, \boldsymbol{p}+\boldsymbol{q}) + S^{-1}(i\nu_n, \boldsymbol{p}+\boldsymbol{q}) - S^{-1}(i\omega_m + i\nu_n, \boldsymbol{p}) - S^{-1}(i\nu_n, \boldsymbol{p})\right] - \frac{q_i(\boldsymbol{q}\cdot\boldsymbol{\gamma})}{q^2}.\end{aligned} \tag{164}$$

These forms of the phenomenological vertex Eqs. (163) and (164) satisfy the WTI Eq. (162). It should be emphasized that a different choice of vertices which satisfies the WTI can be constructed from the same quark propagator because the number of constraints are not enough to determine the four components of vertices uniquely [78]. However, our vertex respects the gauge invariance at least, and thus we can analyze the photon and dilepton production rates gauge invariantly.

Other characteristic of Eqs. (163) and (164) is that they approach bare vertices when the momentum of outline Q is large enough. We can easily check this behavior. In high momentum region where $P+Q, Q \gg T$, as discussed in Section 3.3.3, the quark propagator behaves as the bare propagator because the effect of thermal scatterings on the quark becomes smaller. Substitute the inverse bare quark propagator $S^{-1}(P) = \not{p}$ for Eqs. (163) and (164), one obtains

$$\Gamma_0(P+Q,P) \to \frac{1}{2i\omega_m}\cdot 2\omega_m\gamma_0 = \gamma_0, \tag{165}$$

$$\Gamma_i(P+Q,P) \to \gamma_i + \frac{q_i}{2q^2}\cdot 2\boldsymbol{q}\cdot\boldsymbol{\gamma} - \frac{\gamma_i(\boldsymbol{q}\cdot\boldsymbol{\gamma})}{q^2} = \gamma_i. \tag{166}$$

Eqs. (165) and (166) seem to imply that the photon emission rate with high energy $\omega \gg T$ approaches zero and the dilepton emission rate with large invariant mass $Q^2 \gg T^2$ approaches the rate obtained from the free quark gluon gas because the quasi-particle approaches to the bare quark when its momentum is much larger than the temperature. The latter is correct but the former situation does not happen. Certainly, one obtains the one-loop diagram when one substitutes the free quark propagator and the bare vertex for Eq. (151), and its imaginary part vanishes for on-shell photons. However, the decay of the high energy normal state to high energy photon and low energy plasmino state has non zero strength even the energy of photon is enough high $\omega \gg T$. Therefore, the radiation of high energy photons are permitted. We discuss details in the following section.

4.1.3 Gauge Invariant Vertex with $\boldsymbol{q} = 0$

In this study, we evaluate the dilepton production rate at zero momentum. To make the analysis simple, we construct the vertex $\Gamma_\mu(i\omega_m + i\nu_n, \boldsymbol{p}; i\nu_n, \boldsymbol{p})$ by the following procedure.

In the present study, we employ an approximation to neglect the $\boldsymbol{q}$ dependence of $\Gamma_0(i\omega_m + i\nu_n, \boldsymbol{p}+\boldsymbol{q}; i\nu_n, \boldsymbol{p})$ at $\boldsymbol{q} = 0$. In other words we assume that

$$\partial\Gamma_0(i\omega_m + i\nu_n, \boldsymbol{p}+\boldsymbol{q}; i\nu_n, \boldsymbol{p})/\partial q_i|_{\boldsymbol{q}=0} = 0. \tag{167}$$

With this approximation and Eq. (162), one obtains

$$q^i\Gamma_i(i\omega_m + i\nu_n, \boldsymbol{p}+\boldsymbol{q}; i\nu_n, \boldsymbol{p}) = S^{-1}(i\omega_m + i\nu_n, \boldsymbol{p}+\boldsymbol{q}) - S^{-1}(i\omega_m + i\nu_n, \boldsymbol{p}). \tag{168}$$

By taking the leading-order terms in $\boldsymbol{q}$ on the both sides, one has

$$\begin{aligned}\Gamma_i(i\omega_m + i\nu_n, \boldsymbol{p}; i\nu_n, \boldsymbol{p}) &= \frac{\partial S^{-1}}{\partial p^i}(i\omega_m + i\nu_n, \boldsymbol{p}) \\ &= \sum_{s=\pm 1} \frac{\partial S_s^{-1}(i\omega_m + i\nu_n, p)}{\partial p^i}\gamma_0\Lambda_s(\boldsymbol{p}) + \sum_{s=\pm 1} S_s^{-1}(i\omega_m + i\nu_n, p)\gamma_0\frac{\partial\Lambda_s(\boldsymbol{p})}{\partial p^i},\end{aligned} \tag{169}$$

where in the second equality, we used Eq. (159).

It should be emphasized that there is no a priori justification of Eq. (167). However, our phenomenological vertex still satisfies the Ward-Takahashi identity, and thus it respects the gauge invariance which makes the important role in the quantum field theory.

4.2 Analysis of Production Rate

The purpose of this study is to obtain photon and dilepton production rates with the lattice quark propagator and gauge invariant vertex. In this subsection, however, before the analysis of the full manipulation we first see production rates in simpler cases: (1) free quark gas in Section 4.2.1, and (2) case with the lattice quark propagators but with the bare vertex in Section 4.3. The full analysis of the photon self energy is then given in Section 4.4.

We will show numerical results in the next section, but we reveal physical production processes corresponding to each term in obtained results in Sections 4.3 and 4.4.

In each calculation, we first analyze the photon self energy (151) and evaluate the imaginary part. Then, we suppose the on-shell photon and obtain thermal photon production rates. Next, we consider virtual photons with $\boldsymbol{q} = \boldsymbol{0}$. In this case, virtual photons become dileptons in final states and the lepton and anti-lepton are emitted back-to-back in the center-of-mass frame of the photon.

4.2.1 Free quark gas

The photon self energy for the massless free quark gas is obtained by substituting the free quark propagator $S(P) = 1/\not{p}$ and the bare vertex $\Gamma_\nu = \gamma_\nu$ into Eq. (151). The photon self energy is given by

$$\Pi_{\mu\nu}(i\omega_m, \boldsymbol{q}) = -\frac{5}{3}e^2 T \sum_n \int \frac{d^3p}{(2\pi)^3} \mathrm{Tr}_{\mathrm{D}} \left[\frac{1}{\not{p}} \gamma_\mu \frac{1}{\not{p} + \not{q}} \gamma_\nu \right]. \tag{170}$$

As $\mathrm{Tr}_{\mathrm{D}}[\not{p}\gamma_\mu(\not{p}+\not{q})\gamma^\mu] = -8p \cdot (p+q)$, the trace of the photon self energy Eq. (170) is evaluated as

$$\begin{aligned} \Pi^\mu_\mu(i\omega, \boldsymbol{q}) &= \frac{40}{3}e^2 T \sum_n \int \frac{d^3p}{(2\pi)^3} \frac{p\cdot(p+q)}{P^2(P+Q)^2} \\ &= \frac{40}{3}e^2 T \sum_n \int \frac{d^3p}{(2\pi)^3} \sum_{s,t=\pm1} \frac{s}{i\nu_n - sp} \cdot \frac{t}{i\nu_n + i\omega_m - t|\boldsymbol{p}+\boldsymbol{q}|} \frac{i\nu_n(i\omega_m + i\nu_n) - p|\boldsymbol{p}+\boldsymbol{q}|}{4p|\boldsymbol{p}+\boldsymbol{q}|} \\ &= \frac{40}{3}e^2 T \sum_n \int \frac{d^3p}{(2\pi)^3} \sum_{s,t=\pm1} \frac{st}{4p|\boldsymbol{p}+\boldsymbol{q}|} \\ &\quad \times \left[1 - \frac{sp}{i\nu_n - sp} - \frac{t|\boldsymbol{p}+\boldsymbol{q}|}{i\nu_n + i\omega_m - t|\boldsymbol{p}+\boldsymbol{q}|} + \frac{sp}{i\nu_n - sp} \cdot \frac{t|\boldsymbol{p}+\boldsymbol{q}|}{i\nu_n + i\omega_m - t|\boldsymbol{p}+\boldsymbol{q}|} \right], \end{aligned} \tag{171}$$

where we takes the factorization in the third equality. When one takes the analytic continuation $i\omega_m \to \omega + i\varepsilon$ and evaluate the retarded photon self energy, only the fourth term in the second line has the imaginary part, and thus we ignore other terms. We takes the Matsubara sum in Eq. (171). The Matsubara sum on the fermion frequency is given by

$$T \sum_n \frac{1}{i\nu_n - E_1} \cdot \frac{1}{i\omega_m + i\nu_n - E_2} = \frac{f(E_1) - f(E_2)}{i\omega_m + E_1 - E_2}, \tag{172}$$

where $f(E) = 1/(\mathrm{e}^{\beta E} + 1)$ is the Fermi distribution function. The fourth term in the second line in Eq. (171) becomes

$$\frac{10}{3}e^2 \int \frac{d^3p}{(2\pi)^3} \sum_{s,t=\pm1} \frac{f(sp) - f(t|\boldsymbol{p}+\boldsymbol{q}|)}{i\omega_m + sp - t|\boldsymbol{p}+\boldsymbol{q}|}. \tag{173}$$

Now, we consider $1/x + i\eta'$ to extract the imaginary part of the photon self energy. $1/x + i\eta'$ with the positive infinitesimal number η' is expressed as

$$\frac{1}{x + i\eta'} = \mathscr{P}\frac{1}{x} - i\pi\delta(x), \tag{174}$$

where $\mathscr{P}1/x$ is the principal part of $1/x$. Therefore, the trace of the imaginary part of the retarded photon self energy in free quark gas case is evaluated as

$$\mathrm{Im}\Pi^{R,\mu}_{\mu}(\omega,\boldsymbol{q}) = -\frac{10\pi e^2}{3}\int\frac{d^3p}{(2\pi)^3}\sum_{s,t=\pm1}[f(sp)-f(t|\boldsymbol{p}+\boldsymbol{q}|)]\delta(\omega+sp-t|\boldsymbol{p}+\boldsymbol{q}|). \tag{175}$$

In the case of free quark gas, the photon production rate is trivially zero because the photon production via a pair annihilation to real photon $q\bar{q}\to\gamma$ and a spontaneous photon emission without gluon scattering $q\to q\gamma$ are forbidden kinematically. Mathematically, the set of $(\omega,\boldsymbol{q},\boldsymbol{p})$ which satisfies both $\omega=|\boldsymbol{q}|$ and $\omega+sp-t|\boldsymbol{p}+\boldsymbol{q}|=0$ exists only when $\boldsymbol{p}=\boldsymbol{0}$ or $-2\boldsymbol{q}$. In this case, the phase space becomes zero and the loop integral $\int d^3p/(2\pi)^3$ in Eq. (175) gives zero.

On the other hand, the non-zero value of the dilepton production rate with $\boldsymbol{q}=\boldsymbol{0}$ is obtained as [82]

$$\left.\frac{dN^{l^+l^-}}{d\omega d^3q d^4x}\right| = \frac{5\alpha^2}{36\pi^4}(f(\omega/2))^2. \tag{176}$$

4.3 Photon Self Energy without Vertex Correction

Next, we evaluate the photon self energy constructed with the lattice quark propagator obtained in Section 4.1.1 and the bare vertex. In this case, the photon self energy for the two flavor QCD is given by

$$\Pi_{\mu\nu}(i\omega_m,\boldsymbol{q}) = -\frac{5}{3}e^2T\sum_n\int\frac{d^3p}{(2\pi)^3}\mathrm{Tr}_{\mathrm{D}}[S(P)\gamma_\mu S(P+Q)\gamma_\nu], \tag{177}$$

where S is the lattice quark propagator.

In analyses of Eq. (177) and the self energy evaluated with the lattice quark propagator and the gauge invariant vertex, the traces including projection operators $\Lambda_\pm$ frequently appear which are calculated to be

$$\mathrm{Tr}_{\mathrm{D}}[\Lambda_s(\boldsymbol{p})\Lambda_t(\boldsymbol{p}+\boldsymbol{q})] = \frac{st}{2p_1p_2}[(sp_1+tp_2)^2-q^2], \tag{178}$$

$$\sum_i q_i\mathrm{Tr}_{\mathrm{D}}[\Lambda_s(\boldsymbol{p})\gamma_0\gamma_i\Lambda_t(\boldsymbol{p}+\boldsymbol{q})] = st[(sp_1+tp_2)^2-q^2]\frac{tp_2-sp_1}{2p_1p_2}, \tag{179}$$

$$\sum_{i=1}^{3} q_i\mathrm{Tr}_{\mathrm{D}}[\Lambda_s(\boldsymbol{p})\gamma_0\gamma_i\Lambda_t(\boldsymbol{p}+\boldsymbol{q})\gamma_0\gamma_i] = 4-\frac{st}{2p_1p_2}[(sp_1+tp_2)^2-q^2], \tag{180}$$

$$\mathrm{Tr}_{\mathrm{D}}[\Lambda_s(\boldsymbol{p})\gamma_0(\boldsymbol{q}\cdot\boldsymbol{\gamma})\Lambda_t(\boldsymbol{p}+\boldsymbol{q})\gamma_0(\boldsymbol{q}\cdot\boldsymbol{\gamma})] = 1-\frac{st}{2p_1p_2}\left[(p_1^2+p_2^2-q^2)+\frac{(p_1^2-p_2^2)^2-q^4}{q^2}\right], \tag{181}$$

with $\boldsymbol{p}_1=\boldsymbol{p}$ and $\boldsymbol{p}_2=\boldsymbol{p}+\boldsymbol{q}$. From Eqs. (157), (178), and (180), the trace of the the photon self energy

Eq. (177) is evaluated as

$$\Pi^{\mu}_{\mu}(i\omega_m,\boldsymbol{q}) = -\frac{5e^2}{12\pi^2 q} T\sum_n \sum_{s,t=\pm1} \int dp_1 dp_2 [st[(sp_1+tp_2)^2-q^2]-4p_1p_2] S_s(i\nu_n,p_1) S_t(i\omega_m+i\nu_n,p_2), \tag{182}$$

where we transform the integral measure as

$$\int \frac{d^3p}{(2\pi)^3} = \int_0^{\infty} \frac{dp_1}{2\pi} \int_0^{\infty} \frac{dp_2}{2\pi} \frac{p_1p_2}{q}. \tag{183}$$

Substituting the quark propagator obtained with the two-pole ansatz Eq. (158) into Eq. (182), taking the analytic continuation Eq. (150) and taking the imaginary part, one obtains the imaginary part of the retarded photon self energy,

$$\begin{aligned}\mathrm{Im}\Pi^{R,\mu}_{\mu}(\omega,\boldsymbol{q}) =& \frac{5e^2}{12\pi q} \sum_{\substack{s,t,\eta_1,\eta_2\\=\pm1}} \int dp_1 dp_2 Z_{\eta_1}(p_1) Z_{\eta_2}(p_2) [st[(sp_1+tp_2)^2-q^2]-4p_1p_2] \\ & \times [f(s\eta_1\nu_{\eta_1}(p_1)) - f(t\eta_2\nu_{\eta_2}(p_2))] \delta(\omega + s\eta_1\nu_{\eta_1}(p_1) - t\eta_2\nu_{\eta_2}(p_2)).\end{aligned} \tag{184}$$

From Eqs. (148) and (184), the production rate of thermal real photons is evaluated as

$$\begin{aligned}\omega\frac{N^{\gamma}_{\mathrm{NoV.C.}}}{d^3qd^4x} =& -\frac{5\alpha}{24\pi^3}\cdot\frac{1}{\mathrm{e}^{\beta\omega}-1} \sum_{\substack{s,t,\eta_1,\eta_2\\=\pm1}} \int dp_1 dp_2 Z_{\eta_1}(p_1) Z_{\eta_2}(p_2) [st[(sp_1+tp_2)^2-\omega^2]-4p_1p_2] \\ & \times [f(s\eta_1\nu_{\eta_1}(p_1)) - f(t\eta_2\nu_{\eta_2}(p_2))] \delta(\omega + s\eta_1\nu_{\eta_1}(p_1) - t\eta_2\nu_{\eta_2}(p_2)).\end{aligned} \tag{185}$$

We can gain insight on the thermal photon production from Eq. (185). Before we calculate the photon production rate with the gauge invariant vertex Eqs. (163) and (164), let us discuss details.

First, the δ-function in Eq. (185) simply expresses the energy conservation and it is a constraint for integrals on the (p_1,p_2) plane. The coefficient $st[(sp_1+tp_2)^2-\omega^2]-4p_1p_2$ is arisen from the trace over Dirac indices.

Next, we discuss the thermal factor $f(s\eta_1\nu_{\eta_1}(p_1)) - f(t\eta_2\nu_{\eta_2}(p_2))$ in Eq. (185). One can obtain a kinematics of photon and quasi-particles from the structure of the factor. For simplicity, we suppose the positive ω. This condition is reasonable because observed photons have positive energies. For a given set of (s,t,η_1,η_2), $f(s\eta_1\nu_{\eta_1}(p_1)) - f(t\eta_2\nu_{\eta_2}(p_2))$ becomes $1-f(\nu_1)-f(\nu_2)$ or $f(\nu_1)-f(\nu_2)$ with $\nu_1=\nu_{\pm}(p_1)$ and $\nu_2=\nu_{\pm}(p_2)$. When the thermal factor becomes $1-f(\nu_1)-f(\nu_2)$, the thermal factor can be rewritten as

$$1-f(\nu_1)-f(\nu_2) = (1-f(\nu_1))(1-f(\nu_2)) - f(\nu_1)f(\nu_2), \tag{186}$$

this is the difference between the products of thermal distributions and Pauli blocking effects. The term in Eq. (185) proportional to $1-f(\nu_1)-f(\nu_2)$ has the δ-function $\delta(\omega-\nu_1-\nu_2)$. The δ-function is the energy conservation, and thus the corresponding term expresses the photon emission from the quasi-particle "pair annihilation" shown in Fig. 22(a). In this case, the quasi-particle and anti-quasi-particle pair annihilate to the photon and the final state photon has the energy $\nu_1+\nu_2$. Although the photon production formula Eq. (148) takes only the photon emission term of $\mathrm{Im}\Pi_{\mu}^{R,\mu}$, $\mathrm{Im}\Pi_{\mu}^{R,\mu}$ itself is the difference between the photon production from the hot medium and the photon absorption by the medium. However, Eqs. (148) and (149) are real and virtual photon "production" rates, it is implied that multiplying the Bose distribution function $1/(e^{\beta\omega}-1)$ corresponds to extract emission contributions from $\mathrm{Im}\Pi_{\mu}^{R,\mu}$.

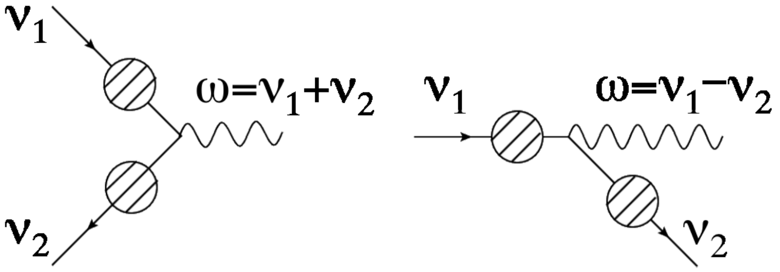

(a) Pair annihilation (b) Landau damping

Figure 22: Photon production processes with quasi-particles. Shaded circles mean quasi-particles are full.

Next, we consider the case of $f(\nu_1)-f(\nu_2)$. This thermal factor can be rewritten as

$$f(\nu_1)-f(\nu_2) = f(\nu_1)(1-f(\nu_2))-(1-f(\nu_1))f(\nu_2). \tag{187}$$

Eq. (187) is the difference between two products of the thermal distribution and the Pauli blocking effect. It means that both initial and final states include quasi-particle as shown in Fig. 22(b). The corresponding photon production process is called "Landau damping" [73]. Owing to the thermal effect, quark dispersions split and the photon emission via Landau damping is allowed which is forbidden in the case of free quark gas.

Next, let us consider a consistency between residues $Z_{\pm}$ in Eq. (185) and the interpretation of photon production processes. Both photon production processes include two quasi-particles. Residues $Z_{\pm}$ can be interpreted as presence strength of each quasi-particle. Photon production events are depends on the strength, and thus the residue of the quasi-particle $Z_{\pm}$ appears twice in Eq. (185). As mentioned above, each term in Eq. (185) can be interpreted as the physical process of pair annihilation and scattering of quasi-particles.

4.3.1 Kinematics of Photon Production Processes

It should be emphasized that the real photon is never emitted via the quasi-particle pair annihilation when the quasi-particle has HTL or free quark dispersion. In both cases, the pair annihilation process is forbidden kinematically. However, when one analyzes Eq. (185) with the lattice quark propagator obtained in Refs. [19–21], the photon emission via the quasi-particle pair annihilation is possible owing to the peculiar structure of "plasmino" dispersion shown in Fig. 20. The crucial difference between the lattice plasmino and the HTL plasmino is that the plasmino dispersion obtained on the lattice invades even in the space-like region. This structure permits the photon emission via quasi-particle pair annihilations. Let us discuss kinematics of photon and quasi-particles with the quasi-particle dispersion shown in Fig. 20. The pair annihilation of the normal quasi-particle and anti-quasi-particle does not emit the on-shell photon in perturbative analyses. In Fig. 23(a), we illustrate the minimum energy of photon for a given momentum q for each pair annihilation process at $T/T_{\mathrm{c}} = 1.5$. The plasmino-plasmino pair annihilation emits photons with energies $> 2.00 m_{\mathrm{T}} \approx 0.63\mathrm{GeV}$ and the normal-plasmino pair annihilation emits photons with energies $> 2.58 m_{\mathrm{T}} \approx 0.86\mathrm{GeV}$. Dispersions of $\nu_+ + \nu_-$ and $\nu_- + \nu_-$ exist even in space-like region, and thus these photons can be on-shell. We also illustrate maximum values of photons arisen from Landau damping in Fig. 23(b). One finds that Landau damping between two normal modes is forbidden kinematically. In contrast to the pair annihilation, as discussed in Section 3, some Landau damping processes in which just only three particles participate are already treated in perturbative analyses. Remember the diagram shown in Fig. 15 which is composed of the bare quark, the HTL quark and bare vertices. The HTL quark spectral function has two poles, and thus the decay process corresponding to the diagram in Fig. 15 includes the contribution from the Landau damping with three particles. However, the dispersions of lattice quasi-particles are different from the perturbative ones, and thus the kinematics of Landau damping is also changed. It should be emphasized that the cutoff which separates soft scale gT and hard scale T does not exist in our analysis. In Refs. [61, 62], the diagram shown in Fig. 15 which includes the contribution from Landau damping is considered in soft region. On the other hand, the hard photon production via Landau damping of quasi-particles is possible in our analysis. In fact, we will see that a part of photons with higher energy, $\omega \geq T$, are produced by Landau damping in Section 5.1. In this way, photon production mechanisms in our analysis are greatly different from those of perturbative analysis.

4.3.2 Kinematics and Integral Region

Next, we discuss a concrete method of integrations in our analysis. Remember we define momenta of two quarks as $\boldsymbol{p}_1 = \boldsymbol{p}$ and $\boldsymbol{p}_2 = \boldsymbol{p} + \boldsymbol{q}$ with the quark momentum $\boldsymbol{p}$ and the photon momentum $\boldsymbol{q}$. Then, the on-shell condition $\omega = q$ can be transformed as $|\boldsymbol{p}_2 - \boldsymbol{p}_1| = q$, and thus one obtains relations between p_1, p_2 and q as $p_2 \leq p_1 + q$, $p_2 \geq p_1 - q$ and $p_2 \geq -p_1 + \omega$ in the first quadrant of the (p_1, p_2)

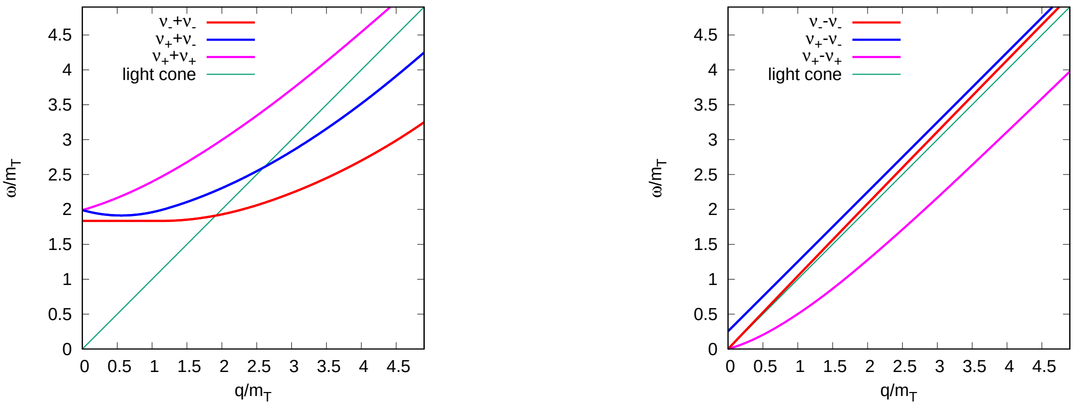

(a) Dispersions of pair annihilation

(b) Dispersions of Landau damping

Figure 23: Dispersion relations for photons produced via pair annihilation and Landau damping at $T/T_{\rm c} = 1.5$. For given q, minimum values are illustrated in the left panel and maximum values are illustrated in the right panel.

plane. Now, the integral region in Eq. (185) is limited as the region I sketched in Fig. 24(a).

Now, we consider a restriction on p_1 and p_2 integrals arising from the structure of the lattice quasi-particle dispersion shown in Fig. 20. Besides the restriction arisen from the on-shell condition, the structure of dispersions gives an additional restriction on the (p_1, p_2) plane with the δ-function in Eq. (185) which represents the energy conservation. Sets of (p_1, p_2) which satisfy the given energy conservation form a line on the (p_1, p_2) plane. As a result, one has to integrate along the line in the region I to evaluate contributions of each photon production. We illustrate an example of the contour in Fig. 24(b). In Fig. 24(b), we takes $\omega = 5m_{\rm T}$ and the contour satisfies $\nu_+(p_1) + \nu_-(p_2) = \omega$. One has to evaluate the integrals in Eq. (185) along the contour in the region I. We will discuss details of each energy conservation with the lattice quark propagator [19–21] in Section 5.

We consider the dilepton production rate with $\boldsymbol{q} = \boldsymbol{0}$ in this study. When $\boldsymbol{q} = \boldsymbol{0}$, the double integral in Eq. (185) turns to a single integral. From Eq. (185), the thermal dilepton production rate with $\boldsymbol{q} = \boldsymbol{0}$ is calculated as

$$
\begin{aligned}
\left.\frac{dN^{l^+l^-}}{d\omega d^3q d^4x}\right|_{\boldsymbol{q}=\boldsymbol{0}} = \frac{10\alpha^2}{9\pi^4}\frac{1}{\omega^2}\frac{1}{e^{\beta\omega}-1}\int_0^\infty & dp p^2 [Z_+(p)^2[1-2f(\nu_+(p))]\delta(\omega - 2\nu_+(p)) \\
& + Z_-(p)^2[1-2f(\nu_-(p))]\delta(\omega - 2\nu_-(p)) \\
& + 2Z_+(p)Z_-(p)[f(\nu_-(p)) - f(\nu_+(p))]\delta(\omega - \nu_+(p) + \nu_-(p))].
\end{aligned}
\tag{188}
$$

In this case, two normal quasi-particle pair annihilation is allowed because the emitted photon is off-shell. However, owing to the constraint $\boldsymbol{q} = \boldsymbol{0}$, normal and plasmino pair annihilation process and Landau damping between two normal quasi-particles and two plasmino quasi-particles are for-

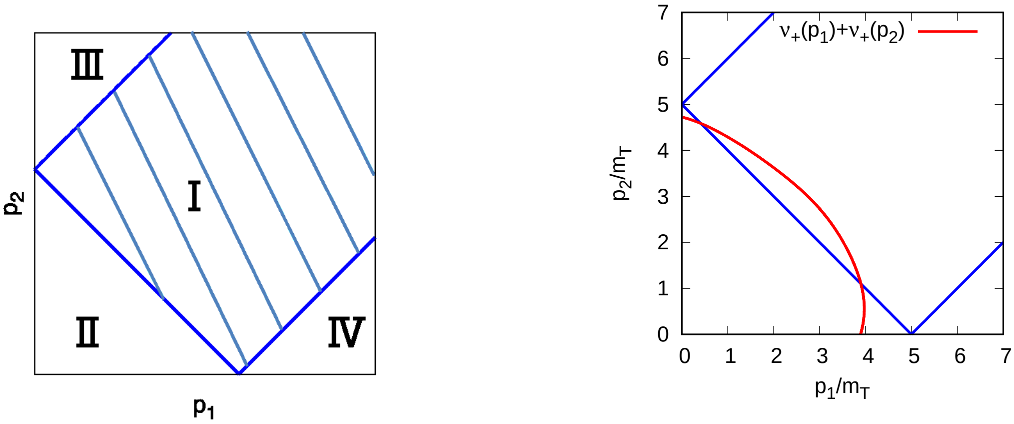

(a) Schematic for the p_1 and p_2 integral region in Eq. (185)

(b) The contour which satisfies $\nu_+(p_1)+\nu_-(p_2)=5m_T$ at $T=1.5T_{\mathrm{c}}$

Figure 24: Kinematical constraints on the p_1 and p_2 integrals in photon self energy.

bidden kinematically. These kinematics between quasi-particles and photon are not changed by the vertex correction, and thus photons and dileptons are produced via quasi-particle pair annihilation and Landau damping even in the full analysis.

By evaluating the p-integral in Eq. (188), one can gain a deeper insight on the dilepton production. The form of the dilepton production rate after the integration over p reads

$$
\begin{aligned}
\left.\frac{dN^{l^+l^-}}{d\omega d^3q d^4x}\right|_{q=0} = \frac{10\alpha^2}{9\pi^4}\frac{1}{\omega^2}\frac{1}{\mathrm{e}^{\beta\omega}-1}\Bigg[& \left.\frac{p^2 Z_+(p)^2}{2|d\nu_+(p)/dp|}[1-2f(\nu_+(p))]\right|_{\omega=2\nu_+(p)} \\
& +\sum_l \left.\frac{p_l^2 Z_-(p_l)^2}{2|d\nu_-(p_l)/dp|}[1-2f(\nu_-(p_l))]\right|_{\omega=2\nu_-(p_l)} \\
& +\sum_l \left.\frac{2p_l^2 Z_+(p_l)Z_-(p_l)}{|d[\nu_+(p_l)-\nu_-(p_l)]/dp|}[f(\nu_-(p_l))-f(\nu_+(p_l))]\right|_{\omega=\nu_+(p_l)-\nu_-(p_l)}\Bigg],
\end{aligned}
\tag{189}
$$

where the momentum p in each term is given by the condition arising from the δ-functions in Eq. (188). Each term can take nonzero values only when there exist momenta satisfying this condition for a given ω. This gives the condition for ω at which each term takes a nonzero value. For example, the first term takes nonzero values for $\omega > 2m_{\mathrm{T}}$. Because the second and third terms can have multiple solutions of p for a fixed ω, we represent this possibility by the sum over l. It is also notable that each term in Eq. (189) is inversely proportional to the derivative of $\nu_\pm(p)$ and $\nu_+(p)-\nu_-(p)$; they come from the density of states of each mode. Accordingly, the dilepton production rate diverges when the derivatives vanish. Such divergence is known as van Hove singularity. In Section 5.2, we will see the appearance of such singularities in the dilepton spectrum.

4.4 Photon Self Energy with Gauge Invariant Vertex

Now let us analyze the photon self energy with the lattice quark propagator and the gauge invariant vertex.

The production rates Eqs. (148) and (149) is proportional to $\mathrm{Im}\Pi^{R,\mu}_{\mu}$, and thus we have to analyze diagonal components of $\Pi^{R}_{\mu\nu}$. First, we consider Π_{00}. The trace part is evaluated as

$$
\begin{aligned}
&\mathrm{Tr_D}[S(P_1)\gamma_0 S(P_2)\Gamma_0(P_2,P_1)]\\
&=\sum_{s,t=\pm1}\frac{1}{2i\omega_m}\mathrm{Tr_D}[\Lambda_s(p_1)\Lambda_t(p_2)]\\
&\quad\times\left[S_s(i\nu_n,p_1)\left[1-\frac{S_t(i\omega_m+i\nu_n,p_2)}{S_t(i\nu_n,p_2)}\right]-S_t(i\omega_m+i\nu_n,p_2)\left[1-\frac{S_s(i\nu_n,p_1)}{S_s(i\omega_m+i\nu_n,p_1)}\right]\right]\\
&=\sum_{s,t=\pm1}\frac{1}{2i\omega_m}\mathrm{Tr_D}[\Lambda_s(p_1)\Lambda_t(p_2)]\\
&\quad\times i\omega_m\left[\sum_{\varepsilon_1=\pm1}S_s(i\nu_n,p_1)\frac{Z_{\varepsilon_1}(p_2)(i\nu_n+t\varepsilon_1\nu_{\bar{\varepsilon}_1}(p_2))}{(i\omega_m+i\nu_n-\varepsilon_1 t\nu_{\varepsilon_1}(p_2))(i\nu_n+tV(p_2))}\right.\\
&\qquad\left.+\sum_{\varepsilon_2=\pm1}S_t(i\omega_m+i\nu_n,p_2)\frac{Z_{\varepsilon_2}(p_1)(i\omega_m+i\nu_n+s\varepsilon_2\nu_{\bar{\varepsilon}_2}(p_1))}{(i\nu_n-\varepsilon_2 s\nu_{\varepsilon_2}(p_1))(i\omega_m+i\nu_n+sV(p_1))}\right],
\end{aligned}
\tag{190}
$$

where $\bar{\nu}(p)=\nu_+(p)+\nu_-(p)$ and $\nu_{\bar{\varepsilon}}=\nu_{-\varepsilon}$. We substitute the quark propagator obtained with the two-pole ansatz Eq. (158) into $S_{s,t}$ in the second equality.

From Eqs. (151), (158), (178), (183) and (190), Π_{00} is evaluated as

$$
\begin{aligned}
&\Pi_{00}(i\omega_m,\boldsymbol{q})\\
&=-\frac{5e^2}{12}T\sum_{n}\sum_{\substack{s,t,\eta_1,\eta_2\\=\pm1}}\int dp_1dp_2st[(sp_1+tp_2)^2-q^2]Z_{\eta_1}(p_1)Z_{\eta_2}(p_2)\\
&\quad\times\left[\left(\frac{t\eta_2\nu_{\bar{\eta}_2}(p_2)+s\eta_1\nu_{\eta_1}(p_1)}{s\eta_1\nu_{\eta_1}(p_1)+tV(p_2)}+\frac{s\eta_1\nu_{\bar{\eta}_1}(p_1)+t\eta_2\nu_{\eta_2}(p_2)}{t\eta_2\nu_{\eta_2}(p_2)+sV(p_1)}\right)\frac{1}{i\omega_m+i\nu_n-t\eta_2\nu_{\eta_2}(p_2)}\cdot\frac{1}{i\nu_n-s\eta_1\nu_{\eta_1}(p_1)}\right.\\
&\quad-\frac{t\eta_2 Z_{\bar{\eta}_2}(p_2)\bar{\nu}(p_2)}{i\nu_n+tV(p_2)}\cdot\frac{1}{i\omega_m+i\nu_n-t\eta_2\nu_{\eta_2}(p_2)}\cdot\frac{1}{s\eta_1\nu_{\eta_1}(p_1)+tV(p_2)}\\
&\quad\left.-\frac{s\eta_1 Z_{\bar{\eta}_1}(p_1)\bar{\nu}(p_1)}{i\omega_m+i\nu_n+sV(p_1)}\cdot\frac{1}{i\nu_n-s\eta_1\nu_{\eta_1}(p_1)}\cdot\frac{1}{t\eta_2\nu_{\eta_2}(p_2)+sV(p_1)}\right]\\
&=-\frac{5e^2}{12(2\pi)^2q}\sum_{\substack{s,t,\eta_1,\eta_2\\=\pm1}}\int dp_1dp_2st[(sp_1+tp_2)^2-q^2]Z_{\eta_1}(p_1)Z_{\eta_2}(p_2)\\
&\quad\times\left[\left(2+\frac{t\eta_2 Z_{\bar{\eta}_2}(p_2)\bar{\nu}(p_2)}{s\eta_1\nu_{\eta_1}(p_1)+tV(p_2)}+\frac{s\eta_1 Z_{\bar{\eta}_1}(p_1)\bar{\nu}(p_1)}{t\eta_2\nu_{\eta_2}(p_2)+sV(p_1)}\right)\frac{f(s\eta_1\nu_{\eta_1}(p_1))-f(t\eta_2\nu_{\eta_2}(p_2))}{i\omega_m+s\eta_1\nu_{\eta_1}(p_1)-t\eta_2\nu_{\eta_2}(p_2)}\right.\\
&\quad-\frac{t\eta_2 Z_{\bar{\eta}_2}(p_2)\bar{\nu}(p_2)}{s\eta_1\nu_{\eta_1}(p_1)+tV(p_2)}\cdot\frac{f(-tV(p_2))-f(t\eta_2\nu_{\eta_2}(p_2))}{i\omega_m-tV(p_2)-t\eta_2\nu_{\eta_2}(p_2)}
\end{aligned}
$$

$$
\left.-\frac{s\eta_1 Z_{\bar{\eta}_1}(p_1)\bar{\nu}(p_1)}{t\eta_2\nu_{\eta_2}(p_2)+sV(p_1)}\cdot\frac{f(s\eta_1\nu_{\eta_1}(p_1))-f(-sV(p_1))}{i\omega_m+s\eta_1\nu_{\eta_1}(p_1)+sV(p_1)}\right], \tag{191}
$$

where we transform the first term by $V(p)+\eta\nu_\eta(p)=\eta Z_\eta(p)\bar{\nu}(p)$ and $V(p)+\bar{\eta}\nu_{\bar{\eta}}(p)=\bar{\eta}Z_{\bar{\eta}}(p)\bar{\nu}(p)$ in the second line. Because the gauge invariant vertex Eq. (163) is proportional to $1/i\omega_m$, it seems that the final result has an infrared divergence. However, this divergence is canceled out.

From Eqs. (150), (174) and (191), $\mathrm{Im}\Pi^R_{00}$ is evaluated as

$$
\begin{aligned}
&\mathrm{Im}\Pi^R_{00}(\omega,\boldsymbol{q})\\
=&\frac{5\alpha}{16q}\sum_{\substack{s,t,\eta_1,\eta_2\\=\pm1}}\int dp_1dp_2st[(sp_1+tp_2)^2-q^2]Z_{\eta_1}(p_1)Z_{\eta_2}(p_2)\\
&\times\Bigg[\left(2+\frac{t\eta_2 Z_{\bar{\eta}_2}(p_2)\bar{\nu}(p_2)}{s\eta_1\nu_{\eta_1}(p_1)+tV(p_2)}+\frac{s\eta_1 Z_{\bar{\eta}_1}(p_1)\bar{\nu}(p_1)}{t\eta_2\nu_{\eta_2}(p_2)+sV(p_1)}\right)\\
&\quad\times[f(s\eta_1\nu_{\eta_1}(p_1))-f(t\eta_2\nu_{\eta_2}(p_2))]\delta(\omega+s\eta_1\nu_{\eta_1}(p_1)-t\eta_2\nu_{\eta_2}(p_2))\\
&\quad-\frac{t\eta_2 Z_{\bar{\eta}_2}(p_2)\bar{\nu}(p_2)}{s\eta_1\nu_{\eta_1}(p_1)+tV(p_2)}[f(-tV(p_2))-f(t\eta_2\nu_{\eta_2}(p_2))]\delta(\omega-tV(p_2)-t\eta_2\nu_{\eta_2}(p_2))\\
&\quad-\frac{s\eta_1 Z_{\bar{\eta}_1}(p_1)\bar{\nu}(p_1)}{t\eta_2\nu_{\eta_2}(p_2)+sV(p_1)}[f(s\eta_1\nu_{\eta_1}(p_1))-f(-sV(p_1))]\delta(\omega+s\eta_1\nu_{\eta_1}(p_1)+sV(p_1))\Bigg].
\end{aligned}\tag{192}
$$

Each δ-function in Eq. (192) represents the energy conservation. One can obtain the information about photon production mechanism from these conservations as will be discussed later.

Next, we analyze $\sum_i \mathrm{Im}\Pi^R_{ii}$. As in the similar manner in the case of $\mathrm{Im}\Pi^R_{00}$, we first evaluate $\sum_i \Pi_{ii}$ and then extract the imaginary part. To evaluate $\sum_i \Pi_{ii}$, we decompose the photon self energies into three parts $\Pi^{(1)}_{ii}, \Pi^{(2)}_{ii}$, $\Pi^{(3)}_{ii}$ as

$$
\Pi^{(1)}_{ii}(i\omega_m,\boldsymbol{q})=-\frac{5}{3}T\sum_n\int\frac{d^3p}{(2\pi)^3}\mathrm{Tr}_{\mathrm{D}}[S(P)\gamma_i S(P+Q)\gamma_i], \tag{193}
$$

$$
\begin{aligned}
\Pi^{(2)}_{ii}(i\omega_m,\boldsymbol{q})=&-\frac{5}{3}T\sum_n\int\frac{d^3p}{(2\pi)^3}\mathrm{Tr}_{\mathrm{D}}\Bigg[S(P)\gamma_i S(P+Q)\left(\frac{-q_i}{2q^2}\right)\\
&\times\left[S^{-1}(i\omega_m+i\nu_n,\boldsymbol{p}+\boldsymbol{q})+S^{-1}(i\nu_n,\boldsymbol{p}+\boldsymbol{q})-S^{-1}(i\omega_m+i\nu_n,\boldsymbol{p})-S^{-1}(i\nu_n,\boldsymbol{p})\right]\Bigg],
\end{aligned}\tag{194}
$$

$$
\Pi^{(3)}_{ii}(i\omega_m,\boldsymbol{q})=-\frac{5}{3}T\sum_n\int\frac{d^3p}{(2\pi)^3}\mathrm{Tr}_{\mathrm{D}}\left[S(P)\gamma_i S(P+Q)\left(\frac{-q_i(\boldsymbol{q}\cdot\boldsymbol{\gamma})}{q^2}\right)\right], \tag{195}
$$

where $\Pi_{ii}(Q)=\Pi^{(1)}_{ii}(Q)+\Pi^{(2)}_{ii}(Q)+\Pi^{(3)}_{ii}(Q)$. We calculate them separately. We have already treated

$\sum_i \Pi_{ii}^{(1)}$ in Section 4.3. It is given by

$$\sum_{i=1}^{3}\mathrm{Im}\Pi_{ii}^{(1),R}(\omega,\boldsymbol{q}) = -\frac{5\alpha}{3q}\sum_{\substack{s,t,\eta_1,\eta_2\\=\pm1}}\int dp_1dp_2Z_{\eta_1}(p_1)Z_{\eta_2}(p_2)\left[\frac{st(sp_1+tp_2)^2-q^2}{2}-4p_1p_2\right]$$
$$\times[f(s\eta_1\nu_{\eta_1}(p_1))-f(t\eta_2\nu_{\eta_2}(p_2))]\delta(\omega+s\eta_1\nu_{\eta_1}(p_1)-t\eta_2\nu_{\eta_2}(p_2)). \quad (196)$$

Let us consider $\Pi_{ii}^{(2)}$ next. As in the similar manner for $\mathrm{Im}\Pi_{00}^{R}$, one can evaluate $\mathrm{Im}\sum_i\Pi_{ii}^{(2),R}$ by the following procedure,

$$\begin{aligned}
&T\sum_n \mathrm{Tr_D}[S(P)\gamma_i S(P+Q)[S^{-1}(i\omega_m+i\nu_n,\boldsymbol{p}+\boldsymbol{q})+S^{-1}(i\omega_m,\boldsymbol{p}+\boldsymbol{q})-S^{-1}(i\omega_m+i\nu_n,\boldsymbol{p})-S^{-1}(i\nu_n,\boldsymbol{p})]]\\
=&T\sum_n \mathrm{Tr_D}[\Lambda_s(\boldsymbol{p}_1)\gamma_0\gamma_i\Lambda_t(\boldsymbol{p}_2)]\\
&\times\left[S_s(i\nu_n,p_1)\left[1+\frac{S_t(i\omega_m+i\nu_n,p_2)}{S_t(i\nu_n,p_2)}\right]-S_t(i\omega_m+i\nu_n,p_2)\left[1+\frac{S_s(i\nu_n,p_1)}{S_s(i\omega_m+i\nu_n,p_1)}\right]\right]\\
=&T\sum_n \mathrm{Tr_D}[\Lambda_s(\boldsymbol{p}_1)\gamma_0\gamma_i\Lambda_t(\boldsymbol{p}_2)]\\
&\times\left[S_s(i\nu_n,p_1)\left[\frac{S_t(i\omega_m+i\nu_n,p_2)}{S_t(i\nu_n,p_2)}-1\right]-S_t(i\omega_m+i\nu_n,p_2)\left[\frac{S_s(i\nu_n,p_1)}{S_s(i\omega_m+i\nu_n,p_1)}-1\right]\right], \quad (197)
\end{aligned}$$

where the final approximation is justified when we focus on the imaginary part and substitute the quark propagator obtained with the two-pole ansatz Eq. (158) into $S_{s,t}$ because the imaginary part of $T\sum_n S_{s,t}$ equals to zero with two-pole approximation and one can add or subtract $S_{s,t}$ arbitrary. $\sum_i \mathrm{Im}\Pi_{ii}^{(2),R}$ is calculated as

$$\begin{aligned}
&\sum_{i=1}^{3}\mathrm{Im}\Pi_{ii}^{(2),R}(\omega,\boldsymbol{q})\\
=&\frac{5\alpha}{16q}\sum_{\substack{s,t,\eta_1,\eta_2\\=\pm1}}\int dp_1dp_2 st\omega\frac{tp_2-sp_1}{q^2}[(sp_1+tp_2)^2-q^2]Z_{\eta_1}(p_1)Z_{\eta_2}(p_2)\\
&\times\Bigg[\left(2+\frac{t\eta_2Z_{\bar{\eta}_2}(p_2)\bar{\nu}(p_2)}{s\eta_1\nu_{\eta_1}(p_1)+tV(p_2)}+\frac{s\eta_1Z_{\bar{\eta}_1}(p_1)\bar{\nu}(p_1)}{t\eta_2\nu_{\eta_2}(p_2)+sV(p_1)}\right)\\
&\quad\times[f(s\eta_1\nu_{\eta_1}(p_1))-f(t\eta_2\nu_{\eta_2}(p_2))]\delta(\omega+s\eta_1\nu_{\eta_1}(p_1)-t\eta_2\nu_{\eta_2}(p_2))\\
&\quad-\frac{t\eta_2Z_{\bar{\eta}_2}(p_2)\bar{\nu}(p_2)}{s\eta_1\nu_{\eta_1}(p_1)+tV(p_2)}[f(-tV(p_2))-f(t\eta_2\nu_{\eta_2}(p_2))]\delta(\omega-tV(p_2)-t\eta_2\nu_{\eta_2}(p_2))\\
&\quad-\frac{s\eta_1Z_{\bar{\eta}_1}(p_1)\bar{\nu}(p_1)}{t\eta_2\nu_{\eta_2}(p_2)+sV(p_1)}[f(s\eta_1\nu_{\eta_1}(p_1))-f(-sV(p_1))]\delta(\omega+s\eta_1\nu_{\eta_1}(p_1)+sV(p_1))\Bigg]. \quad (198)
\end{aligned}$$

It has a similar structure to $\mathrm{Im}\Pi_{00}^{R}$ Eq. (192). Compared to $\mathrm{Im}\Pi_{00}^{R}$, the integrand in Eq. (198) has an extra factor $\omega(tp_2-sp_1)/q^2$.

Now let us consider the last part $\Pi_{ii}^{(3)}$. From Eq. (181), the imaginary part of the retarded photon self energy $\sum_i \mathrm{Im}\Pi_{ii}^{(3),R}$ is expressed as

$$\begin{aligned}
&\sum_i \mathrm{Im}\Pi_{ii}^{(3),R} \\
=&\frac{5\alpha}{3q}\sum_{\substack{s,t,\eta_1,\eta_2\\=\pm 1}}\int dp_1 dp_2 p_1 p_2 \left[1-\frac{st}{2p_1p_2}\left[(p_1^2+p_2^2-q^2)+\frac{(p_1^2-p_2^2)^2-q^4}{q^2}\right]\right] Z_{\eta_1}(p_1)Z_{\eta_2}(p_2) \\
&\times[f(s\eta_1\nu_{\eta_1}(p_1))-f(t\eta_2\nu_{\eta_2}(p_2))]\delta(\omega+s\eta_1\nu_{\eta_1}(p_1)-t\eta_2\nu_{\eta_2}(p_2)). \qquad (199)
\end{aligned}$$

Finally, from Eqs. (192), (196), (198) and (199), we obtain the trace of the imaginary part of the photon self energy constructed with the lattice quark propagator [19–21] and the gauge invariant vertex Eqs. (163) and (164),

$$\begin{aligned}
&\mathrm{Im}\Pi_{\mu}^{R,\mu}(\omega,\boldsymbol{q}) \\
=&-\frac{5\alpha}{12q}\sum_{\substack{s,t,\eta_1,\eta_2\\=\pm 1}}\int dp_1 dp_2 Z_{\eta_1}(p_1)Z_{\eta_2}(p_2)\left[-st[(sp_1+tp_2)^2-q^2]\left(1-\frac{\omega(tp_2-sp_1)}{q^2}\right)\right. \\
&\times\left[-\frac{t\eta_2 Z_{\bar{\eta}_2}(p_2)\bar{\nu}(p_2)}{s\eta_1\nu_{\eta_1}(p_1)+tV(p_2)}[f(-tV(p_2))-f(t\eta_2\nu_{\eta_2}(p_2))]\delta(\omega-tV(p_2)-t\eta_2\nu_{\eta_2}(p_2))\right. \\
&\quad\left.-\frac{s\eta_1 Z_{\bar{\eta}_1}(p_1)\bar{\nu}(p_1)}{t\eta_2\nu_{\eta_2}(p_2)+sV(p_1)}[f(s\eta_1\nu_{\eta_1}(p_1))-f(-sV(p_1))]\delta(\omega+s\eta_1\nu_{\eta_1}(p_1)+sV(p_1))\right] \\
&\quad+\left[-st[(sp_1+tp_2)^2-q^2]\left(1-\frac{\omega(tp_2-sp_1)}{q^2}\right)\left(2+\frac{t\eta_2 Z_{\bar{\eta}_2}(p_2)\bar{\nu}(p_2)}{s\eta_1\nu_{\eta_1}(p_1)+tV(p_2)}+\frac{s\eta_1 Z_{\bar{\eta}_1}(p_1)\bar{\nu}(p_1)}{t\eta_2\nu_{\eta_2}(p_2)+sV(p_1)}\right)\right. \\
&\quad\left.+12p_1p_2-2st[(sp_1+tp_2)^2-q^2]+2st\left[(p_1^2+p_2^2-q^2)-\frac{(p_1^2-p_2^2)^2-q^4}{q^2}\right]\right] \\
&\quad\left.\times[f(s\eta_1\nu_{\eta_1}(p_1))-f(t\eta_2\nu_{\eta_2}(p_2))]\delta(\omega+s\eta_1\nu_{\eta_1}(p_1)-t\eta_2\nu_{\eta_2}(p_2))\right]. \qquad (200)
\end{aligned}$$

One obtains a non-perturbative thermal photon production rate by multiplying Eq. (200) by the factor $-b(\omega)/(2\pi)^3$ with the Bose distribution function $b(\omega)=1/(\mathrm{e}^{\beta\omega}-1)$. Let us inspect the physical meaning of each term in Eq. (200). As discussed in Section 4.3, the third term in Eq. (200) corresponds to contributions from pair annihilation and Landau damping. Compared to Eq. (185), thermal coefficient and δ-function are shared but the coefficient becomes more complicated owing to the vertex correction. The first and second terms in Eq. (200) seem to be photon emissions (or absorption) via pair annihilation or Landau damping where quasi-particles have energies ν_η and V. However, thermal excited states of quarks does not have the dispersion $\nu=V(p)=Z_+(p)\nu_-(p)-Z_-(p)\nu_+(p)$. Therefore, the photon productions expressed in the first and second terms in Eq. (200) cannot be interpreted via simple reactions between quasi-particles and the photon. The origin of these odd photon productions is the anomalous pole included in S_s^{-1} in Eqs. (163) and (164). When one evaluates the Matsubara sum of the photon self energy constructed with the lattice quark propagator and our vertex, one has to estimate both contributions from poles of the lattice quark propagator and the anomalous pole which is included in Γ_μ. One finds that the argument of the δ-function of the first term in Eq. (200) depends only on p_2. Similarly, the argument of the second δ-function depends only on p_1. It means that integrals on the (p_1, p_2) plane of these terms become one dimensional integrals.

We reveal that anomalous photon emissions expressed in the first and second terms in Eq. (200) appear when we evaluate the photon self energy with the vertex Γ_μ. At diagram level, all gluon exchange between two quarks are taken in the diagram shown in Fig. 19. These gluon exchanges are expressed in the full photon-quark vertex. It implies that anomalous photon productions in Eq. (200) can be considered as a total contribution from all gluon exchange diagrams.

Next, let us consider a thermal dilepton production rate. When the full vertex function satisfying the WTI is used in Eq. (151), the temporal component Π_{00} for $\boldsymbol{q}=0$ vanishes. One can easily check this explicitly by substituting Eq. (163) into Eq. (151). For $\sum_{i=1}^{3}\Pi_{ii}$, from Eqs. (149),(151) and (169), one has

$$\sum_i \Pi_{ii}(i\omega_m,0)=\frac{10e^2}{3}T\sum_n\int\frac{d^3p}{(2\pi)^3}\sum_{s=\pm}sS_s(i\nu_n,p)\left\{\frac{\partial\ln S_s^{-1}(i\nu_n+i\omega_m,p)}{\partial p}-\frac{1}{p}\left(1-\frac{S_{-s}(i\nu_n+i\omega_m,p)}{S_s(i\nu_n+i\omega_m,p)}\right)\right\},\tag{201}$$

where to obtain the first term we used

$$S_s(i\nu_n,p)\frac{\partial S_s^{-1}(i\nu_n,p)}{\partial p}=\frac{\partial\ln S_s^{-1}(i\nu_n,p)}{\partial p}.\tag{202}$$

With the lattice quark propagator, the term including $\partial\ln S_s^{-1}/\partial p$ in Eq. (201) is then calculated to be

$$\begin{aligned}
&T\sum_n sS_s(i\nu_n,p)\frac{\partial\ln S_s^{-1}(i\nu_n+i\omega_m,\boldsymbol{p})}{\partial p}\\
&=-T\sum_n\left(\frac{Z_+}{i\nu_n-s\nu_+}+\frac{Z_-}{i\nu_n+s\nu_-}\right)\left(\frac{d\nu_+/dp}{i\nu_n+i\omega_m-s\nu_+}-\frac{d\nu_-/dp}{i\nu_n+i\omega_m+s\nu_-}+\frac{dV/dp}{i\nu_n+i\omega_m+sV}\right)\\
&=-\left(\frac{Z_+d\nu_-/dp}{i\omega_m+s\nu_++s\nu_-}+\frac{Z_-d\nu_+/dp}{i\omega_m-s\nu_+-s\nu_-}\right)(f(s\nu_+)+f(s\nu_-)-1)\\
&\quad+\frac{Z_+dV/dp}{i\omega_m+s\nu_++sV}(f(s\nu_+)-f(-sV))+\frac{Z_-dV/dp}{i\omega_m-s\nu_-+sV}(f(s\nu_-)-f(-sV)),
\end{aligned}\tag{203}$$

where the Matsubara sum over n is taken in the last equality and each argument of functions is p.

The remaining part of Eq. (201) is calculated as follows:

$$\begin{aligned}
&T\sum_n sS_s(i\nu_n,p)\left(1-\frac{S_{-s}(i\nu_n+i\omega_m,p)}{S_s(i\nu_n+i\omega_m,p)}\right)\frac{1}{p}\\
&=T\sum_n\left(\frac{Z_+}{i\nu_n-s\nu_+}+\frac{Z_-}{i\nu_n+s\nu_-}\right)\left(\frac{F_1}{i\nu_n+i\omega_m+sV}+\frac{F_2}{i\nu_n+i\omega_m+s\nu_+}+\frac{F_3}{i\nu_n+i\omega_m-s\nu_-}\right)
\end{aligned}\tag{204}$$

$$
\begin{aligned}
=&\frac{Z_+F_1}{i\omega_m+s\nu_++sV}\left(f(-sV)-f(s\nu_+)\right)+\frac{Z_-F_1}{i\omega_m-s\nu_-+sV}\left(f(-sV)-f(-s\nu_-)\right)\\
&+\frac{Z_+F_2}{i\omega_m+2s\nu_+}\left(f(-s\nu_+)-f(s\nu_+)\right)+\frac{Z_-F_2}{i\omega_m+s\nu_+-s\nu_-}\left(f(-s\nu_+)-f(-s\nu_-)\right)\\
&+\frac{Z_+F_3}{i\omega_m+s\nu_+-s\nu_-}\left(f(s\nu_-)-f(s\nu_+)\right)+\frac{Z_-F_3}{i\omega_m-2s\nu_-}\left(f(s\nu_-)-f(-s\nu_-)\right),
\end{aligned}
\tag{205}
$$

where

$$
\begin{aligned}
F_1&=-\frac{2E(\nu_--V)(\nu_++V)}{p(\nu_-+V)(\nu_+-V)},\\
F_2&=\frac{2\nu_+(\nu_++V)(\nu_+-\nu_-)}{p(\nu_+-V)(\nu_++\nu_-)},\\
F_3&=\frac{2\nu_-(\nu_+-\nu_-)(\nu_--V)}{p(\nu_++\nu_-)(\nu_-+V)},
\end{aligned}
$$

and each argument of functions is p.

Combining these results and taking the analytic continuation, the thermal dilepton production rate with $\boldsymbol{q}=\mathbf{0}$ is given by

$$
\begin{aligned}
&\left.\frac{dN^{l^+l^-}}{d\omega d^3q d^4x}\right|_{\boldsymbol{q}=\mathbf{0}}\\
=&-\frac{5\alpha^2}{9\pi^4}\frac{1}{\omega^2}\frac{1}{\mathrm{e}^{\beta\omega}-1}\int_0^\infty dp p^2\Bigg[-\frac{2(\nu_+-\nu_-)}{p}\Bigg[Z_+Z_-\frac{V(\nu_+-\nu_-)+2\nu_+\nu_-}{(\nu_+-V)(\nu_-+V)}[f(\nu_-)-f(\nu_+)]\\
&\times\delta(\omega-\nu_++\nu_-)+\frac{Z_-^2\nu_-}{\nu_-+V}[1-2f(\nu_-)]\delta(\omega-2\nu_-)+\frac{Z_+^2\nu_+}{\nu_+-V}[1-2f(\nu_+)]\delta(\omega-2\nu_+)\Bigg]\\
&+\left[Z_+\frac{d\nu_-}{dp}-Z_-\frac{d\nu_+}{dp}\right][1-f(\nu_+)-f(\nu_-)]\delta(\omega-\nu_+-\nu_-)-\left[\frac{2Z_+Z_-V\bar{\nu}^2}{p(\nu_+-V)(\nu_-+V)}+\frac{dV}{dp}\right]\\
&\times[Z_+[1-f(V)-f(\nu_+)]\delta(\omega-\nu_+-V)+Z_-[f(V)-f(\nu_-)]\delta(\omega-\nu_-+V)]\Bigg],
\end{aligned}
\tag{206}
$$

where each argument of the function is p. One finds that each contribution of the anomalous radiation becomes finite owing to the stronger constraint. Because the gauge invariant vertex Eq. (169) is the partial derivative of the lattice quark propagator which is obtained with the two-pole approximation, derivatives of dispersions and $V(p)$ appear in the formula Eq. (206). In Section 5.2, we show the numerical analysis of the dilepton production rate in the case of $\boldsymbol{q}=\mathbf{0}$. We will discuss a qualitative change of the obtained spectrum caused by the vertex correction.

5 Numerical Result

We obtained formalism of non-perturbative production rates of photons and dileptons in the previous section. Our goal is analyzing these thermal production rates non-perturbatively. In this section, we show numerical results of production rates. We also discuss effects on each rate arisen from the peculiar structure of the plasmino mode and our vertex correction. First, we show the numerical result of thermal photons and discuss about the structure of the obtained spectral. After that, we consider the numerical result of thermal dileptons.

5.1 Numerical Result of Non-Perturbative Photon Production Rate

In this subsection, we consider the numerical result of non-perturbative photon production rate from Eq. (200). We explain details of the spectral structure related to the kinematics and dispersions of quasi-particles.

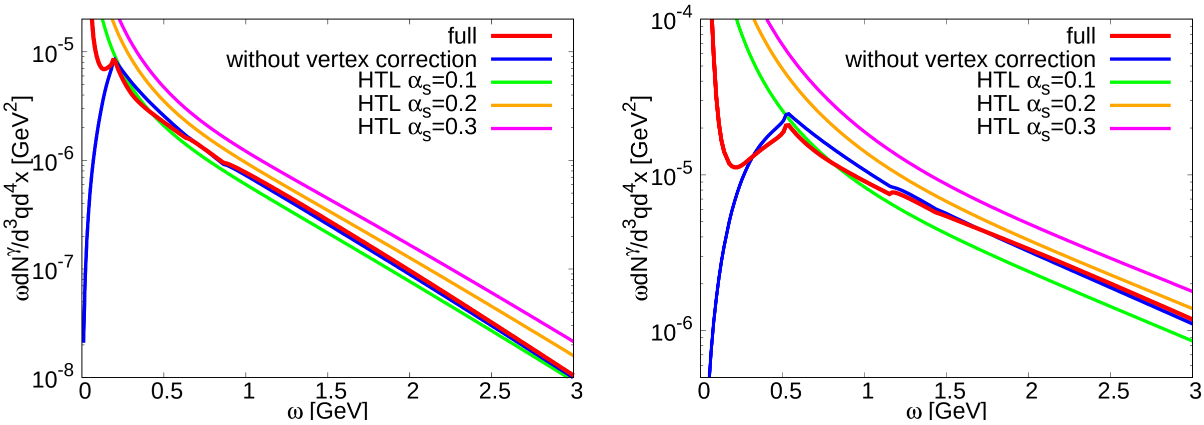

(a) $T = 1.5T_{\mathrm{c}}$

(b) $T = 3T_{\mathrm{c}}$

Figure 25: Thermal photon production rate at $T = 1.5T_{\mathrm{c}}$ (left panel) and $3T_{\mathrm{c}}$ (right panel) illustrated with perturbative results [64] and the no vertex correction result Eq. (185).

In Fig. 25, we show the numerical result of the thermal photon production rate obtained from Eq. (200) at $T = 1.5T_{\mathrm{c}}$ (Fig. 25(a)) and $T = 3T_{\mathrm{c}}$ (Fig. 25(b)) with perturbative results [64] of several α_s and the production rate analyzed with the bare vertex Eq. (185). Several comments on the numerical analysis are in order. First, in Fig. 25(a), we cut the full production rate at very soft region $\omega < 50$MeV where the numerical calculation becomes unstable. This cut is reasonable because we are interested in photons with $\mathscr{O}$(GeV) momentum and such very soft photons cannot be detected in HIC. Second, the numerical calculation without vertex correction is stable even in small energy region. Finally, in Fig. 25(a), we draw perturbative lines during $0.09\mathrm{GeV} < \omega < 3\mathrm{GeV}$ where the phenomenological fitting Eqs. (143), (144) and (145) well reproduce the leading order perturbative result [64]. In the case of $T = 3T_{\mathrm{c}}$, we cut the production rate below 60MeV and phenomenological fitting lines start at

$\omega = 0.18$GeV.

In the region where 1GeV $< \omega <$ 3GeV, the full result and the bare vertex result have similar tendency to perturbative results. They have the almost same slopes and comparable production rates. It is a casual coincidence for values of production rates. However, the reason why each spectral has the almost same slope is that slopes are governed by the overall thermal factor, $1/e^{\beta\omega}-1$ in Eq. (148), both in non-perturbative case and in the perturbative analysis. In Fig. 26, we illustrate production rates divided by the Bose distribution function for two temperatures. It is $-\mathrm{Im}\Pi_{\mu}^{R,\mu}/(2\pi)^3$ itself. It seems to be odd that $\mathrm{Im}\Pi_{\mu}^{R,\mu}$ does not damp with the photon energy increased. However, this behavior is not counterintuitive. Let us explain the behavior of $\mathrm{Im}\Pi_{\mu}^{R,\mu}$. First, remember that the imaginary part of the retarded photon self energy is related to the "difference" between the photon absorption and the photon production from the hot medium. In addition, the retarded photon self energy is calculated based on the finite temperature field theory, and thus we implicitly assume that the static medium has an infinite volume. Owing to the size of the hot matter, photons with higher momenta are emitted to some extent and they are absorbed by the medium. One finds that photon production and absorption are occurred even in the higher energy region $\omega \gg T$. Therefore, the value of $\mathrm{Im}\Pi_{\mu}^{R,\mu}$ does not become small even in the higher energy region.

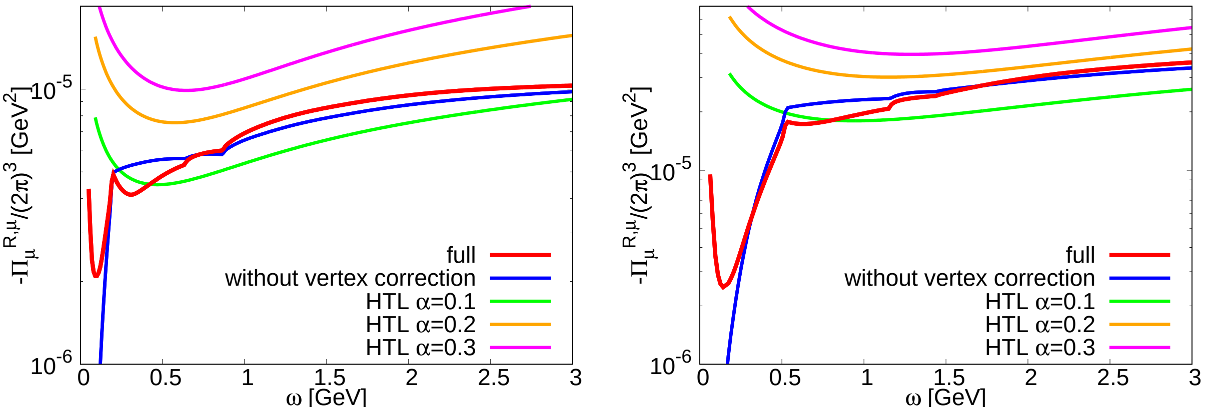

(a) $T = 1.5T_c$

(b) $T = 3T_c$

Figure 26: Production rates divided by the Bose distribution function at $T = 1.5T_c$ (left panel) and $T = 3T_c$ (right panel).

We reveal the reason why $\mathrm{Im}\Pi_{\mu}^{R,\mu}$ has finite value in the region $\omega \gg T$. However, one may guess that when the static medium fulfills the whole space, produced thermal photons are not able to penetrate the matter even at the leading order calculation of α, and thus net photon production rate should become zero. To avoid this problem, let suppose a strange situation that an observer observes the infinite size thermal medium from the outside. In this case, the observer detects photons emitted from the surface of the medium. More accurately, photons radiated from near the surface where a depth from the surface is comparable to the photon mean free path can be detected by the observer. The thermal real photon production rate Eq. (148) can be considered as the photon radiation from the surface of the hot matter. Finally, we comment on an application for heavy ion collisions. In the future, we intend to apply our result to estimate the photon production "yield" from the quark gluon plasma. It is considered that sizes of deconfined media produced in heavy ion collisions are smaller that the photon mean free path. Therefore, it is reasonable to substitute the photon production rate from near surface of the infinite size deconfined medium for the photon emission rate of the tiny local thermal equilibrium deconfined medium.

Now, we return to slops of obtained spectra. One finds that the imaginary part of the retarded photon self energy is not suppressed when the photon energy becomes large both in our analysis and in the perturbative analysis. Only the Bose distribution function is the factor to suppress the photon radiation. Therefore, our result and perturbative results share the similar slope.

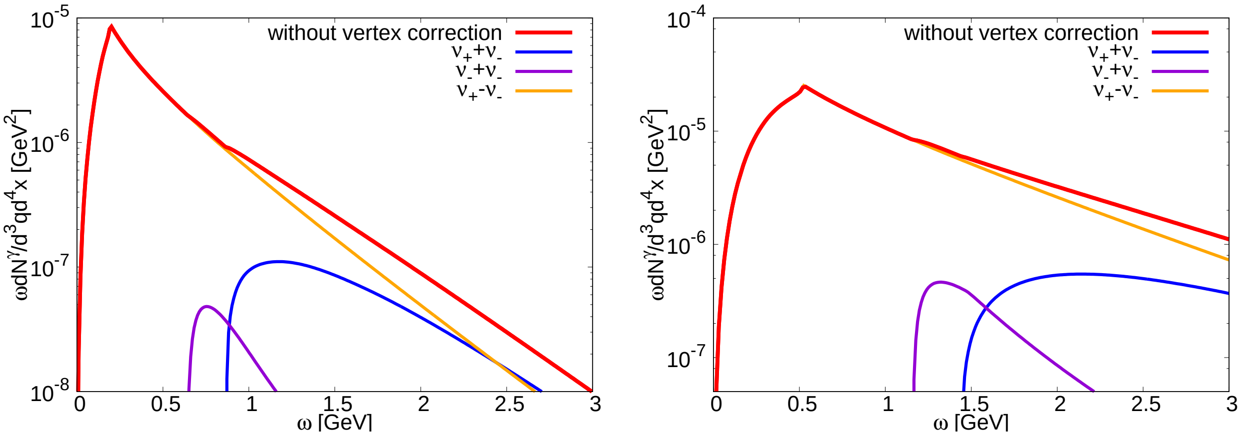

(a) $T = 1.5T_{\mathrm{c}}$

(b) $T = 3T_{\mathrm{c}}$

Figure 27: Decomposition of photon production rates obtained from the lattice quark propagator and the bare vertex at $T = 1.5T_{\mathrm{c}}$ (left panel) and $T = 3T_{\mathrm{c}}$ (right panel).

Next, let us consider contributions from several reactions separately. Before we discuss the full result, we first consider the decomposition of the rate obtained with the lattice quark propagator and the bare vertex. It will help us to understand effects of our vertex correction. In Fig. 27, we illustrate the contribution of each term in Eq. (185) with the production rate evaluated with the lattice quark propagator and the bare vertex. Although four energy conservation $\omega = \nu_- \pm \nu_-$, $\nu_+ \pm \nu_-$ are possible but the contribution of $\nu_- - \nu_-$ is not shown in Fig. 27. Compared to the total rate, the radiation from $nu_- - \nu_-$ is smaller by five order of magnitude. This behavior of $\nu_- - \nu_-$ process is preferable. The photon emission via $nu_- - \nu_-$ can be interpreted as "Cherenkov" radiation. Cherenkov radiation is a phenomenon that the thermal excited particle emits the photon when it propagates in the medium beyond the speed of light. Recall the dispersion of the lattice quark propagator [19–21] which we discussed in Section 4.1.1. The dispersion of the plasmino mode exists even in space-like region, it exceeds unity for $p \gtrsim 3m_{\mathrm{T}}$ and it acausal. The Cherenkov radiation is arisen from the acausal structure of the plasmino dispersion. Owing to the acausality, this Cherenkov process is unphysical

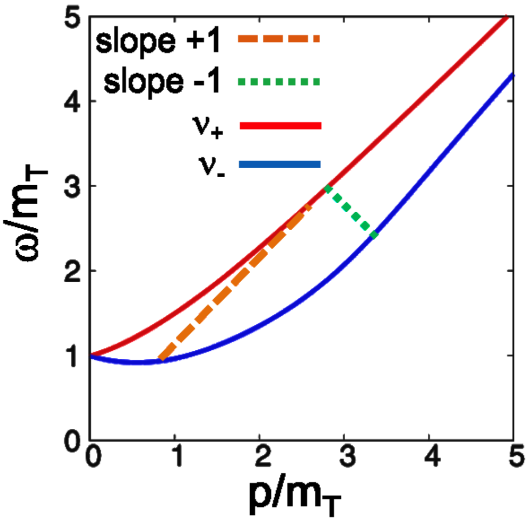

Figure 28: Dispersions of quasi-particles are shown with lines of slopes ±1 which connect two dispersions.

and expected to be forbidden. However, for our analysis which uses the lattice dispersion as the input, this acausal Cherenkov radiation is essentially unavoidable. Based on the two-pole ansatz model, the $\nu_- - \nu_-$ Landau damping channel has the intensity. However, as already mentioned, the contribution of the Cherenkov effect is extremely smaller than other processes. Therefore, this unphysical emission is negligible.

Now, let us discuss other three processes. From Fig. 27, one finds that pair annihilation processes have thresholds though the Landau damping between normal and plasmino quasi-particles arises at the origin. As we discussed in Section 4.3, thresholds are determined via the kinematics and dispersions of quasi-particles. The threshold of the normal and plasmino pair annihilation is estimated as 0.87GeV for $T = 1.5T_\mathrm{c}$ and 1.43GeV for $T = 3T_\mathrm{c}$. Another threshold of the pair annihilation is evaluated about 0.64GeV for $T = 1.5T_\mathrm{c}$ and 1.16GeV for $T = 3T_\mathrm{c}$. At these threshold, the total production rate changes non-smoothly. With the increasing of the photon energy, these channels open and construct the non-smooth structure.

It should be emphasized that a cusp which is located around 0.19GeV for $T = 1.5T_\mathrm{c}$ and 0.53GeV for $T = 3T_\mathrm{c}$ is not arisen from the opening pair annihilation channel. Its origin is the kinematics of the Landau damping between normal and plasmino quasi-particles. Let us study the contribution of the Landau damping $\nu_+ - \nu_-$ which dominates the total photon production rate. The positional relation on the dispersion of initial and final state quasi-particles can be illustrated as shown in Fig. 28. Owing to the constraint of the on-shell condition, the initial point and the final point are tied with lines whose slopes equal to ±1. The height between two points corresponds to the energy of the produced photon and the more height becomes longer, the length of the line becomes longer. From Fig. 28, one finds that the length of the line which has the positive slope can continue to be large. On the other hand, the length of the line with the negative slope has the upper limit. Kinematically, this means that the photon production where the three-dimensional momentum of the plasmino quasi-particle is larger than the one of the initial state quasi-particle is gradually forbidden with the emitted photon energy increased. The cusp observed in Fig. 27 corresponds to the energy where the photon production satisfying $p_{\text{final}} - p_{\text{initial}} = q$ starts to be limited. Here, we define p_{initial} and $p_{\text{final}} = q$ as the absolute value of the initial state quasi-particle and the final state quasi-particle, respectively.

We finds that the Landau damping between normal and plasmino quasi-particles has the largest contribution and the total spectrum has the peculiar structure which is caused by the lattice quark dispersion and the kinematics among quasi-particles. In the rest of this subsection, we consider the full result. Even the vertex correction gives anomalous photon production processes, it also changes each contribution. However, the vertex correction does not alter the dynamics of pair annihilation and Landau damping. Therefore, positions of the cusp and thresholds are invariant. We discuss the full result from the next paragraph.

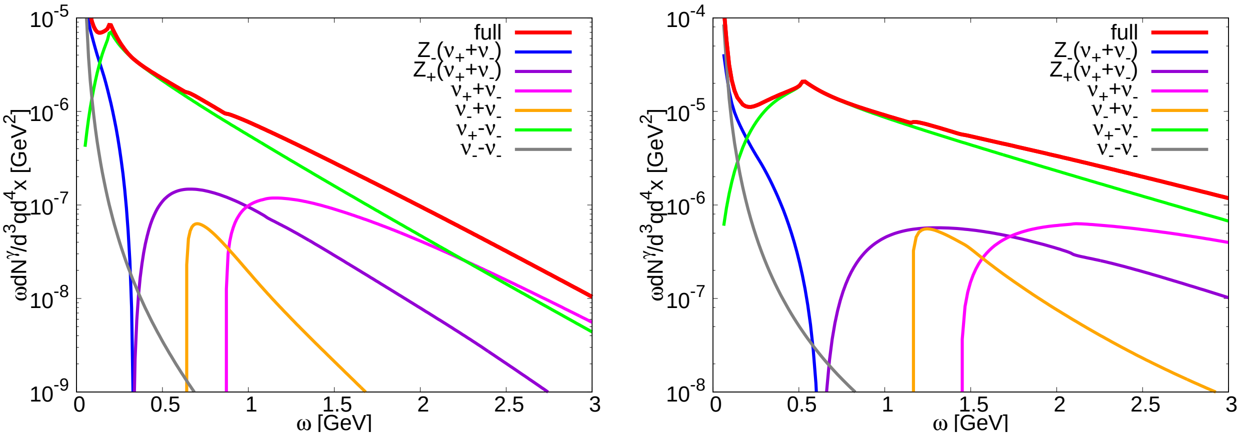

(a) $T = 1.5T_{\text{c}}$

(b) $T = 3T_{\text{c}}$

Figure 29: Decomposition of full photon production rates at $T = 1.5T_{\text{c}}$ (left panel) and $T = 3T_{\text{c}}$ (right panel).

In Fig. 29, we show the contribution of each term in Eq. (200). Compared to the bare vertex result, one finds that additional photon productions arisen owing to the anomalous pole. These anomalous photon radiations obey energy conservation $\omega = Z_+(\nu_+ + \nu_-) = \nu_+ + V$ and $\omega = Z_-(\nu_+ + \nu_-) = \nu_- - V$. $Z_+(\nu_+ + \nu_-)$ is the monotonic increase function and $Z_-(\nu_+ + \nu_-)$ is the monotonic decrease function. $Z_+(0)(\nu_+(0) + \nu_-(0)) \simeq Z_-(0)(\nu_+(0) + \nu_-(0))$. We define a threshold energy $\omega_{\text{A}} = Z_+(0)(\nu_+(0) + \nu_-(0))$. Where the energy of photon is smaller than ω_{A}, the anomalous photon production respecting $\omega = Z_-(\nu_+ + \nu_-)$ is occurred. On the other hand, anomalous photons with energies higher than ω_{A} are radiated via another anomalous reaction which satisfies $\omega = Z_+(\nu_+ + \nu_-)$. ω_{A} is approximated about 0.33GeV at $T = 1.5T_{\text{c}}$ and 0.63GeV at $T = 3T_{\text{c}}$. The anomalous photon production where $\omega < \omega_{\text{A}}$ has an infrared divergence. Let us check a mechanism how the divergence appears. Consider the term proportional to $\delta(\omega - tV(p_2) - t\eta_2 v_{\eta_2}(p_2))$ in Eq. (200) with $s = t = \eta_1 = \eta_2 = -1$. In this case, $1/s\eta_1 v_{\eta_1}(p_1) + tV(p_2)$ becomes $1/\omega$ in order to respect the energy conservation. Therefore, the contribution from this anomalous radiation diverges in $\omega \to 0$ limit. However, we emphasize that photons cannot be observed until such lower energy region. It is expected that the infrared behavior does not make fatal problem when one evaluates the photon production yield.

Another effect of our vertex correction is modification of each contribution. An outstanding change is that the unphysical Cherenkov radiation contribution gets a divergence near $\omega = 0$. Owing to the vertex correction, the integrand corresponding to the Cherenkov radiation in Eq. (200) gets the divergence. The divergence of the integrand reflects on the Cherenkov radiation rate. However, the divergence is located at the very soft energy region where photons cannot be detected in experiments. Therefore, it is expected that this divergence does not make a serious problem when one estimate the photon production yield. Other pair annihilation and Landau damping processes contributions are also altered by the vertex correction but the dominance contribution is still the Landau damping production between normal and plasmino quasi-particles. We emphasize that the change of the total rate change is not so large and the full result shows almost comparable rate to perturbative results of $\alpha_s = 0.1 \sim 0.2$. This result implies an existence of other photon source. We consider the necessity of other photon production mechanism in Section 6.

5.2 Numerical Result of Non-Perturbative Dilepton Production Rate

Next, let us consider the numerical result of the non-perturbative dilepton production rate obtained from Eq. (206). As in the case of the photon production rate, our vertex correction introduces the anomalous production. In contrast, the anomalous dilepton makes an essential role to lead to an qualitative variation of the dilepton rate. We check several effects of the dispersion structure and the vertex correction on the spectrum in this subsection.

In Fig. 30, we show the numerical result of the dilepton production rate Eq. (206) with results obtained by the HTL method [67] for two temperatures. We also plot spectra obtained without the vertex correction Eq. (189) and with the free quark gas model Eq. (176) in Fig. 30. The value of the thermal mass m_T is taken from the result obtained on the lattice [21].

In Figs. 30(a) and 30(b), one finds that the production rate with the lattice quark propagators has divergences at two energies, $\omega/m_\mathrm{T} = \omega_1/m_\mathrm{T} \simeq 1.1$ and $\omega/m_\mathrm{T} = \omega_2/m_\mathrm{T} \simeq 1.8$ for $T = 1.5T_\mathrm{c}$ and $\omega/m_\mathrm{T} = \omega_1/m_\mathrm{T} \simeq 1.6$ and $\omega/m_\mathrm{T} = \omega_2/m_\mathrm{T} \simeq 1.7$ for $T = 3T_\mathrm{c}$. For $\omega < \omega_1$, our result, as a whole, behaves similarly to the HTL one [67], i.e. it increases as ω decreases, although our production rate is smaller than the perturbative one for small ω. Near ω_1, however, it shows a prominent enhancement and exceeds the latter. We explain the detail of the enhancement later. The rate has non-smooth variation at $\omega = \omega_1$, and is significantly suppressed compared with Eq. (176) for $\omega_1 < \omega < \omega_2$. The rate has another non-smooth variation point at $\omega = \omega_2$, above which the rate is close to the free

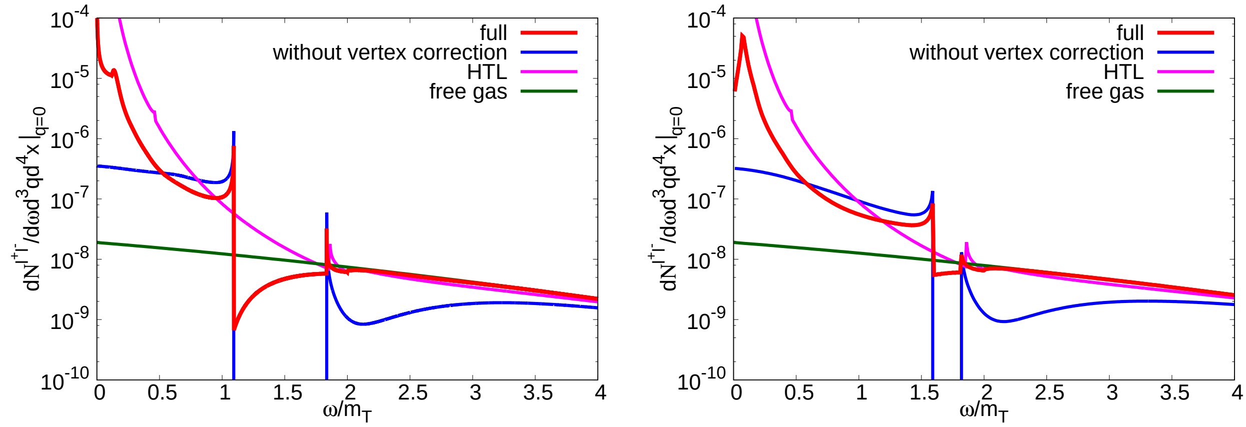

(a) $T = 1.5T_\mathrm{c}$ (b) $T = 3T_\mathrm{c}$

Figure 30: Dilepton production rates at zero momentum for $T = 1.5T_\mathrm{c}$ (left panel) and $3T_\mathrm{c}$ (right panel). Results without vertex correction are also plotted. Thin lines show perturbative results and free quark gas results.

quark one. In the dilepton rate without vertex correction, one also finds two non-smooth variations at $\omega = \omega_1$ and ω_2, while the rate vanishes for $\omega_1 < \omega < \omega_2$. One also finds that the rate takes a finite value at $\omega = 0$ for $T = 3T_\mathrm{c}$, while it diverges for $T = 1.5T_\mathrm{c}$. This limiting behavior may depend on the way of the extrapolation of $\nu_\pm(p)$ to large momentum.

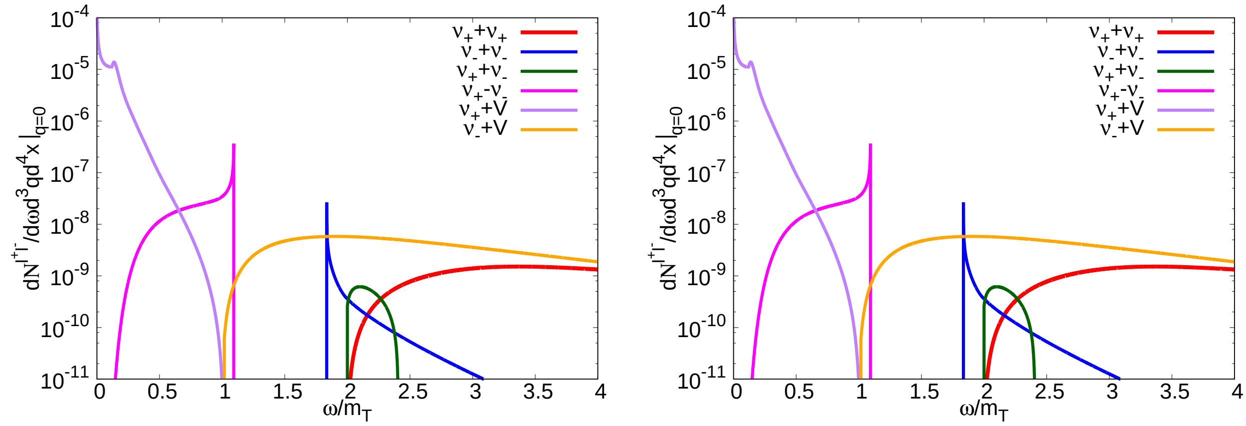

(a) $T = 1.5T_\mathrm{c}$ (b) $T = 3T_\mathrm{c}$

Figure 31: Decomposition of dilepton production rates for $T = 1.5T_\mathrm{c}$ (left panel) and $3T_\mathrm{c}$ (right panel).

In order to understand these results in more detail, we show the contribution of each term in Eq. (206) separately in Fig. 31. In the figure, the rate coming from the pair annihilation of two normal modes ($\nu_+ + \nu_+$), two plasmino modes ($\nu_- + \nu_-$), and the normal and plasmino modes ($\nu_+ + \nu_-$) are separately shown, together with those of the Landau damping between quasi-particles ($\nu_+ - \nu_-$) and processes including the anomalous mode with the normal ($\nu_+ + V$) and the plasmino ($\nu_- - V$)

modes. From the figure, one finds that the two divergences at $\omega = \omega_1$ and ω_2 come from the Landau damping and the plasmino pair annihilation rates, respectively. As discussed in Section 4.3, these divergences come from the van Hove singularity. The dilepton production rate Eq. (206) is inversely proportional to derivatives of the dispersion relations, $d\nu_-(p)/dp$ and $d\{\nu_+(p) - \nu_-(p)\}/dp$. As shown in Figs. 20 and 32 each of $\nu_-(p)$ and $\nu_+(p) - \nu_-(p)$ has an extremum at nonzero p. Their values at the extrema are $\nu_+(p) - \nu_-(p) = \omega_1$ and $2\nu_-(p) = \omega_2$. At these points the derivatives vanish. This leads to the divergences in the photon self energy, and accordingly the dilepton production rate.

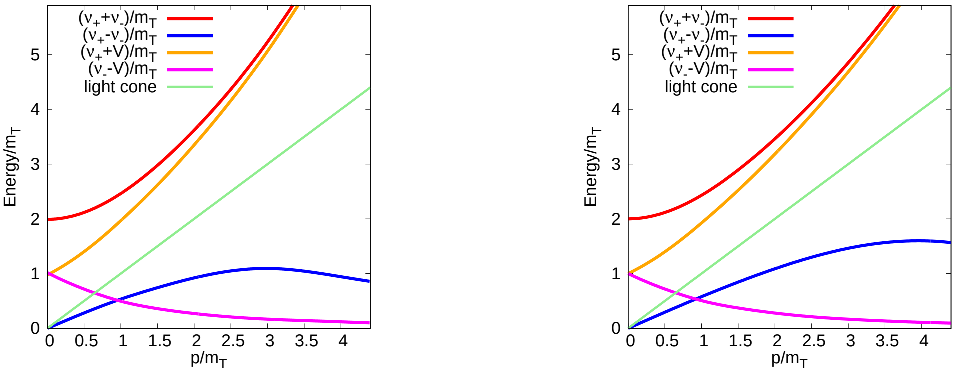

(a) $T = 1.5T_c$

(b) $T = 3T_c$

Figure 32: Momentum dependences of various functions composed of $\nu_\pm(p)$ and $V(p)$ for $T = 1.5T_c$ (left panel) and $3T_c$ (right panel).

The divergences due to the van Hove singularity are buried if the quark quasi-particles have a width. When the width is not large, however, the enhancement of the dilepton production rate would be observed as a remnant of the van Hove singularity, because the van Hove singularity takes place as a consequence of the concentration of the density of states. If the dispersion relation has the structure which causes such a concentration, the enhancement of the dilepton production rate is expected to occur although the singularity is blurred with the width of quasi-particles. It is also noteworthy that the analyses in Refs. [20, 21] suggest the small width of quark quasi-particles as discussed already in Section 4.1.1. The enhancement of the dilepton production near $\omega \simeq m_T$ found in this study, therefore, can be a robust phenomenon with the modified dispersion relations of quark quasi-particles.

Fig. 31 also shows that each individual process is non vanishing in a limited range of ω. The range can be read off from the corresponding functions plotted in Fig. 32. The $\nu_+ + \nu_+$ and $\nu_+ + \nu_-$ rates are non vanishing for $\omega > 2m_T$. On the other hand, the lower threshold of the $\nu_- + \nu_-$ rate, $\omega = \omega_2$, is slightly lower than $2m_T$, because $\nu_-(p)$ has a minimum smaller than m_T at nonzero momentum. The range of the Landau damping is also kinematically constrained to $\omega < \omega_1$. The $\nu_+ + V$ and $\nu_- - V$ rates are non vanishing for $\omega > m_T$ and $\omega < m_T$, respectively. The anomalous and normal mode rate gives rise to a nonzero value for $\omega_1 < \omega < \omega_2$. To the dilepton production rate without the vertex correction, only the $\nu_+ + \nu_+$, $\nu_- + \nu_-$, and $\nu_+ - \nu_-$ contribute and the rate vanishes for $\omega_1 < \omega < \omega_2$.

For large ω, the rate is dominated by the $\nu_+ + \nu_+$. This is a consequence of the fact that the quark propagator approaches the free quark one as p becomes larger. A glance at Fig. 31 might give an impression that the anomalous and normal mode rate also survives for large ω. Although not shown in Fig. 31, however, the $\nu_+ + \nu_-$ rate takes a negative value for $\omega \gtrsim 2.4 m_{\mathrm{T}}$, and this term almost cancels out with the $\nu_+ + V$ rate. We have checked that the sum of these terms is always positive. The total dilepton production rate for $\omega > 0$ therefore takes the positive value as it should be.

6 Discussion

Now, let us discuss phenomenological interpretations of the results in this study. We consider how obtained spectra are reflected on production yields and anisotropic flows which are observed in HIC in this section.

First, we focus on the discontinuities observed in photon and dilepton spectra. If the hot static QGP were stable and kept at a constant temperature, there is a possibility to observe these non-smooth structures in accumulated experimental data and positions of the non-smooth variations give the information of the temperature of the deconfined medium. However, the produced deconfined medium expands and cools down rapidly. As the hot matter cools down, positions of the non-smooth variation are changed. As a result, obtained spectra of yields, which are integration over production rates of various temperatures, do not have the non-smooth structure.

It seems not possible that the obtained non-smooth variations of the photon rate survives even in the photon yield. How about discontinuities of the dilepton production rate which arise via the van Hove singularity? Remember that the van Hove singularity also exists in HTL analysis though it is almost buried in the continuum contribution. Numerical results of the dilepton yield based on the HTL analysis do not show any discontinuity. It seems to mean that the dilepton production yield does not have the discontinuous structure even with our result.

6.1 Photons

Next, we consider each signal separately in more detail. First we discuss the photon production. According to numerical simulations of photon yield obtained by the flow based on a hydrodynamic model with the perturbative photon production rate, the production yield underestimates the experimental data about 0.5 [41]. Also this model does not reproduce the observed large photon v_2 and v_3 in RHIC [41, 42]. In Ref. [41], only the photon elliptic flow v_2 is evaluated with the hydrodynamics and the perturbative production rate but it reveals that prompt photons strongly suppresses the photon elliptic flow. This is the strange situation that photons produced by initial hard scatterings whose experimental yield is smaller by two order of magnitude suppress the v_2. Either way, however, the more photons should be emitted in the later stage since the hot QGP produced in order to reproduce the large elliptic flow.

The previous results of Refs. [41, 42] seem to imply that the more photons are produced from the hot media. We expected that the non-perturbative analysis varies the photon production from the deconfined medium and the variation led to improvements of phenomenological calculations. Surprisingly, however, the obtained result is almost comparable to perturbative results. This result itself is meaningful because it suggests that the perturbative analysis is accidentally coincident with the thermal photon radiation rate from the strong coupled QGP. It turns out that experimental data is larger than the present model calculation and our non-perturbative rate does not increase the yield from QGP. As to the case of the photon production yield, our non-perturbative analysis of the radiation rate does not change theoretical estimations of flows. It should be emphasized that the more photons emitted from the later stage of the time evolution of HIC, the flow grows up more larger because once photons are emitted they do not receive any more acceleration by the expansion.

These results imply a limitation of the present model whose photon sources are initial parton scatterings, photon productions from QGP and hadronic medium and final state decay photons. We guess a possible scenario to improve the model calculation. It is to introduce a new photon production mechanism such as a radiative recombination. When an additional photon production process exists at the later stage of the time evolution of HIC, it increases the total photon yield and generates the larger anisotropy. This scenario can solve the photon puzzle.

6.2 Dileptons

Next, we discuss the dilepton production. In HIC, only dilepton production yields are observed [9, 10]. The phenomenological calculation based on the vector dominance model well reproduces experimental data [49]. However, one should be careful that this analysis is based on a simple kinematics of the expanding medium [50,51]. In Refs. [50,51], the thermal fireball is approximated as an isotropic expanding cylinder. Such model is too simple to produce anisotropies, and thus a more realistic model as suggested in Ref. [52] is desirable.

In the present study, we evaluate thermal dilepton rates for $\boldsymbol{q} = \boldsymbol{0}$. They have enhancements owing to the van Hove singularity around 350MeV and 1GeV for $T = 1.5T_\mathrm{c},\ 3T_\mathrm{c}$, respectively. Because the enhancement of yields are observed in the low invariant mass region where $m_{l^+l^-} < 1$GeV, our results seem to be pleasing qualitatively. There is a possibility that enhancements arisen from the van Hove singularity reproduce the measured data. On the other hand, our results are smaller than the HTL by one order of magnitude on the whole. In addition, analyses of production yields depend on kinematics of media. Therefore, it is worth evaluating the production yield with our dilepton radiation and the realistic kinematic model. It is difficult to make a prediction on the total yield without the dynamical simulation but, at least, the more realistic kinematic model is desirable.

It should also be mentioned that the finite momentum dilepton production rate is needed to evaluate the yield per invariant mass and one can evaluate the finite momentum rate with the expansion of the numerical simulation.

7 Summary

We summarize the present study and make a short comment on the future work in this section in this study. In order to evaluate production rate of thermal photons and dileptons from the deconfined medium non-perturbatively, we evaluate the Schwinger-Dyson equation of the photon self energy with the quark propagator obtained on the lattice. The photon-quark vertex is constructed so as to satisfy the Ward-Takahashi identity. We evaluate the imaginary part of the full photon self energy gauge invariantly which is constructed with the lattice quark propagator and the vertex for two values of temperature $T = 1.5T_c$ and $3T_c$.

The lattice quark propagator is obtained with the two-pole approximation and does not have a continuum part. In addition, dispersions of quasi-particle calculated on the lattice QCD show peculiar structure. The dispersion of plasmino which has the minimum at finite momentum exists even in space-like region and is acausal in some region. We found that these peculiar features are reflected on real and virtual photon production processes.

There is the arbitrariness to determine the vertex and we use different vertices to analyze the photon spectrum and the dilepton spectrum. However, both vertices respect the gauge invariance and they have structures proportional to the inverse quark propagator. We substitute the lattice quark propagator, and thus vertices acquire anomalous poles. Radiations via anomalous poles cannot be interpreted as simple kinematics among quasi-particles and a photon. The anomalous pole affects the dilepton spectrum qualitatively but its contribution for the total production rate is relatively small.

We also perform numerical simulations of photon and dilepton radiations for zero momentum. Surprisingly, photon result shows the similar behavior the perturbative result. This coincidence is purely accidental and does not suggest a possibility that the produced QGP interacts weakly. If the coupling of produced deconfined medium is weak, it contradicts the fluid behavior of QGP. We first reveal that previous perturbative analyses are accidentally coincident with our non-perturbative result.

The dilepton production rate shows the smaller or comparable rate to the perturbative one. In contrast to the photon radiation, the obtained spectrum has qualitatively different structure from the perturbative one because the input quark propagator does not have the continuum part. The obtained rate shows divergences which arise from the van Hove singularity. The van Hove singularity also exists in the perturbative analysis but its positions differ from the previous ones owing to the difference of the dispersion.

Present analyses of photon production yield based on the fluid model and the perturbative calculation do not reproduce observed anisotropic flows of photons. In addition, the photon production yield evaluated with the same model shows the same order result as the experimental data but seems a little bit small. These facts imply the limitation of the previous model. It is possible that the extra photon production process exists in dynamics of ultra-relativistic heavy ion collisions.

For the dilepton production yield, the previous analysis based on the vector dominance model well reproduces experimental data. However, such a model uses the too simple model which cannot produce the anisotropy. In anticipation of the future measurement of dilepton flows, the production yield should be recalculated with the more realistic model.

As the future work, the numerical analysis of the production yields with the obtained production rates is an important task. For the photon production, the obtained yield is expected to be small against the experimental result, and thus the investigation of the new photon production mechanism is also important. To evaluate the dilepton production yield, we have to extend the formalism for the finite momentum virtual photon. This analysis can be carried out with the obtained photon self energy and the off-shell condition. In addition, the analysis on the vertex dependence is also an important future study.

Acknowledgements

I would like to express my appreciation to people who make constructive comments for me and support my research activities in doctoral course at Osaka University.

First, more than anyone else, I would like to express my sincere gratitude towards Prof. M. Asakawa who inspired me to engage in the curious research about thermal radiations of photons and dileptons from a quark-gluon plasma and give me essential advice on the present study. I received the great deal of inspiration for the interpretation of obtained results. I am also deeply grateful for the received support to engage in activities of Osaka University Cross-Boundary Innovation Program.

I deeply appreciate the support Assistant Prof. M. Kitazawa has all given me. Especially, I am grateful for the discussion on details, advice concerning to numerical analyses and delicate helps to carry out my study.

I would like to express my appreciation to Prof. M. Harada of Nagoya University for giving me the important comment on the phenomenological vertex function.

I would also like to thank to Osaka University Cross-Boundary Innovation Program. I could not be engaged in the doctoral research without various supports of CBI program. I am deeply grateful to Prof. K. Fujita and Prof. T. Shimoda who gave me a priceless opportunity to join CBI program.

Finally, I wish express the deepest appreciation to my family for support and encouragement throughout my academic life.

References

[1] G. Baym and C. Pethick, Ann. Rev. Astron. Astrophys. **17**, 415 (1979).

[2] T. Celik, F. Karsch and H. Satz, Phys. Lett. **97B** (1980) 128.

[3] I. Arsene *et al.* [BRAHMS Collaboration], Nucl. Phys. A **757**, 1 (2005); B. B. Back, *et al.* [PHOBOS Collaboration], ibid. **757**, 28 (2005); J. Adams *et al.* [STAR Collaboration], ibid. **757**, 102 (2005); K. Adcox *et al.* [PHENIX Collaboration], ibid. **757**, 184 (2005).

[4] B. Muller, J. Schukraft, and B. Wyslouch, Ann. Rev. Nucl. Part. Sci. **62**, 361 (2012).

[5] E. L. Feinberg, Nuovo Cim. A **34**, 391 (1976).

[6] E. V. Shuryak, Phys. Lett. **78B**, 150 (1978)

[7] A. Adare *et al.* [PHENIX Collaboration], Phys. Rev. C **91**, no. 6, 064904 (2015)

[8] J. Adam *et al.* [ALICE Collaboration], Phys. Lett. B **754**, 235 (2016)

[9] A. Adare *et al.* [PHENIX Collaboration], Phys. Rev. C **93**, no. 1, 014904 (2016)

[10] L. Adamczyk *et al.* [STAR Collaboration], Phys. Rev. C **92**, no. 2, 024912 (2015)

[11] A. Adare *et al.* [PHENIX Collaboration], Phys. Rev. C **94**, no. 6, 064901 (2016)

[12] T. Hirano and M. Gyulassy, Nucl. Phys. A **769**, 71 (2006)

[13] T. Hirano, U. W. Heinz, D. Kharzeev, R. Lacey and Y. Nara, Phys. Lett. B **636**, 299 (2006)

[14] F. Karsch, E. Laermann, P. Petreczky, S. Stickan and I. Wetzorke, Phys. Lett. B **530**, 147 (2002)

[15] H.-T. Ding, A. Francis, O. Kaczmarek, F. Karsch, E. Laermann and W. Soeldner, Phys. Rev. D **83**, 034504 (2011)

[16] L. D. McLerran and T. Toimela, Phys. Rev. D **31**, 545 (1985).

[17] H. A. Weldon, Phys. Rev. D **42**, 2384 (1990).

[18] C. Gale and J. I. Kapusta, Nucl. Phys. B **357**, 65 (1991).

[19] F. Karsch and M. Kitazawa, Phys. Rev. D **80**, 056001 (2009).

[20] M. Kitazawa and F. Karsch, Nucl. Phys. A **830**, 223C (2009).

[21] O. Kaczmarek, F. Karsch, M. Kitazawa and W. Soldner, Phys. Rev. D **86**, 036006 (2012).

[22] C. N. Yang and R. L. Mills, Phys. Rev. **96**, 191 (1954).

[23] M. Gell-Mann, Phys. Lett. **8**, 214 (1964).

[24] G. Zweig, CERN-TH-401.

[25] G. Miller *et al.*, Phys. Rev. D **5**, 528 (1972).

[26] M. Y. Han and Y. Nambu, Phys. Rev. **139**, B1006 (1965).

[27] R. Brandelik *et al.* [TASSO Collaboration], Phys. Lett. **86B**, 243 (1979); R. Brandelik *et al.* [TASSO Collaboration], Phys. Lett. **97B**, 453 (1980).

[28] J. J. Aubert *et al.* [E598 Collaboration], Phys. Rev. Lett. **33**, 1404 (1974).

[29] J. E. Augustin *et al.* [SLAC-SP-017 Collaboration], Phys. Rev. Lett. **33**, 1406 (1974) [Adv. Exp. Phys. **5**, 141 (1976)].

[30] D. J. Gross and F. Wilczek, Phys. Rev. D **8**, 3633 (1973).

[31] H. D. Politzer, Phys. Rept. **14**, 129 (1974).

[32] J. S. Poucher *et al.*, Phys. Rev. Lett. **32**, 118 (1974).

[33] C. G. Callan, Jr., Phys. Rev. D **2** (1970) 1541; K. Symanzik, Commun. Math. Phys. **18** (1970) 227; K. Symanzik, Commun. Math. Phys. **23** (1971) 49.

[34] G. 't Hooft, Nucl. Phys. B **33**, 173 (1971).

[35] J. C. Collins and M. J. Perry, Phys. Rev. Lett. **34**, 1353 (1975).

[36] M. Asakawa and K. Yazaki, Nucl. Phys. A **504**, 668 (1989).

[37] R. J. Fries, B. Muller, C. Nonaka and S. A. Bass, Phys. Rev. Lett. **90** (2003) 202303

[38] R. J. Fries, B. Muller, C. Nonaka and S. A. Bass, Phys. Rev. C **68**, 044902 (2003)

[39] T. Matsui and H. Satz, Phys. Lett. B **178**, 416 (1986).

[40] S. D. Drell and T. M. Yan, Phys. Rev. Lett. **25**, 316 (1970) Erratum: [Phys. Rev. Lett. **25**, 902 (1970)]; S. D. Drell and T. M. Yan, Annals Phys. **66**, 578 (1971)

[41] J. F. Paquet, C. Shen, G. S. Denicol, M. Luzum, B. Schenke, S. Jeon and C. Gale, Phys. Rev. C **93**, no. 4, 044906 (2016)

[42] C. Shen, U. W. Heinz, J. F. Paquet, I. Kozlov and C. Gale, Phys. Rev. C **91**, no. 2, 024908 (2015)

[43] K. Guettler *et al.* [British-Scandinavian-MIT Collaboration], Phys. Lett. **64B**, 111 (1976).

[44] J. Bartke *et al.* [Aachen-Berlin-Bonn-CERN-Cracow-Heidelberg-Warsaw Collaboration], Nucl. Phys. B **120**, 14 (1977).

[45] K. Fukushima, D. E. Kharzeev and H. J. Warringa, Phys. Rev. D **78**, 074033 (2008)

[46] K. Hattori and K. Itakura, Annals Phys. **330**, 23 (2013)

[47] K. Hattori and K. Itakura, Annals Phys. **334**, 58 (2013)

[48] K. I. Ishikawa, D. Kimura, K. Shigaki and A. Tsuji, Int. J. Mod. Phys. A **28**, 1350100 (2013)

[49] R. Rapp, J. Wambach and H. van Hees, Landolt-Bornstein **23**, 134 (2010)

[50] H. van Hees, M. He and R. Rapp, Nucl. Phys. A **933**, 256 (2015)

[51] R. Rapp and H. van Hees, Phys. Lett. B **753**, 586 (2016)

[52] C. Nonaka and M. Asakawa, PTEP **2012**, 01A208 (2012)

[53] K. Kajantie and H. I. Miettinen, Z. Phys. C **9**, 341 (1981).

[54] F. Halzen and H. C. Liu, Phys. Rev. D **25**, 1842 (1982).

[55] B. Sinha, Phys. Lett. **128B**, 91 (1983).

[56] R. C. Hwa and K. Kajantie, Phys. Rev. D **32**, 1109 (1985).

[57] G. Staadt, W. Greiner and J. Rafelski, Phys. Rev. D **33**, 66 (1986).

[58] R. D. Pisarski, Nucl. Phys. B **309**, 476 (1988).

[59] R. D. Pisarski, Phys. Rev. Lett. **63**, 1129 (1989).

[60] E. Braaten and R. D. Pisarski, Nucl. Phys. B **337**, 569 (1990).

[61] J. I. Kapusta, P. Lichard and D. Seibert, Phys. Rev. D **44**, 2774 (1991) Erratum: [Phys. Rev. D **47**, 4171 (1993)].

[62] R. Baier, H. Nakkagawa, A. Niegawa and K. Redlich, Z. Phys. C **53**, 433 (1992).

[63] P. B. Arnold, G. D. Moore and L. G. Yaffe, JHEP **0111**, 057 (2001)

[64] P. B. Arnold, G. D. Moore and L. G. Yaffe, JHEP **0112**, 009 (2001)

[65] J. Ghiglieri, J. Hong, A. Kurkela, E. Lu, G. D. Moore and D. Teaney, JHEP **1305**, 010 (2013)

[66] P. B. Arnold, G. D. Moore and L. G. Yaffe, JHEP **0206**, 030 (2002)

[67] E. Braaten, R. D. Pisarski and T. C. Yuan, Phys. Rev. Lett. **64**, 2242 (1990).

[68] S. M. H. Wong, Z. Phys. C **53**, 465 (1992).

[69] E. Braaten and R. D. Pisarski, Phys. Rev. D **42**, 2156 (1990).

[70] R. D. Pisarski, Nucl. Phys. A **525**, 175 (1991).

[71] R. Baier, G. Kunstatter and D. Schiff, Phys. Rev. D **45**, R4381 (1992).

[72] E. Braaten and R. D. Pisarski, Phys. Rev. D **46**, 1829 (1992).

[73] L. D. Landau, J. Phys. (USSR) **10**, 25 (1946)

[74] L. D. Landau and I. Pomeranchuk, Dokl. Akad. Nauk Ser. Fiz. **92**, 535 (1953).

[75] L. D. Landau and I. Pomeranchuk, Dokl. Akad. Nauk Ser. Fiz. **92**, 735 (1953).

[76] A. B. Migdal, Dokl. Akad. Nauk Ser. Fiz. **105**, 77 (1955).

[77] A. B. Migdal, Phys. Rev. **103**, 1811 (1956).

[78] J. S. Ball and T. W. Chiu, Phys. Rev. D **22**, 2542 (1980).

[79] T. Kim, M. Asakawa and M. Kitazawa, Phys. Rev. D **92**, no. 11, 114014 (2015)

[80] G. Baym, J. P. Blaizot and B. Svetitsky, Phys. Rev. D **46**, 4043 (1992).

[81] A. K. Rebhan, Phys. Rev. D **48**, R3967 (1993)

[82] M. Le Bellac, *Thermal Field Theory* (Cambridge University Press, Cambridge, 1996).

[83] J. A. Mueller, C. S. Fischer and D. Nickel, Eur. Phys. J. C **70**, 1037 (2010).

[84] M. E. Peskin and D. V. Schroeder *An Introduction to Quantum Field Theory*, (Westview Press, 1995).

[85] K. Yagi, T. Hatsuda and Y. Miake *Quark-Gluon Plasma*, (Cambridge University Press, Cambridge, 2005).

[86] J. I. Kapusta and C. Gale, *Finite-Temperature Field Theory Principles and Applications Scond Edition* (Cambridge Monographs on Mathematical Physics, 2006).

[87] M. Le Bellac, *Thermal Field Theory* (Cambridge University Press, Cambridge, 1996).